INFORMATION TO USERS

This reproduction was made from a copy of a document sent to us for microfilming. While the most advanced technology has been used to photograph and reproduce this document, the quality of the reproduction is heavily dependent upon the quality of the material submitted.

The following explanation of techniques is provided to help clarify markings or notations which may appear on this reproduction.

1. The sign or "target" for pages apparently lacking from the document photographed is "Missing Page(s)". If it was possible to obtain the missing page(s) or section, they are spliced into the film along with adjacent pages. This may have necessitated cutting through an image and duplicating adjacent pages to assure complete continuity.

2. When an image on the film is obliterated with a round black mark, it is an indication of either blurred copy because of movement during exposure, duplicate copy, or copyrighted materials that should not have been filmed. For blurred pages, a good image of the page can be found in the adjacent frame. If copyrighted materials were deleted, a target note will appear listing the pages in the adjacent frame.

3. When a map, drawing or chart, etc., is part of the material being photographed, a definite method of "sectioning" the material has been followed. It is customary to begin filming at the upper left hand corner of a large sheet and to continue from left to right in equal sections with small overlaps. If necessary, sectioning is continued again—beginning below the first row and continuing on until complete.

4. For illustrations that cannot be satisfactorily reproduced by xerographic means, photographic prints can be purchased at additional cost and inserted into your xerographic copy. These prints are available upon request from the Dissertations Customer Services Department.

5. Some pages in any document may have indistinct print. In all cases the best available copy has been filmed.

University Microfilms International
300 N. Zeeb Road
Ann Arbor, MI 48106

Siripala, Withana P.

STUDY OF SURFACE STATES AT THE SEMICONDUCTOR/ELECTROLYTE INTERFACE OF LIQUID-JUNCTION SOLAR CELLS

City University of New York PH.D. 1983

Study of Surface States at the Semiconductor/Electrolyte Interface of Liquid-Junction Solar Cells.

by

Withana P. Siripala

A dissertation submitted to the Graduate Faculty in Physics in partial fulfillment of the requirements for the degree of Doctor of Philosophy. The City University of New York.

1983

This manuscript has been read and accepted for the Graduate Faculty in Physics in satisfaction of the dissertation requirement for the degree of Doctor of Philosophy.

8/10/83
date

Prof. M. Tomkiewicz
Chairman of Examining Committee

8/23/83
date

Executive Officer

Prof. F.H. Pollak, Brooklyn

Prof. S. Aronson, Brooklyn

Prof. F. Smith, City College

Dr. R. H. Wilson, General El. Cor.
Supervisory Committee

The City University of New York

To my mother and family members

ABSTRACT

Study of Surface States at the Semiconductor/Electrolyte Interface of Liquid-Junction Solar Cells.

by

Withana P. Siripala

Advisor: Professor Micha Tomkiewicz

The existence of surface states at the semiconductor electrolyte interface of photoelectrochemical (PEC) cells plays a major role in determining the performance of the device in regard to the potential distribution and transport mechanisms of photogenerated carriers at the interface. We have investigated the n-TiO_2/electrolyte interface using three experimental techniques: relaxation spectrum analysis, photocurrent spectroscopy, and electrolyte electroreflectance (EER) spectroscopy. The effect of Fermi level pinning at the $CdIn_2Se_4$/aqueous-polysulfide interface was also studied using EER.

Three distinct surface states were observed at the n-TiO_2/aqueous-electrolyte interface. The dominant state, which tails from the conduction band edge, is primarily responsible for the surface recombination of photocarriers at the interface. The second surface state, observed at 0.8 eV

below the conduction band of TiO_2, originates in the dark charge transfer intermediates (TiO_2-H). It is proposed that the sub-bandgap (SBG) photocurrent-potential behavior is a result of the mechanism of dynamic formation and annihilation of these surface states. The third surface state was at 1.3 eV below the conduction band of TiO_2, and the SBG EER measurements show this state is "intrinsic" to the surface. These states were detected with SBG EER and impedance measurements in the presence of electrolytes that can adsorb on the surface of TiO_2. Surface concentration of these states was evaluated with impedance measurements.

EER measurements on a $CdIn_2Se_4$/polysulfide system have shown that the EER spectrum is sensitive to the surface preperation of the sample. The EER signal was quenched as the surface was driven to strong depletion, owing to Fermi level pinning at the interface in the presence of a high density of surface states. The full analysis of this effect enables us to measure the change in the flatband potential, as a function of the electrode potential, and also the energy distribution of these states.

ACKNOWLEDGEMENTS

I wish to express my deepest gratitude to my thesis advisor, Professor Micha Tomkiewicz, without whose valuable guidence, patience and understandings throughout my thesis work, this dissertation would not have been possible. I would also like to express my gratitude to Professor Fred H. Pollak for constant encouragement during this work.

I like to acknowledge with deep appreciation the careful reading of this manuscript and the advice given to me by the other committee members, Professors S. Aronson of Brooklyn College of CUNY and F.W. Smith of City College of CUNY and Dr. R.H. Wilson of General Electric Corporation.

There are many whom I would like to express my appreciations, Mr. Padmanabhan Paryanthal for the various helps given to me, Mr. Michael Kramer for helping me with typing, Mr. Dharmasena Peramunage for helping me with preparing slides,as well as Drs. Paul Amirtharaj and Ying-Sheng Huang.

I want to acknowledge with deep gratitude the department of Physics of Brooklyn College for providing me this opportunity. I gratefully acknowledge the Exxon Eduacation Foundation for the Exxon Eduacation Fellowship for new research initiatives and also NASA for partial support of this work.

CONTENTS

LIST OF FIGURES

Chapter 1

INTRODUCTION

1.1 SOLAR ENERGY CONVERSION AND PHOTOELECTROCHEMICAL SOLAR CELLS

In the last 25 years, serious consideration has been given to the task of converting the most abundant and reliable energy source, sunlight, into electricity. The photoelectric phenomena, which is basic to this process, was reported as early as 1839 by Becquerel [1] and by Adams and Day [2] in 1877. The fundamental process in photoelectricity is the interaction of light with the semiconducting material to produce electron-hole pairs that can then be separated by an internal electric field created by an inhomogeniety in the system. This inhomogeniety in the system can be caused by a metal-semiconductor contact (a Schottky junction), a junction between two regions of a semiconductor with different types of conductivity such as a p-n junction (a homojunction), a junction between two different semiconductors (a heterojunction), or a junction between a semiconductor and an electrolyte. Solar energy conversion devices require and exploit these above mentioned inhomogenities in the system. In the case of photoelectrochemical (PEC) solar cells, the semiconductor/electrolyte interface is involved in the pro-

cess of generation and transportation of charge carriers. The photogenerated carriers are thus participating directly in the chemical reaction at the surface of electrode, a process fundamental to the operation of the cell.

PEC cells are classified into two general categoreis: electrochemical photovoltaic cells and photoelectrosynthetic cells. In electrochemical photovoltaic cells, the photogenerated majority carriers are transported through the external circuit to deliver power at the load, while the net change in the electrolyte remains zero. The final result is then the conversion of light energy into electrical energy. In photoelectrosynthetic cells, however, there is a net change in chemical constituents in the electroltyte and the final result is the conversion of light energy into chemical enenrgy.

In recent years, interest has been growing in the use of PEC cells for low-cost solar energy conversion devices [3-12]. Field inhomogeniety which causes a potential barrier for the majority carriers at the junction, is one of the key factors deterimining the efficiency of the device. The establishment of this junction barrier is much easier in PEC cells, where the semiconductor is simply immersed in the electrolyte, than solid state solar cells, where contact is made between two solids. Since the contact between solid and liquid reaches better perfection than between the two solids, low-cost polycrystalline semiconductor films are po-

tentially more efficient in liquid junction solar cells than in solid state cells. However, in PEC cells, the stability of the semiconductor is often questionable, if the electrode decomposition reaction is more favorable than the desired chemical reactions in the electrolyte. This problem can be overcome by adding to the electrolyte a redox couple (see sec. 1.2.1B) whose reaction is much more favorable than the decomposition reaction.

Photoelectrolytic solar cells, i.e., photoelectrosynthetic cells that produce hydrogen and oxygen, are also being considered for solar energy conversion devices. Since Fujishima and Honda [13] first reported photoelectrolysis of water using TiO_2 electrodes, many researchers have extensively studied TiO_2 and other semiconductors for the purpose of photoelectrolysis [8,9]. Photoelectrolysis has attracted such attention because it converts solar energy into chemical energy in the form of hydrogen, which can be stored, transported, and used as a fuel. An efficient photoelectrolysis process would be an ideal source of hydrogen for the present energy requirement. Electrode stability, however, is still a major concern of this process, because while the chemical reactions are being decided, it is not possible to stabilize the electrode with other redox couples as in the electrolytic photovoltaic cells. Using a proper semiconductor would overcome this problem.

1.2 SEMICONDUCTOR/ELECTROLYTE INTERFACE

1.2.1 Space Charge Effect

As already mentioned in the previous section, the inhomogeniety in the system which produces the space charge layer at the semiconductor/electrolyte interface dominates the efficiency of the PEC devices.The mechanism that brings the system into a thermodynamic equilibrium and creates thereby a space charge layer at the interface can easily be understood by examining the motion of free carriers across the semiconductor/electrolyte interface.

As a specific example of space charge layer, we will examine an n-type semiconductor and an electrolyte with a reactive specie, A, which is in oxidized form, A^{++} and reduced form, A^{+}, in the solution. In other words, the redox couple in the electrolyte is A^{+}/A^{++}. When the system is brought in contact with the electrolyte, the following reaction can occur during the charge transfer process at the electrode:

$$A^{++} + e \rightleftharpoons A^{+} \qquad (1.1)$$

This charge transfer process continues until the electrochemical potential of the system becomes equal everywhere [14]. The transfer of electrons from the semiconductor to the electrolyte creates a space charge layer in the semiconductor, composed of the remaining positive charges (the ionized donors), and negative counter ions at the surface of

the semiconductor. This double layer creates an opposing electric field at the interface which prevents further charge transfer, and then the system attains thermodynamic equilibrium. The charge distribution and the electrostatic potential distribution at the interface after the charge transfer, are shown schematically in Fig.1(b) and (c), respectively. The initial difference in electrochemical potential between the semiconductor and the electrolyte, the parameter determining the driving force in the charge transfer process, can easily be understood by looking first at the individual electrochemical potentials of the electrolyte and the semiconductor.

(a) The Fermi Level in a Semiconductor:

Fig. 1(a) shows the density of state distribution in a semiconductor. The density of electron states in the conduction band can be approximated by [15];

$$D_e(E) = \frac{1}{2\pi^2} (2m_e/\hbar^2)^{3/2} (E-E_g)^{1/2} \qquad (1.2)$$

where m_e is the effective mass of an electron in the conduction band and E_g is the bandgap of the material. Here the energy (E) is measured from the top of the valence band. Similarly, the density of of states in the valence band is given by:

$$D_h(E) = \frac{1}{2\pi^2} (2m_h/\hbar^2)^{3/2} (-E)^{1/2} \qquad (1.3)$$

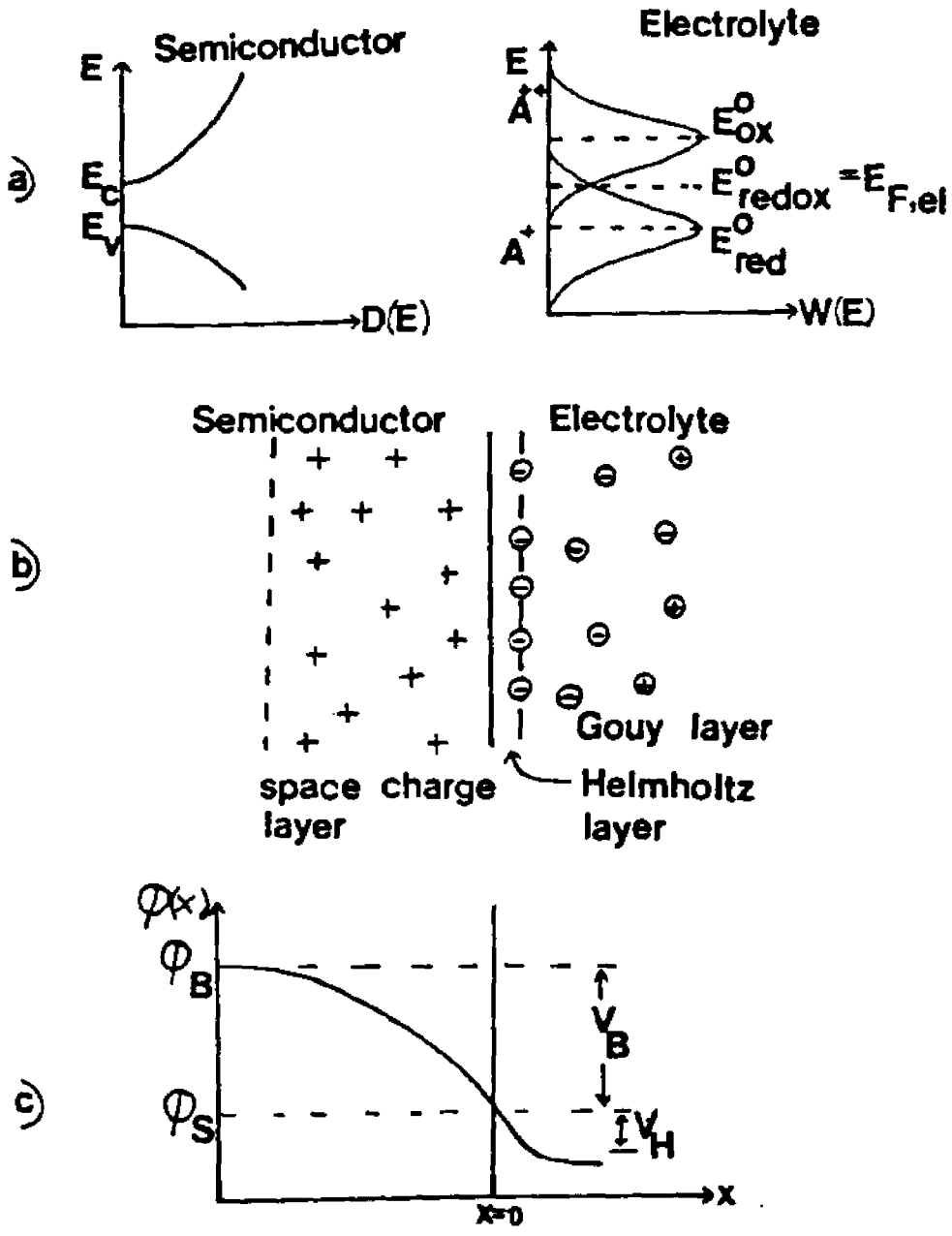

Fig. 1.1 Schematic representations of (a) energy levels in a semiconductor and an electrolyte, (b) charge distribution at the interface, and (c) electrostatic potential distribution at the interface.

where m_h is the effective mass of a hole in the valence band. By considering the condition for electroneutrality, it can be shown that for an n-type semiconductor the position of the Fermi level is given by [17,18]:

$$E_F = E_c - kT \ln(N_C/N_D) \qquad (1.4)$$

where N_D is the fully ionized donor concentration in the semiconductor and N_C is the effective density of states given by:

$$N_C = 2 (2\pi m_e kT/h^2)^{3/2} \qquad (1.5)$$

(b) The Electrochemical Potential in an Electrolyte:

In an electrolyte there are only a limited number of available electron states, and these are determined by the concentration of ions in the solution [14,16]. The energy distribution of these states is particularly important for the charge transfer process. The energy of an ion in solution fluctuates over a wide energy range because of the varying degrees of interaction with the surrounding dipoles in the electrolyte. As shown in Fig. 1(a), the fluctuation of the energy levels averages out in time to give a gaussian

distribution of energy levels around characteristic mean value for each component of the redox system. However, when the charge state of an ion is changed, the solvation shell is rearrenged to minimize the energy and hence the equilibrium energy of the filled or reduced state is separated from the empty or oxidized states (Franck-Condon splitting). According to Gerischer [19], the resulting normalized energy distribution functions are;

for occupied (reduced) states:

$$W_{red}(E) = (4\pi\lambda kT)^{-1/2} \exp\left[\frac{-(E-E^{o}_{red})^{2}}{4\lambda kT}\right] \qquad (1.6)$$

and for unoccupied (oxidized) states:

$$W_{ox}(E) = (4\pi\lambda kT)^{-1/2} \exp\left[\frac{-(E-E^{o}_{ox})^{2}}{4\lambda kT}\right] \qquad (1.7)$$

where E^{o}_{ox} and E^{o}_{red} are the most probable energies for the occupied and unoccupied states, respectively, in solution. The parameter λ represents the activation energy for the transformation of one species to the other. Also, E^{o}_{red}, E^{o}_{ox} and λ are related by:

$$E^{o}_{ox} - E^{o}_{red} = 2\lambda \qquad (1.8)$$

As shown in Fig.1(a), at the energy E^{o}_{redox}, the standard redox energy of the couple, it is equally likely that the state is either being occupied or emptied, i.e., the probability of occupation is 1/2 at the energy E^{o}_{redox}. This energy is referred to as the Fermi level in the electrolyte.

If the initial Fermi level in an n-type semiconductor is above the redox energy level in the electrolyte, then the equilibration of the two levels takes place by transfering electrons from the conduction band of the semiconductor to the electrolyte. The inverse situation occurs with a p-type semiconductor having an initial Fermi level below the redox energy of the electrolyte.

1.2.2 Solution to the Poisson's Equation

The mathematical description of the space charge layer at the semiconductor/electrolyte interface is substantially simplified because only one dimension has to be considered, the direction perpendicular to the surface. The electrostatic potential within the semiconductor at point x from the surface, Fig.1c , must satisfy the basic Poisson's equation:

$$\frac{d^2\varphi(x)}{dx^2} = \frac{\rho_{(x)}}{\epsilon\,\epsilon_o} \qquad (1.9)$$

where ϵ and ϵ_o are the dielectric constants of the semiconductor and the permitivity of the free space, respectively, and $\rho(x)$ is the charge density at the point x given by:

$$\rho_{(x)} = e\left[-n(x) + P(x) + N_D - N_A\right] \qquad (1.10)$$

where n(x), p(x), N_D and N_A are concentration of electrons, holes, donors, and acceptors, respectively (It is assumed here that all acceptors and donors are fully ionized).

For a fully depleted space charge layer, we can assume that the free carrier concentration appearing in the total charge density may be neglected. Also for an n-type semiconductor, acceptor concentration may be neglected. Thus the Equation 1.9 can be solved for an n-type semiconductor to obtain the thickness of the space charge layer [14], d:

$$d = (2\epsilon\epsilon_o/eN_D)^{1/2}\,(\varphi_B - \varphi_s - kT/e)^{1/2} \qquad (1.11)$$

where φ_B and φ_s are the electrostatic potentials in the neutral region and at the surface of the semiconductor, respectively (Fig. 1c). Since the electrostatic potential at the surface of the semiconductor is smaller than in the bulk, the electron energy at the surface is also higher there. Thus, as shown in Fig. 1.2, the bands are bent upward at the surface, creating a potential barrier for electrons. The band bending, V_b, is given by:

$$V_b = (\varphi_B - \varphi_s)$$

= potential drop across the space charge layer (1.12)

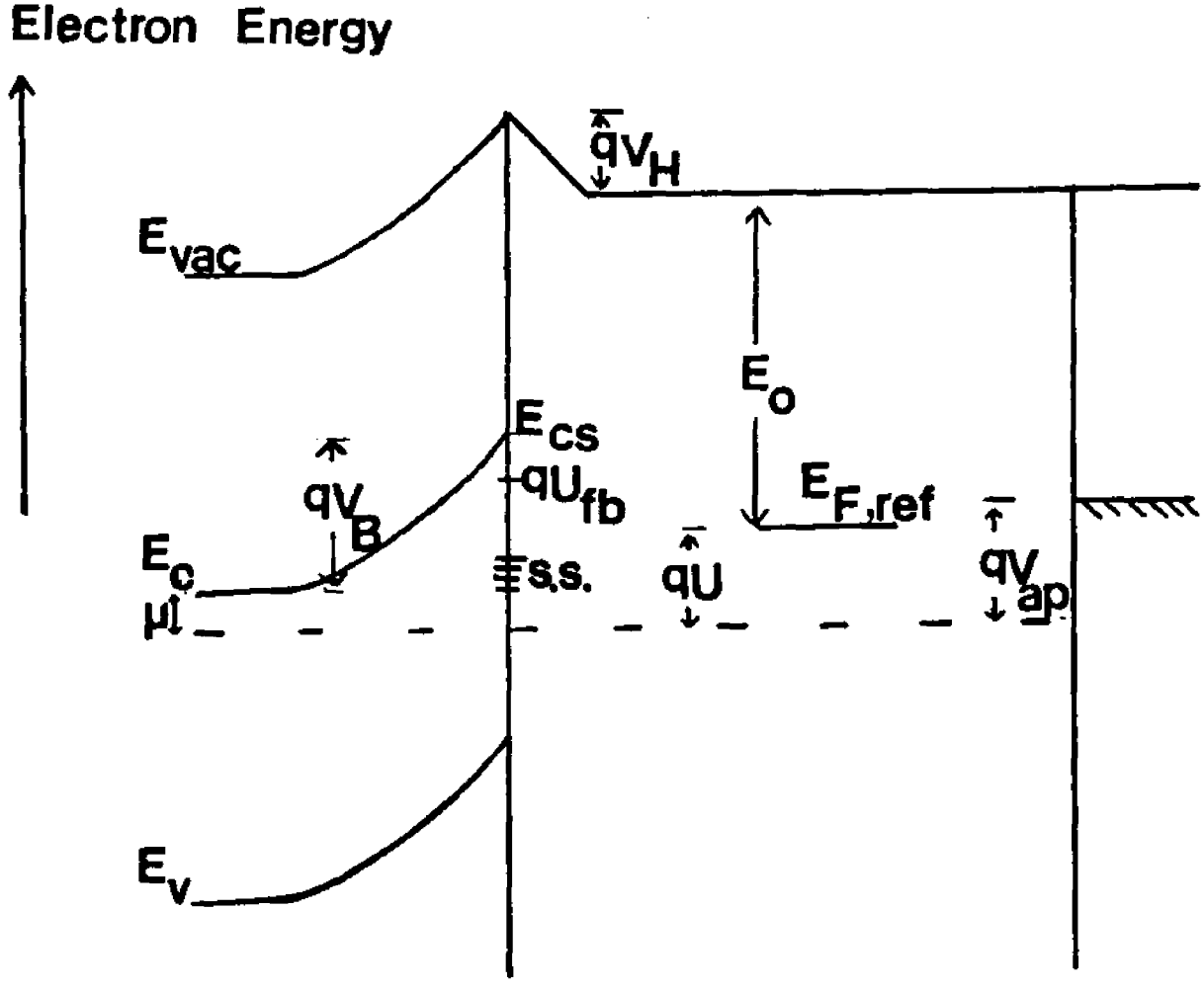

Fig. 1.2 Energy band diagram of the Semiconductor/Electrolyte interface.

1.2.3 Potential Distribution at the Semiconductor/Electrolyte Interface

As mentioned in the previous section, in addition to the space charge layer at the surface of the semiconductor, a layer of condense ionic countercharge, the Helmholtz layer, is present on the electrolyte side. The diffuse part of this layer is called the Gouy layer and it may extend into the electrolyte. The precise nature of the Helmholtz layer is not very well understood [20], because of the complicate interactions between the semiconductor surface and electrolyte species. In addition to the space charge layer, the potential distribution across the interface is shared by other double layers. In highly concentrated solutions, the diffuse double layer submerges into the Helmholtz layer [14]. The potential drop across the Helmholtz layer (Fig. 1(c) and Fig. 1.2) is determined by the adsorption/desorption processes [16,22], and also by charging and discharging of surface states [14].

The position of the Fermi level at the interface can be changed by applying an external voltage, V_{ap}, across the semiconductor and the counter electrode (Fig. 1.2). This potential drop will appear across the space charge layer, V_{sc}, and the Helmholtz layer, V_H, such that [14]:

$$V_{ap} = V_{sc} + V_H \tag{1.13}$$

In general, externally applied voltage can be considered to appear across the space charge layer. However, if high density of surface states is present at the interface, then it can not be assumed that the potential drop across the Helmholtz layer may be neglected, because the Fermi level at the surface can be pinned to the surface states [21,24]. In other words, only a fraction of the externally applied voltage will appear across the space charge layer. For now we will discuss the unpinned case only, and the details of pinning will be discussed in chapter 4. As the externally applied voltage varies, the band bending also varies accordingly, reaching zero at some particular voltage. This potential, as measured with respect to a standard electrode in the electrolyte, is called the flatband potential, U_{fb}, Fig. 1.2. Thus the band bending at the electrode potential U is given by:

$$V_b = U - U_{fb} \tag{1.14}$$

By examining the energy level diagram in Fig. 1.2, we can find an expression for the relationship between the position of the conduction band and the flatband potential[16], thus:

$$E_{cs} = -eU_{fb} + \mu \tag{1.15}$$

where μ is the energy difference between the Fermi level and the bottom of the conduction band in the bulk of the semiconductor. Thus the flatband potential is a measure of the position of the conduction band edge of the semiconductor with respect to a reference energy level in the electrolyte. Also, U_{fb} can be expressed in terms of the potential drop across the Helmholtz layer, such that [16]:

$$U_{fb} = A - V_H \qquad (1.16)$$

where A is an appropriate constant. Normally V_H is found experimentally to be a function of pH [22-24], 59 mV/pH, and hence the flatband potential also (Equation 1.16). The reason for this behavior can be understood by examining the possible adsorption processes which compete with each other in determining the total charge on the electrode surface. The pH dependance of the flatband potential could be explained by assuming that when the semiconductor is in contact with an aqueous electrolyte, the surface of the semiconductor is chemically bonded to OH groups [22-24]. The dissociation of this surface hydroxide is controlled by the pH of the solution according to the following process [24]:

$$\equiv Ti\text{-}OH + H_2O \rightleftharpoons \equiv Ti\text{-}O^- + H_3O^+ \qquad (1.17)$$

i.e., In alkaline or weakly acid solutions, the electrode is charge negatively as a result of the partial dissociation of surface hydroxide. Using thermodynamics considerations, it can be shown that [22]:

$$U_{fb} = \text{const.} - 2.3\ kT\ (pH)/e \qquad (1.18)$$

This gives a theoretical value of 59 mV/pH unit.

This important parameter, U_{fb}, can be found experimentally by measuring the space charge layer capacitance. From Equation 1.11, we can derive an expression for the differential capacitance of the space charge layer, C_{sc}, and also the Mott-Schottky relation [26]:

$$1/C_{sc}^2 = \frac{2}{\epsilon\,\epsilon_o\,eN_D}\ (\ U-U_{fb}-kT/e\ ) \qquad (1.19)$$

1.3 PHOTOEFFECT AT THE SEMICONDUCTOR/ELECTROLYTE INTERFACE

1.3.1 Absorption of Radiation

Optical absorption gives rise to the electronic transition across the bandgap of the semiconductor, which is caused by photons of energy equal to or greater than the bandgap energy. The absorption coefficient of the material as a function of photon energy is an intrinsic property of

the material, and it is determined by the electronic band structure of the material. It has been shown that near the band edge, the optical absorption coefficient, α , of a semiconductor can be expressed as [27,28]:

$$\alpha = A \frac{(h\nu - E_g)^{n/2}}{h\nu} \qquad (1.20)$$

where A is a constant and n depends on whether the transition is direct (n=1) or indirect (n=4). The generation rate of the electron-hole pairs,G, at a distance x inward from the surface of the semiconductor is given by [17]:

$$G = I_a (1-R) e^{-\alpha x} \qquad (1.21)$$

where R is the reflectivity and I_a is the incident photon flux of monochromatic illumination.

1.3.2 Transport of Photocarriers

The electron-hole pairs generated within the semiconductor are separated by the existing electric field in the space charge layer. The minority carriers are thus driven to the semiconductor/ electrolyte interface.The hole flux coming towards the interface, which is generated within the space charge layer, F_f, is given by:

$$F_f = \int_0^d G\,dx = I_a (1-R)(1-e^{-\alpha d}) \qquad (1.22)$$

The light that is not absorbed in the space charge layer is absorbed in the field-free region of the semiconductor. In this region, hole density is determined by the recombination and diffusion processes. The excess concentration of hole density, P , is determined by the following one dimensional transport equation [9]:

$$\frac{dP}{dt} = G + D_p \frac{d^2P}{dx^2} - (P-P_o)/\tau \qquad (1.23)$$

where D_p is the diffusion coefficient for the holes, P_o is the equilibrium hole concentration, and τ is the lifetime of holes. At the steady state, i.e. $\frac{dP}{dt}$ =0, the hole flux diffuses into the space charge layer, F_{diff}, can be evaluated with Equation 1.21, which can be easily solved with the following boundary conditions (Gartner model [29] as applied by Butler [30]).

$$P = P_o \quad \text{for} \quad x = \infty \qquad (1.24)$$

and

$$P = 0 \quad \text{for} \quad x = d \qquad (1.25)$$

Hence, Equation 1.21 leads to [9,14]:

$$F_{diff} = \frac{I_a (1-R)\alpha L_p}{1+\alpha L_p} e^{-\alpha d} + P_o D_p / L_p \qquad (1.26)$$

where $L_p = (D_p \tau)^{1/2}$ is the diffusion length. The last term can be neglected for wide bandgap semiconductors [14]. The simple boundary condition used here is valid only for large d [29]. A more general treatment to the solution of the transport equation was reported by Wilson [31], where a boundary condition parameter that directly related to the total charge transfer rate at the surface was introduced.

From Equations 1.22 and 1.26 we can write the total hole flux coming to the surface ,F , as:

$$F = I_a (1-R) \left[1 - \frac{e^{-\alpha d}}{1+\alpha L_p} \right] \qquad (1.27)$$

The hole flux at the surface is divided into two parts [9,31]. One is the recombination flux, F_r , in which holes are recombined via surface states, given by [9,31]:

$$F_r = S_r P_s \qquad (1.28)$$

where P_s is the surface density of holes, and S_r is the appropriate rate constant parameter, determined by the surface state density distribution. The specific nature of S_r can be understood by applying the Hall-Schockley-Read statictics

[32,33] for the surface recombination. The surface recombination rate resulting from a discrete surface state at the energy E_t with density $N(E_t)$,can be written as [17]:

$$F_r(E_t) = \frac{\sigma_\tau v_{th} N_t(E_t) P_s}{1 + e^{(E_t - E^s_{Fn})/kT}} \tag{1.29}$$

where σ_τ is the capture cross section of the holes, v_{th} is the thermal velocity, and E^s_{Fn} is the quasi-Fermi level at the surface. For a continuum of surface states in the gap, the surface recombination rate can be written as:

$$F_r = \int_{E_V}^{E_C} F_r(E_t)\, dE_t \tag{1.30}$$

Thus from Equations 1.28 ,1.29 , and 1.30 we can write S_r as [31]:

$$S_r = \sigma_\tau v_{th} \int_{E_V}^{E_C} \frac{N_t(E)\, dE}{1 + e^{(E - E^s_{Fn})/kT}} \tag{1.31}$$

$$= \sigma_r v_{th} n_t \tag{1.32}$$

where n_t is the total number of occupied states.

The other part of the total hole flux at the surface is transferred to the electrolyte species in the solution. This

chrage transfer flux, F_t , determines the total photocurrent and can be written as [34]:

$$F_t = S_t P_s \tag{1.33}$$

where S_t is the charge transfer parameter. S_t can be written as [31]:

$$S_t = \int_{E_v}^{E_c} v_{th} \sigma_t N_t(E) \, dE \tag{1.34}$$

where $N_t(E)$ is the area density of reaction centers in the electrolyte, and σ_t is the interaction cross section of the holes. At equilibrium:

$$F = F_r + F_t = I_a (1-R) \left[1 - \frac{e^{-\alpha d}}{1 + \alpha L_p} \right] \tag{1.35}$$

Therefore the photocurrent, J_a , will be:

$$J_a = e I_a (1-R) S_t/(S_t+S_r) \left[1 - \frac{e^{-\alpha d}}{1+\alpha L_p} \right] \tag{1.36}$$

Hence, the quantum efficiency, φ , can be written as [9]:

$$\varphi = \frac{J_a}{eI_a} = \frac{(1-R)\ S_t}{S_t + S_r} \left[1 - \frac{e^{-\alpha d}}{1 + \alpha L_p} \right] \qquad (1.37)$$

Equation (1.37) gives the dependence of the quantum efficiency on the system parameters. The photocurrent-potential behavior is implicit through the potential dependent parameters: space charge layer thickness, d, and surface recombination rate, S_r. In this simple model, the major recombination mechanisms are the bulk recombination in the field-free region and the surface recombination at the interface. Models that deal with recombination at the space charge layer [34,35] as well as those at the space charge layer and the surface [37] have also been reported.

It is evident from equation (1.37) that the surface recombination causes the decrease in quantum efficiency of the photoelectrolysis process. To date, the mechanism by which electrons are exchanged between the semiconductor and the electrolyte species is not very well understood.The equilibrium redox level of the O_2/H_2O couple lies at the middle of the bandgap of TiO_2 [9,39].In this case, only a very low photocurrent for oxygen evolution reaction can be expected since the overlap of the valance band and the reduced states in the electrolyte is very small.Nevertheless, quantum efficiency near 100% has been reported [39-41], which suggests that an alternative process must dominate the charge transfer process across the interface. The most commonly accepted

idea is that the charge is transferred across the interface via surface states [42-45], which are present in the bandgap of the semiconductors.

1.4 SURFACE STATES

Surface states are defined as the localized electronic energy levels present at the surface of the material. The existance of surface states was first discovered by Shockley and Pearson [46] during their surface conductance experiments, and theoretical studies about these states were reported in the literature by Tamm in 1933 [47] and Shockley in 1939 [48]. Because these localized energy levels are active in exchanging or sharing electrons with the bulk of the material and thus actively participate in the electronic and other related properties of the interface, the understanding of the origin and the characteristics of these surface states would be of great importance from the fundamental and applied points of view.

1.4.1 Origin of Surface States

Surface states can originate from many causes, for example, from the termination of the crystal at the surface, which results in a perturbation to the periodic potential (intrinsic surface states), from impurity atoms at the surface, or from adsorbates and ions in the solution at the solid/electrolyte interface, when the ions are close enough

to exchange electrons efficiently with the bands of the solid.

In the case of a clean surface (i.e., where no foreign atoms are being adsorbed), the origin of surface states can easily be understood by examining the atoms on the surface and in the bulk of the material. Bulk atoms of the crystal have a complete set of nearest neighbors, while the surface atoms have at least one neighbour missing. Thus, in the case of a covalent crystal, the surface atom of the lattice has an incomplete bond (or dangling bond);their orbitals occupy different levels than those in the bulk, and hence the so-called Shockley surface states [48] are formed. In these surface states electrons are exchanged with the bands or with the adsorbates with strong covalent bonding.

When the crystal is ionic, on the other hand, the surface atoms are not only incomplete from a co-ordinate point of view but from an electrostaic one as well. This additional electrostatic effect may result in energy levels at the surface. These so-called Tamm surface states [47] can accept or donate the unpaired electrons to the band or to the adsorbates.

The third kind of surface state is associated with the acid (or base) sites [16], where electron pairs are accepted or donated for sharing with adsorbing species.

1.4.2 Theoretical Models of Surface States

In this section we will examine briefly theoretical models for the calculation of surface states, first in the case of adsorbate-free "clean" surface and then for surfaces containing foreign adsorbates.

(a) Adsorbate-free Surface:

In order to demonstrate the origin of states at the semiconductor surface, a simple model has been selected that involves a simple one- dimensional, semi-infinite crystal [16,49].

The wave function of the electronic state in the crystal can be represented as a linear combination of atomic orbitals (LCAO):

$$|\psi\rangle = \sum_i c_i |\varphi_i\rangle \qquad (1.38)$$

where $|\varphi_i\rangle$ is the atomic wave function of the i^{th} atom in the chain and c_i is the corresponding expansion coefficient. This wave function must obey the Schrodinger equation:

$$H|\psi\rangle = E|\psi\rangle \qquad (1.39)$$

From Equations 1.38 and 1.39:

$$\sum_i c_i (H_{ji} - E S_{ji}) = 0 \qquad (1.40)$$

where

$$H_{ji} = \langle \varphi_j | H | \varphi_i \rangle \tag{1.41}$$

and

$$S_{ji} = \langle \varphi_j | \varphi_i \rangle \tag{1.42}$$

The coulomb integral of the i^{th} atom, H_{ii}, is denoted by:

$$H_{ii} = \alpha \tag{1.43}$$

For simplicity, only the nearest neighbor interaction is assumed, i.e., $H_{ij}=0$ unless $i=j\pm1$.

$$H_{ij} = \beta \quad (i = j \pm 1) \tag{1.44}$$

Also, from orthoganality:

$$S_{ij} = \delta_{ij} \tag{1.45}$$

These set of assumptions comprises the Huckel approximation to LCAO. Now, suppose the one-dimensional crystal to be AB

with alteranting A and B atoms,and suppose also that the corresponding α's are given by α_A and α_B respectively.Then from Equation 1.40:

$$(X-Z_1)\, C_i = C_{i-1} - C_{i+1} \qquad (i \text{ odd}) \qquad (1.46)$$

$$(X+Z_1)\, C_i = C_{i+1} - C_{i-1} \qquad (i \text{ odd}) \qquad (1.47)$$

where

$$X = 1/\beta \left[E - (\alpha_A + \alpha_B)/2 \right] \qquad (1.48)$$

and

$$Z_1 = 2\beta (\alpha_A - \alpha_B) \qquad (1.49)$$

Thus, the above set of Equations,1.46 and 1.47, can be solved to give the two bands of allowed energies [49] - conduction band and valence band - with a forbidden gap, E_g:

$$E_g = \alpha_A - \alpha_B \qquad (1.50)$$

But if the crystal is terminated on an A or B atom at the surface, then the boundary condition has to be imposed. Since there is no neighbor on one side of the surface atom, the coulomb integral for this surface atom would be different from the one for bulk atom. In the case that the surface atom (i=1) is A, suppose α_A changes to α_A', then from Equation 1.44:

$$(X-Z_A)\ C_1 = C_2 \qquad (1.51)$$

where

$$Z_A = 1/\beta \left[\alpha_A' - (\alpha_A + \alpha_B)/2 \right] \qquad (1.52)$$

It can easily be shown [49] that this surface energy is different from the bulk energy level; also, the wave function corresponding to this energy state decays exponentially into the crystal, which results in localized states at the surface.

(b) Adsorption of Foreign Species on the Surface:

Since the electronic structure of the surface is perturbed by the adsorption of foreign species on the surface of the solid, a modification in the distribution of surface state energy can be expected. Many theoretical approaches have been used to [16] explain the adsorption of foreign at-

oms on a solid surface. Here we will discuss the results obtianed by Kowalski et al. [50] on adsorption of water on a TiO_2 surface, in which the technique called "self-consistant field X-alpha scattered wave (SCF-X-SW) method" was used. Their calculations are based on a "cluster" of atoms formed from a few substrate atoms and the adsorbed atoms.

Figures 3(a) and 3(b) show the Ti3d and O2p atomic levels and the calculated TiO_2 bulk energy levels. The (110) surface of TiO_2 has been treated as a $(TiO_2)^{6-}$ cluster, and Kowalsky et al. have shown that a surface state is present within the bandgap of TiO_2 , Fig. 3(c). They have also shown that the adsorption of water molecules will shift the surface state away from the bandgap, Fig. 3(d). Fig. 3(e) shows that the adsorption of OH^- also leads to the surface states within the bandgap of TiO_2. This semi-quantitative calculation demonstrate the influnce of foreign molecules adsorption on the surface state energy distribution.

1.4.3 The Formation of Surface State Bands

In this section we will describe briefly the reason for the formation of surface state bands rather than the single-value orbitals. One common reason for the broadening of the experimentally observed surface state density distribution is the heterogeniety of the surface, for which there are number of possible causes [16]: (a) The dislocation of the atoms at the surface where the crystal structure is badly

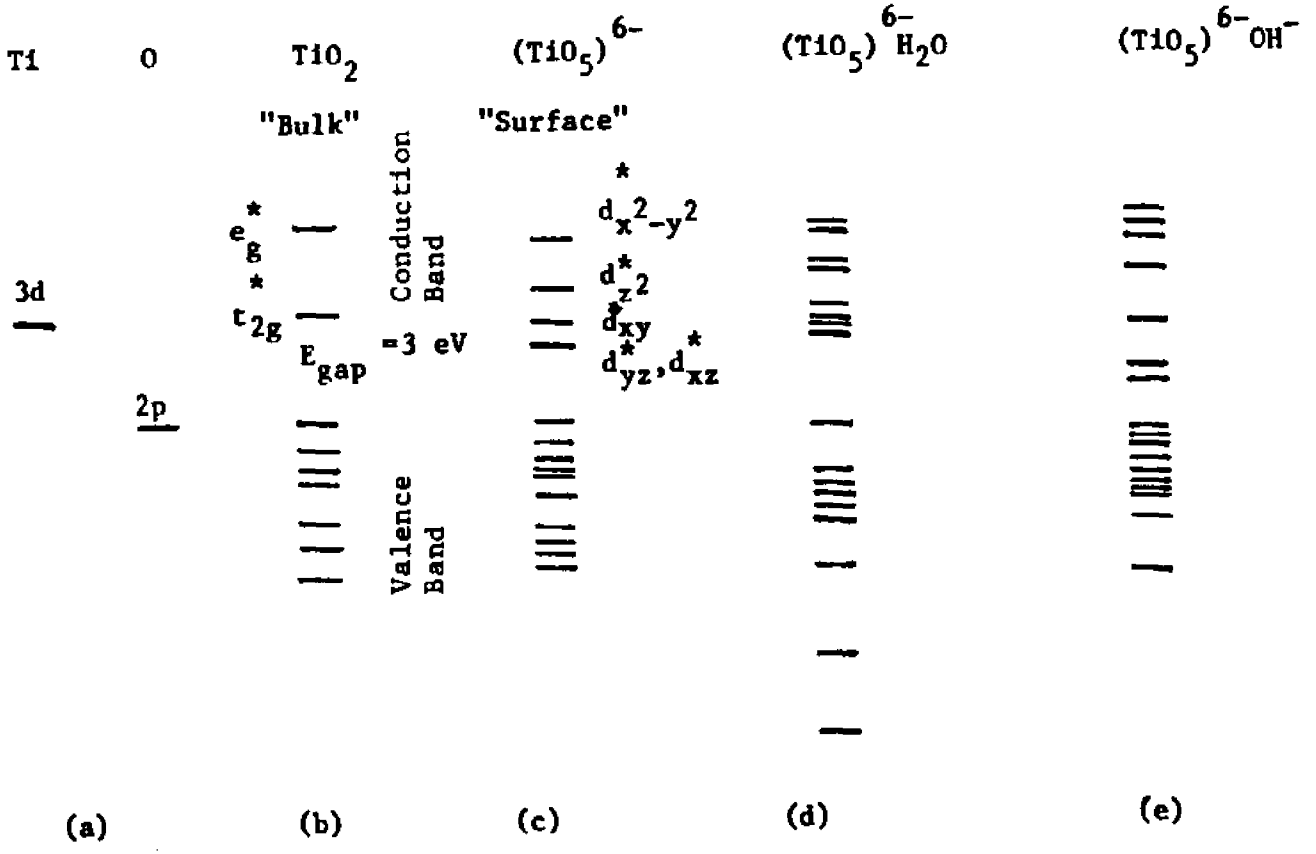

Fig. 1.3 Energy level diagrams of (a) free Titanium and Oxygen, (b) bulk TiO_2, (c) (110) of TiO_2, (d) water chemisorbed (110) surface of TiO_2, and (e) OH^- chemisorbed (110) surface of TiO_2. (Ref. 50)

perturbed and may result in a very active surface atoms. (b)The crystallographic steps may be created [51] where one or more crystal half planes having different characteristics than the main surface plane are exposed. (c) Unidentified foreign adosrbates may be present at some sites of the surface. Experimentally, measurements will average out over a large area, while the true surface state distribution varies from site to site, and hence results in a broad surface state band.

Surface state band formation may also be caused by a polar electrolyte in contact with the surface. According to Morrison [16], the temporal fluctuations of the polarizable solvent cause a gaussian distribution of surface states. If σ is the standard deviation of this gaussian distribution, then it can be shown that [16]:

$$e\sigma = (2\lambda kT)^{1/2} \qquad (1.53)$$

where λ is the activation energy for solvent reorganization. On the other hand, Tomkiewicz [52] has shown that surface states at the interface of a surface modified TiO_2 electrode and an aqueous electrolyte do not favor this model. He has shown that [52] the value of λ obtained for surface states (according to Equation 1.53) is larger than any reorganization energy recorded for free ions in aqueous solutions. Also, a linear relation between σ and the concentra-

tion of the surface state , in contrast with Equation 1.53, has been observed by Tomkiewicz [52].

Still another possible origin of the surface state band formation is the overlap of the adsorbate orbitals,which is based on the same quantum mechanical arguments that cause bands in the bulk of the material. Indeed, in the same study, Tomkiewicz showed that [52], considering the two-dimensional overlap of impurity states, the linear behavior between σ and the concentration of the surface state can be explained.A simple mathematical relation can be expressed for a two-dimensional square lattice, representing the surface atoms, in the first order tight binding approximation, in regarding to the surface state band broadening.Hence obtained first order tight binding energy is given by [15,52]:

$$E_k = -\alpha - 2\gamma\left[\cos(k_x a) + \cos(k_y a)\right] \qquad (1.54)$$

where k is the wave vector, a is the lattice constant,α is the coulomb integral, and γ is the overlap integral. The width of the band is 8γ .It has been shown that for oxygen on $SrTiO_2$, the broadening is 3 eV [52].

1.5 SURFACE SATES AT THE SEMICONDUCTOR/ELECTROLYTE INTERFACE

We are primarily concerned in this study with surface states at the semiconductor/electrolyte interface of liquid junction solar cells. In the literature, different experimental techniques have been used to investigate surface states at various kind of semiconductor/electrolyte interfaces.

Early evidence of the presence of surface states at the semiconductor/electrolyte interface was reported by a number of researchers who measured capacitance on germanium electrodes.Bohnenkamp and Engel (1957) [53] and Hoffman-Perez and Gerischer (1961) [54] reported that the capacitance of the germanium electrodes were not behaving as they had expected. Later, Brattain and Boddy [55] explored reason for this behavior by measuring the effect of cupric ions added to the solution.They found that the existing surface states at the interface contributed to the total capacitance and hence caused the unexpected deviation. They also found that these states were caused by the copper crystallites on the surface.Similar results were also observed when Au and Ag ions were added to the solution [56]. Memming [57,58], on the other hand, found that the mere addition of cupric ions to the solution did not produce surface states on either an n-or a p-type germanium. On the n-type (but not the p-type) germanium, surface states were obtained by illuminating the sample. It has been reported elsewhere [59] that surface

states can be created even when electrodes are treated in the standard way. Geramanium electrodes in strongly acidic and basic solutions also produce surface states and, therefore, addtional capacitance [59].

Many [60] has carried out pulsed experiments to measure transient current through the CdS/electrolyte interface. He found that currents of longer duration were responsible for emptying some surface states, located at 0.8 eV below the conduction band, through tunneling.

Frank and Bard [42] compared the oxidation-reduction peak potentials of a large number of redox couples on both a Pt and a TiO_2 electrode . They found that some couples with more positive redox potentials than the flatband potential of TiO_2 can be reduced irreversibly. They suggested that there is a surface state about 1.2 eV below the conduction band of TiO_2 that can communicate efficiently with conduction band. Morisaki et al. [61] have given evidences for the existance of surface states about 1.3 eV below the conduction band of TiO_2 . They observed in their spectral response measurements a peak at 800 nm corresponding to an electronic transition from the valence band to a surface state at 1.7 eV above the valence band.

Tomkiewicz [24] has shown the existance of a surface state at 1.3 eV below the conduction band of TiO_2 using impedance measurements on an n-TiO_2 /aqueous-electrolyte interface.He has also shown that the high density of surface

states at the interface could lead to a non-linear Mott-Schottky relation. Linear Mott-Schottky behavior could be regained by cleaning the sample surface. Tomkiewicz reported [54,62] another important result on TiO_2 electrodes, namely, that when the surface of such an electrode is chemically modified, surface states are created. He used impedance and photocurrent measurements to identify and characterize these states. These measurements also revealed that the surface state density distribution was gaussian, and the position of the distribution was determined by the derivertized material. These observations led him to the conclusion that band formation was caused by the overlap of the impurity states, and the gaussian distribution was a result of the random distribution of surface states on the crystal surface.

Current-voltage characteristics of TiO_2 electrodes have been used by Wilson [62] to identify and characterize surface states . He observed a reduction peak during a voltage sweep in the dark after a short period of illumination to the bandgap radiation,and attributed this peak to a reduction of surface states oxidized by photogenerated holes. Also it has been suggested by Wilson that these states may be reaction intermediates leading to the oxygen evolution reaction.

Heller et al. [63] have shown the existance of surface states at n-CdS and n-CdSe photoanodes in liquid-junction solar cells. They identified these states by studing the

effect of background illumination on the photoresponse using two beams experiments. They also found that ,as expected,once these surface states were removed by brief surface etching, the efficiency of the solar cells could be improved.

Laser and Gottesfeld [65] identified the existance of surface states at the thermally grown Ti-oxide films using the sub-bandgap induced photocurrent measuremetns. They found that the sub-bandgap photocurrent is enhanced by the continuous illumination from bandgap radiation. The sub-bandgap photocurrent, they suggested, resulted from the excitation of electrons from the valence band to the empty surface states, and the enhancement was caused by the emptying of surface states by bandgap radiation. They proposed a surface state band extending from the top of the valence band to the middle of the bandgap.

In a recent study by Dare-Edwards et al. [65], the photogeneration of hydrogen on a p-type semiconductor was investigated. A surface state created at the p-GaP/electrolyte interface from the charge transfer intermediate produced by the hydrogen evolution reaction was identified, and capacitance and a.c. photocurrent measurements were used to characterize it. They concluded that the surface states were generated by surface bonded hydrogen atoms, which are created and annihilated simultaneously as the hydrogen evolution reaction proceeds.

Recently, Silberstein et al. [67,68] showed the applicability of the electrolyte electroreflectance (EER) technique in determining the status of Fermi level in situ, in semiconductor/electrolyte interface. Their measurements of polycrstalline CdSe in polysulfide solution revealed a strong dependence of the EER signal on the applied bias voltage. They interpreted their results as the Fermi level pinning at the interface caused by the charging of high density of surface states.

Gutierrez and Salvador [69] reported that two types of surface states are present at the TiO_2 /aqueous electrolyte interface and claimed that these states are associated with surface OH groups. From their cyclic-voltammetry measurements they concluded that some surface states are localized near the conduction band and they overlap with the empty levels of the electrolyte species, while others are near to the valance band. The states near to the valance band, they suggested, are directly involved in the photo-oxidation of water.

1.6 LAYOUT

The main objectives of this study are: (a) to explore three experimental techniques for the identification and characterization of surface states at the semiconductor/electrolyte interface and (b) to study the effect of these states on the potential distribution and the photoinduced

charge transfer at the interface of liquid-junction solar cells. Though we are primarily concerned with the n-TiO_2 /aqueous electrolyte interface of photoelectrolytic solar cells, the study also includes an investigation of the $CdIn_2Se_4$/polysulfide interface in order to study a specefic aspect - Fermi level pinning - of the semiconductor/electrolyte interface which is not found in the n-TiO_2 /aqueous electrolyte system.

In chapter 2, we will discuss the experimental details of the three techniques employed in this work: relaxation spectrum analysis , photocurrent spectroscopy, and Electrolyte Electroreflectance Spectroscopy. Sample preperation and the PEC cell employed will be discussed.

Chapter 3 contains the experimental results obtained using the above mentioned techniques.The results on the impedance measurements, EER measurements, and photoresponse measurements will be presented for the n-TiO_2 /aqueous electrolyte system. Also, results will be given for the $CdIn_2Se_4$/polysulfide system where the EER spectra show dramatic changes under various conditions of the electrodes.In the study of Fermi level pinning at the semiconductor/electrolyte interface, the potential behavior of the EER signal in this system will be presented.

Chapter 4 contains a discussion of experimental results. The surface state capacitance variations (i.e.,the structures apearing at 0.8 eV and 1.3 eV below the conduction

band) are correlated with the sub-bandgap photocurrent measurements and the EER measurements. The surface state appearing at 0.8 eV below the conduction band is referred to as the charge transfer intermediate at the TiO_2 /electrolyte interface. The other structure at 1.3 eV below the conduction band is referred to as the "intrinsic" surface state at the TiO_2 surface. The shift in the flatband potential, as measured by both impedance and EER measurements, seems to result from the adsorption of foreign ions on the surface of TiO_2 . The sub-bandgap induced photocurrent-potential behavior is caused by the interaction between the dark charge transfer intermediates and the photoexcited carriers. The bandgap induced photocurrent -potential behavior is explained by accounting the surface recombination of photocarries via the tailing surface state band. The observed decline of phtoresponse due to background illumination is explained as resulting from the transference of photoinduced electrons from the conduction band to the surface states. Finally, the strong potential dependance of the EER signal for $CdIn_2Se_4$ is interpreted as an occurence of Fermi level pinning at the interface (a detail analysis of this effect will be given.). Chapter 4 will conclude with a summary and some proposals for future work.

Chapter II

EXPERIMENTAL TECHNIQUES

Three major experimental techniques have been employed in this work for the study of surface states at the semiconductor/electrolyte interfaces. These three techniques are independent of each other with regard to the basic principles involved in the processes that determine the system responses. Thus, in the relaxation spectrum analysis technique, the electrical response of a PEC cell to an applied a.c. signal is measured; in the other technique, photocurrent spectroscopy, only the optical response of the system is involved; and in EER spectroscopy , the electro-optic effect is employed to determine system response.

2.1 RELAXATION SPECTRUM ANALYSIS TECHNIQUE

Relaxation spectrum analysis technique [70,71] has been widely used to investigate the electrical properties of semiconductor/electrolyte interfaces [24,52,65,70-73]. This technique is based on impedance measurements over a wide range of frequencies to evaluate the passive elements in an equivalent circuit representing the interface. This equivalent circuit is modeled according to the different charge accumulation modes at the interface. Fig. 2.1(a) shows a

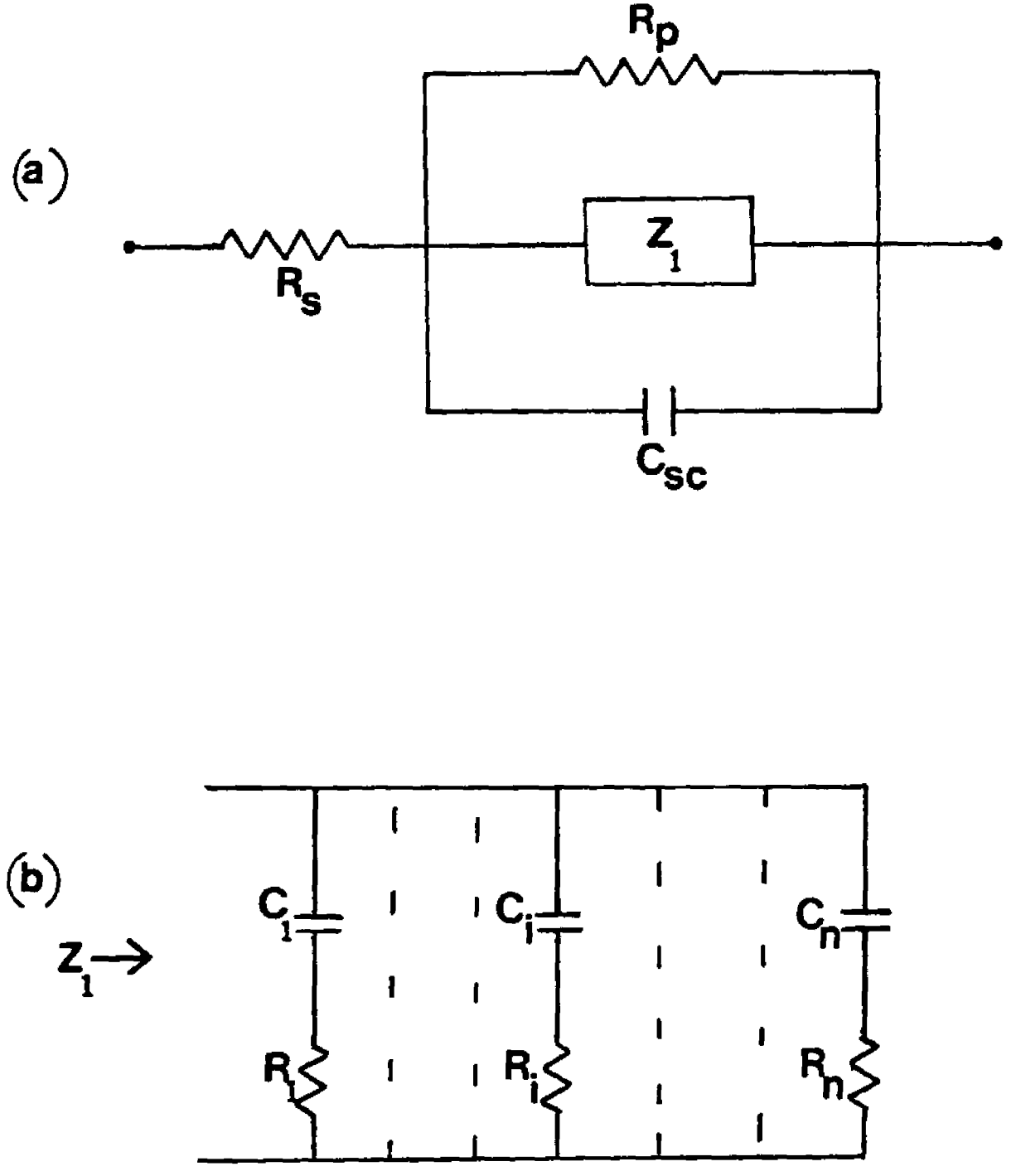

Fig. 2.1 Equivalent circuit of the Semiconductor/Electrolyte interface. For more detials see the text.

general equivalent circuit in which the total charge is shared among all the charge accumulation modes [70,74]. C_{sc} represents the space charge layer capacitance, and R_s is the series resistance associated with the resistance of the semiconductor and the electrolyte. R_p is the resistance associated with the Faradaic current flow across the interface. Z_1 is the impedance of the other possible charge accumulation modes. These may originate from the presence of surface states at the interface or may result from the presence of an another space charge layer with a different doping density than the major space charge layer [70]. Hence, Z_1 may contain more than one RC element (see Fig. 2.1 (b)), depending upon the relaxation time of each accumulation mode. However, it has to be noted here that in Fig. 2.1 the Helmholtz layer capacitance (C_H), which should be in series with the entire equivalent circuit, is not shown for the reason that, in general, $C_H >> C_{sc}$ and we are therefore measuring C_{sc} experimentally as the total series capacitance. However, if this condition no longer be true, then a correction due to C_H should be made [24,75].

Fig. 2.2 shows schematically the experimental setup employed for the relaxation spectrum analysis technique [70]. A frequency synthesizer (hp 3320-B) produces an a.c. signal that is superimposed on the d.c. bias voltage (Fig. 2.2). Two signals originating at A and B are seperately fed into the two channels of the gain phase meter (hp 3575-A), which

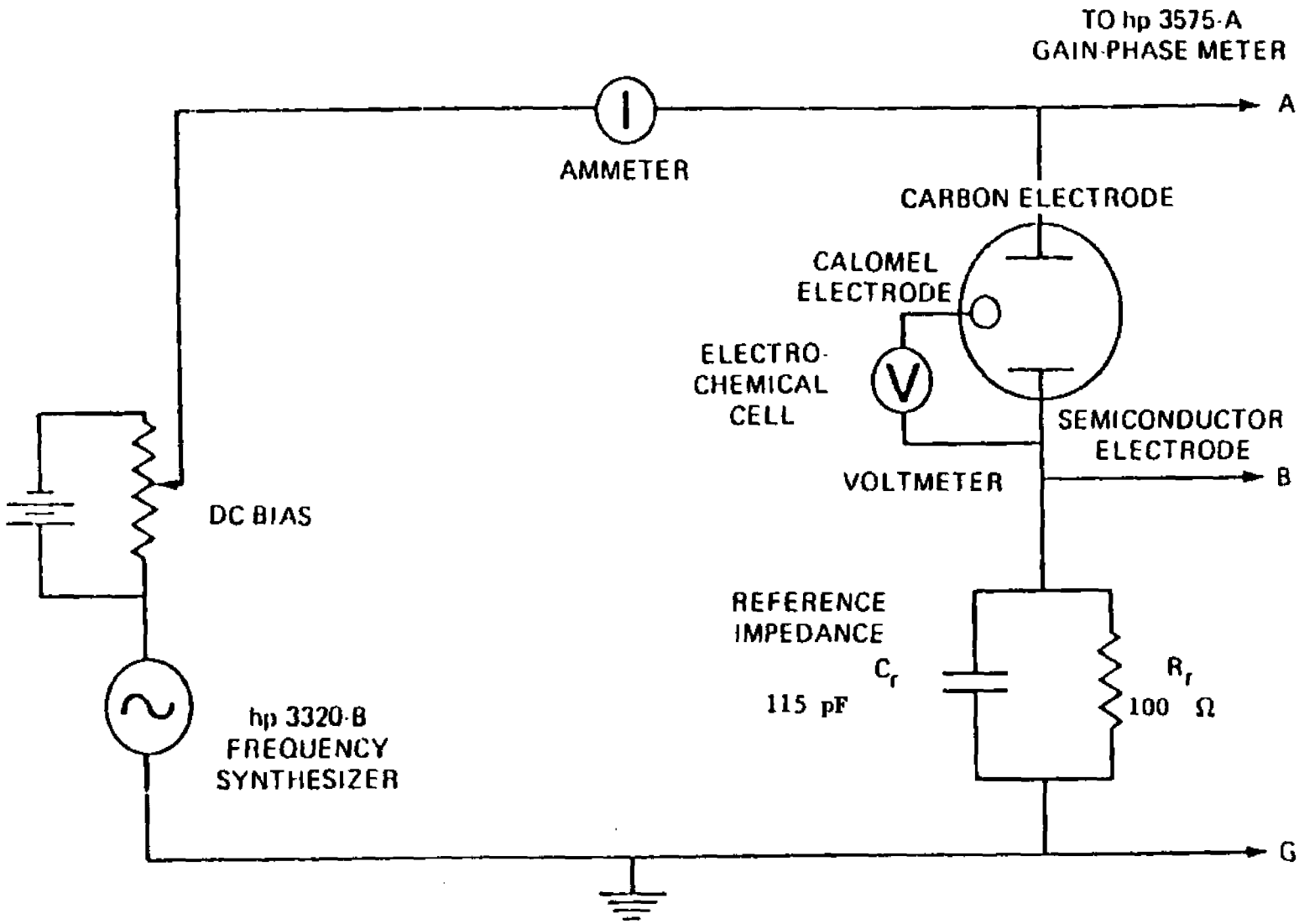

Fig. 2.2 Schematic diagram of the experimental set up of relaxation spectrum analysis technique. (Ref. 70)

measures their relative magnitudes, M, and the phase difference, θ . This measurements is equivalent to the complex voltage ratio between the two signals at A (E_A)and at B (E_B), which can be expressed as:

$$\frac{E_B}{E_A} = \frac{Z_r}{Z + Z_r} \tag{2.1}$$

where Z and Z_r are the impedance of the elctrochemical cell and the reference circuit, respectively. We can write:

$$Z = R + jX \tag{2.2}$$

and

$$Z_r = R_r - j/C_r\omega \tag{2.3}$$

and then from Equation 2.1:

$$R = \frac{R_r}{1+(\omega\tau_r)^2}\left[\frac{\text{Cos }\theta}{M} - \frac{\omega\tau_r \text{ Sin }\theta}{M} - 1\right] \tag{2.4}$$

and:

$$X = \frac{R_r}{1 + (\omega\tau_r)^2}\left[\omega\tau_r - \frac{\sin\theta}{M} - \frac{t_r \cos\theta}{M}\right] \qquad (2.5)$$

where ω is the angular frequency, θ is the phase angle, M is the relative magnitude, and $\tau_r = C_r R_r$ is the relaxtion time of the reference circuit.

Experimentally we can determine R and X as functions of ω . As an example, we have shown in Fig. 2.3, the results for a test circuit given in the original paper by Tomkiewicz [70]. The frequency dependence of curves I and II in Fig. 2.3 can be understood by examining the the different relaxation times of each component in the curcuit. In general, for sufficiently concentrated electrolytes, the space charge layer has the smallest time constant, $R_s C_{sc}$. In the high frequency range, the system behaves as a single capacitor (C_{sc}) and resistor (R_s) connected in series. The impedance of the cell, in this frequency range, is given by:

$$Z_{HF} = R_s - j/\omega C_{sc} \qquad (2.6)$$

Thus, R being independent of ω and deteriming R_s, curve I in Fig. 2.3. Also, X must be inversely proportional to ω , i.e., the plot of $\log(2\pi X)$ vs $\log(f)$ must be a straight

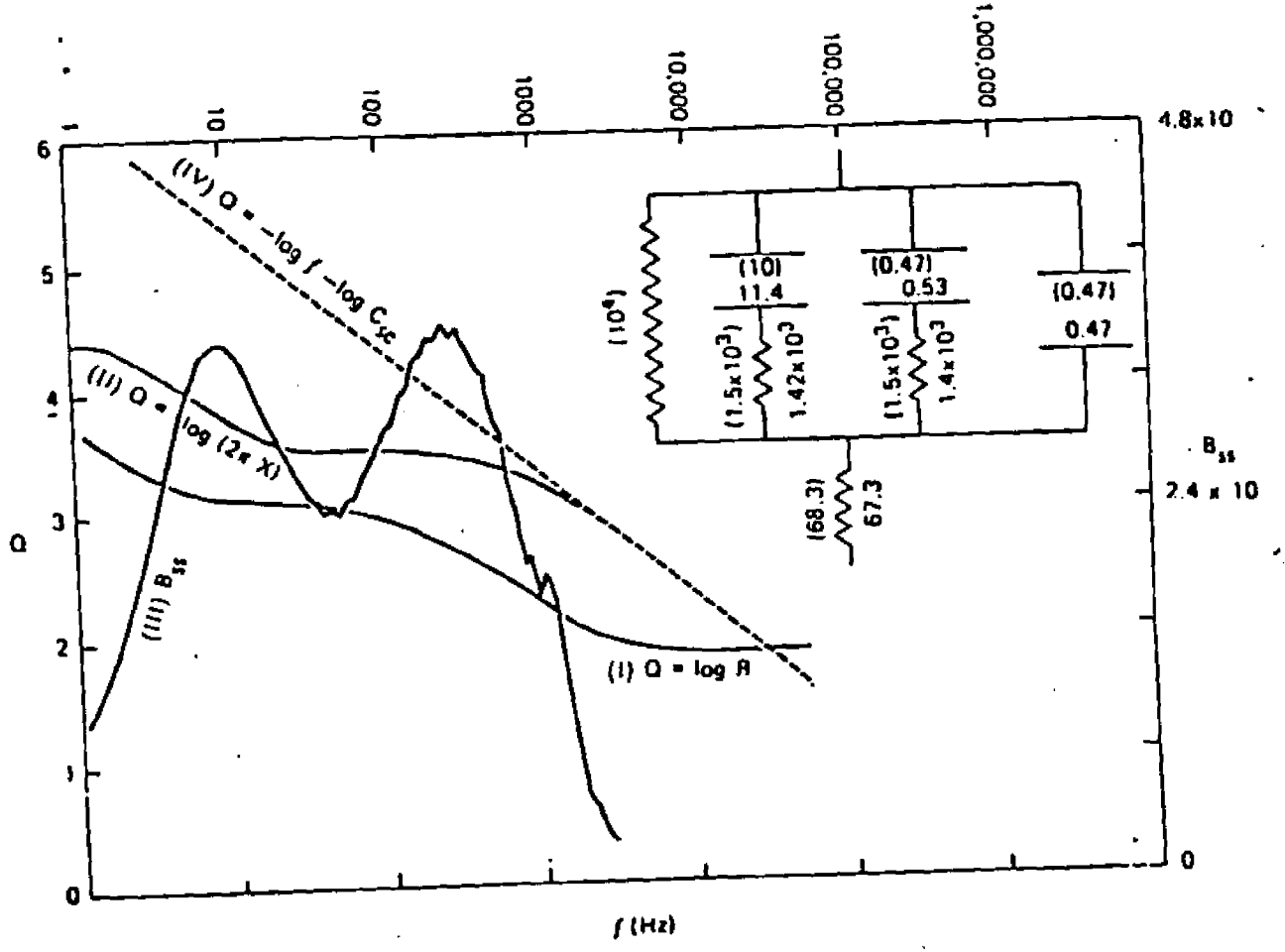

Fig. 2.3 Frequency response curves for model circuit shown at the right hand corner. In parantheses are shown the values of the various elements taken at their stated values. Below them are the values measured from the response curves. (Ref. 70).

of slope one, and the intercept should determine C_{sc}, curve II in Fig. 2.3. In the low frequency range, other elements in the equivalent circuit will also respond to the applied a.c. signal.

Now we can substract the series resistance (R_s) from the total impedance to obtain

$$\begin{aligned} Z' &= Z - R_s = R - R_s + jX \\ &= R' + jX \end{aligned} \tag{2.7}$$

with the admittance given by:

$$\begin{aligned} Y' &= \frac{1}{R' + jX} = \frac{R' - jX}{(R')^2 + X^2} \\ &= G + jB \end{aligned} \tag{2.8}$$

From the equivalent circuit given in Fig. 2.1:

$$G = \frac{1}{R_p} + \sum_{i=1}^{n} \frac{\omega^2 C_i \tau_i}{1 + (\omega \tau_i)^2} \tag{2.9}$$

and

$$B = \omega C_{sc} + \sum_{i=1}^{n} \frac{\omega C_i}{1 + (\omega \tau_i)^2} \qquad (2.10)$$

where $\tau_i = C_i R_i$ is the time constant of the i^{th} element. Since we know C_{sc} from the high frequency response curve, we can substract ωC_{cs} to obtain:

$$B_{ss} = \sum_{i=1}^{n} \frac{\omega C_i}{1 + (\omega \tau_i)^2} \qquad (2.11)$$

Thus, as determined by the Equation 2.11, the variation of B_{ss} with ω gives a superposition of Lorentzian line shapes, curve III of Fig.2.3. If the overlap between the curves is small, or in other words, if each element has different relaxation time, then we should get a series of maxima that completely characterize each RC element.At the maximum of i^{th} peak, $\omega = \omega^i_{max}$, and

$$\frac{\partial B_{ss}}{\partial \omega} = \sum_{i=1}^{n} \left\{ \frac{C_i}{1 + (\omega \tau_i)^2} - \frac{2\omega^2 C_i^2 \tau_i^2}{\left[1 + (\omega t_i)^2\right]^2} \right\} = 0 \qquad (2.12)$$

Since each peak is independent of the other, each term in Equation 2.12 should vanish. Thus:

$$\omega^{i}_{max}\ \tau_i = 1 \tag{2.13}$$

Also from equation 2.11:

$$\begin{aligned} B^{i}_{ss} &= \text{height of the } i^{th} \text{ peak } (H_i) \\ &= \omega^{i}_{max}\ C_i/2 \end{aligned} \tag{2.14}$$

Thefore,

$$C_i = 2\ H_i/\ \omega^{i}_{max} = H_i/\ \pi\ f^{i}_{max} \tag{2.15}$$

and

$$R_i = 1/\ (2\ H_i) \tag{2.16}$$

Hence, each peak in B_{ss} determines the equivelent RC element. In Fig. 2.3 the calculated values are listed in parentheses with stated values of the test circuit [70].

Using this technique we can study the potential behavior of each capacitive element in an electrochemical cell. For heavily doped semiconductors , C_{sc} should follow the Mott-Shottky relation, and the Mott-Shottky plot would enable us to determine the flatband potential and the doping level of

the samples. The surface state capacitance, which is determined by the parallel RC elements in the eqivalent circuit, can be used to evaluate the surface state density distribution at the interface in the following manner.

The total charge on a surface state can be written as:

$$Q_{ss} = \int_{E_v}^{E_c} e\, N_{ss}(E)\, f(E,E_{Fn})\, dE \qquad (2.17)$$

where $N_{ss}(E)$ is the surface state density distribution and $f(E,E_{Fn})$ is the Fermi-Dirac distribution function. It is assumed that the occupancy of the surface states is determined by the Fermi level at the surface, E_{Fn}, a fuction of the applied potential. A small change in E_{Fn}, i.e., a modulation of applied bias by ΔV, can be written as:

$$\Delta E_{Fn} = e\, \Delta V \qquad (2.18)$$

Then,

$$\Delta Q_{ss} = e\, N_{ss}(E_{Fn})\, \Delta E_{Fn}$$

$$= e^2\, N_{ss}(E_{Fn})\, \Delta V \qquad (2.19)$$

Therefore, the differential capacitance of the surface states (C_{ss}) can be written as [24,64]:

$$C_{ss} = \frac{\Delta Q_{ss}}{\Delta V} \simeq e^2 N_{ss}(E_{Fn}) \qquad (2.20)$$

2.2 PHOTOCURRENT SPECTROSCOPY

This experimental technique,which is based on direct measurements of the light-induced photocurrent, has been widely used to study the photoresponse of PEC cells. It has already been established in section 1.3 that the photocurrent is a function of different system parameters, and therefore, by measuring it, informations about the semiconductor/electrolyte interface can be obtained [31,52,62,64]. In addition to the band to band photoexcitations, SBG induced photcurrent can be used to detect surface states and to distinguish them from the bulk midgap states. Two beams experiments, in which the second beam is used for background illumination, have also been used to investigate the interface properties of PEC cells [63,66].

Fig. 2.4 shows schematically the experimental setup employed for the two beams experiments. A 1000 W Xenon lamp (Oriel) with an IR filter made of $CuSO_4$ solution is used for the background illumination. This beam is filtered through a 320 nm band-pass filter, and the intensity is changed using neutral density filters. The scanning beam, obtained from a 150 W Xenon lamp (Oriel), passes through a high intensity Jarrel-Ash monochromator. This beam is chop-

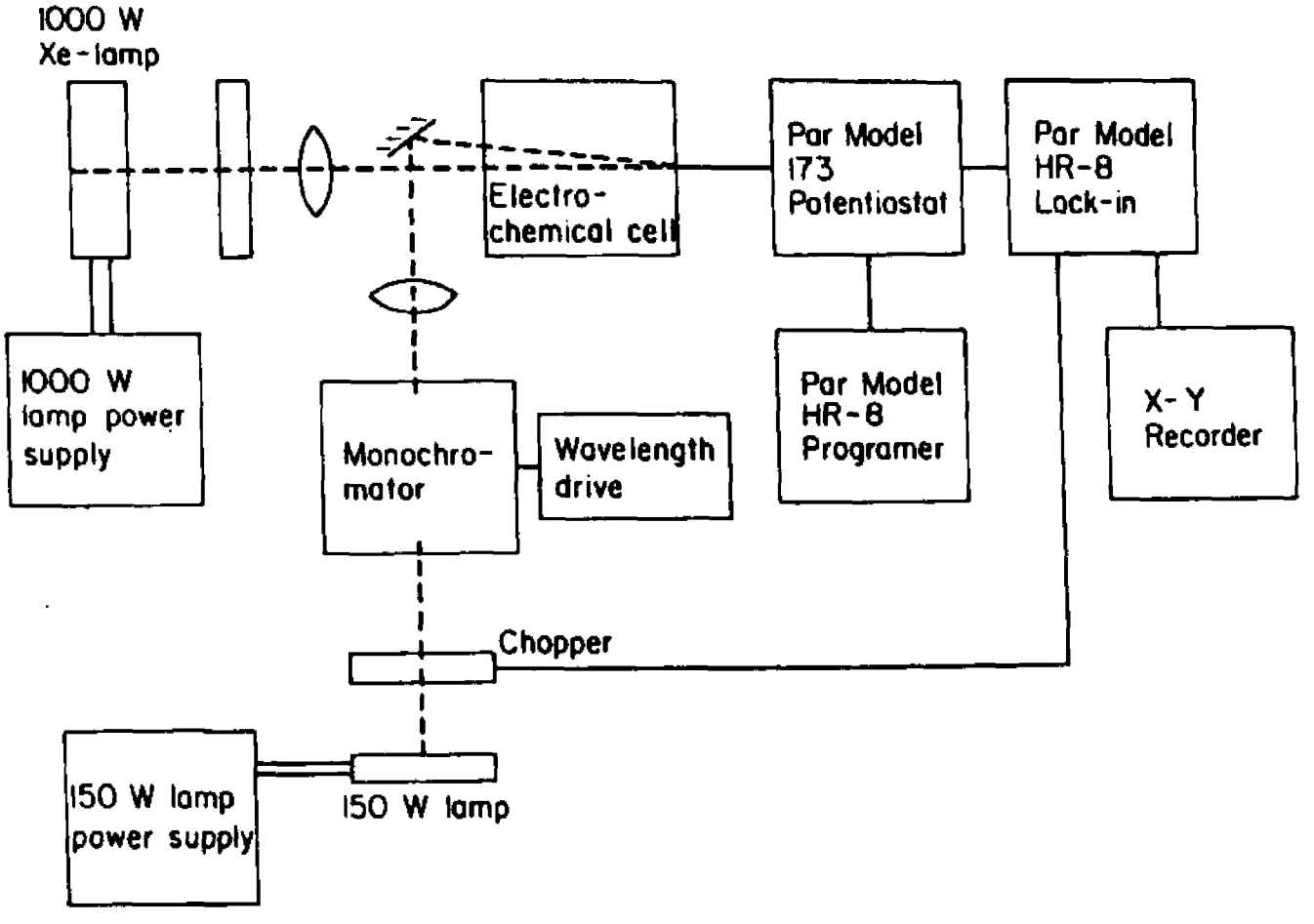

Fig. 2.4 Schematic functional block diagram of two beams experimental set up.

ped with an Ithaco model 382 B chopper. PAR models 173 and 175 potentiostat and programmer are used to operate the electrochemical cell in a potentiostatic mode. The output of the current to voltage converter is fed into the input of a PAR model HR-8 lock-in amplifier with a reference signal taken from the chopper, to measure the photocurrent signal by phase sensitive detection method. In normal photocurrent detection measurements, the experimental setup is the same as in Fig. 2.4, except for absence of background illumination.

2.3 ELECTROLYTE ELECTROREFLECTANCE SPECTROSCOPY

Electroreflectance (ER) is the measurement of electric field modulated reflectivity , and it has been widely used to investigate the optical properties of solids [76]. In the EER technique, a uniform electric field is applied to the surface of the solid by immersing the solid in an appropriate electrolyte [77]. The electric field is modulated by an a.c. signal, and then the electric field modulated reflectivity is measured. The relationship between the observed ER signal and the applied field is very well established under well defined conditions [76-79].

The fundamental quantity that describes the optical response of the material is the complex dielectric function [15]:

$$\varepsilon(\omega) = \varepsilon_1(\omega) + i\varepsilon_2(\omega) \qquad (2.21)$$

For near normal incidence, the reflectivity at the boundary surface seperating two media can be written using the Fresenel's equations [15] as:

$$R = \left| \frac{(n-n_a)}{(n+n_a)} \right|^2 \qquad (2.22)$$

where $n^2 = \varepsilon$ and $n_a^2 = \varepsilon_a$, and n and n_a are refractive indices of the material and the ambient (electrolyte), respectively. Experimentally, R shows peaks in the spectrum that can be attributed to direct interband transitions at points on $\vec{k}$ space, critical points, at which the combined density of states for optical transition has a singularity [15],

$$\nabla_{\vec{k}} \left(E_c(\vec{k}) - E_v(\vec{k}) \right) = 0 \qquad (2.23)$$

In ER, these critical points can be observed directly.

The unpertubed dielectric function (Equation 2.21) is perturbed by the applied electric field; ε_1 and ε_2 are changed by $\Delta\varepsilon_1$ and $\Delta\varepsilon_2$, and hence R is changed by ΔR. In ER, this relative change in reflectance, $\Delta R/R$, is measured. At sufficiently low values of the modulating electric

field (low-field regime) the ER signal for the fully depeleted space charge layer is given by [80,87]:

$$\frac{\Delta R}{R} = - (2eN_D V_{sc}/\epsilon_s) L(\hbar\omega) \qquad (2.24)$$

where V_{sc} is the fundamental harmonic component of the applied voltage across the space charge layer and ϵ_s is the static permitivity. The quantity $L(\hbar\omega)$ is a spectral lineshape function determined by the electric field distribution and properties of the material.

The spectral lineshape for each critical point in the low-field regime is given by [78]:

$$\frac{\Delta R}{R} = Re \left[C e^{i\theta} (E - E_g + i\Gamma)^{-n} \right] \qquad (2.25)$$

where E_g, C, and θ are the energy gap, amplitude, and the phase factor, respectrively, Γ is the broadening parameter, and $n \geqslant 2$, which is characteristic of the critical points for simple parabolic modeles (n=3 for a two-dimentional model, n=5/2 for a three-dimentional model, and n=2 for excitons).

Other than the optical properties of solids, the EER technique can be used to investigate the interface properties of semiconductor/electrolyte junction [81]. The flatband potential at the interface could be determined by studying the potential variation of EER signal [81,82]. At flatband, the EER signal should change sign,i.e., it is zero at that potential. Also the potential variation of the EER signal determines the status of the Fermi level in situ in the semiconductor/electrolyte interface [67,68]. At depletion, the EER signal must be independent of the applied d.c. bias [78]. But, if a high density of surface states is present at the interface that are fast enough to equilibrate at the modulation frequency, then only a fraction of the modulation voltage will apear across the space charge layer,resulting in a strong dependance of the EER signal on the d.c. bias [67,68]. Also SBG EER can be used to study the surface states at the solid/electrolyte interface [80-85].

Fig. 2.5 shows schematically the experimental arrangement employed for the EER measurements [77,81]. The light source is a 150 W Xenon lamp (Oriel) or tungston lamp, which is used with a high-intensity monochromator (Heath model EU 700-56) to obtain a monochromatic beam. This beam, with intensity I_o,is focused onto the sample by a focusing lens, and the sample is immersed in an electrolyte contained in a cell with a quartz window. A modulating voltage and the

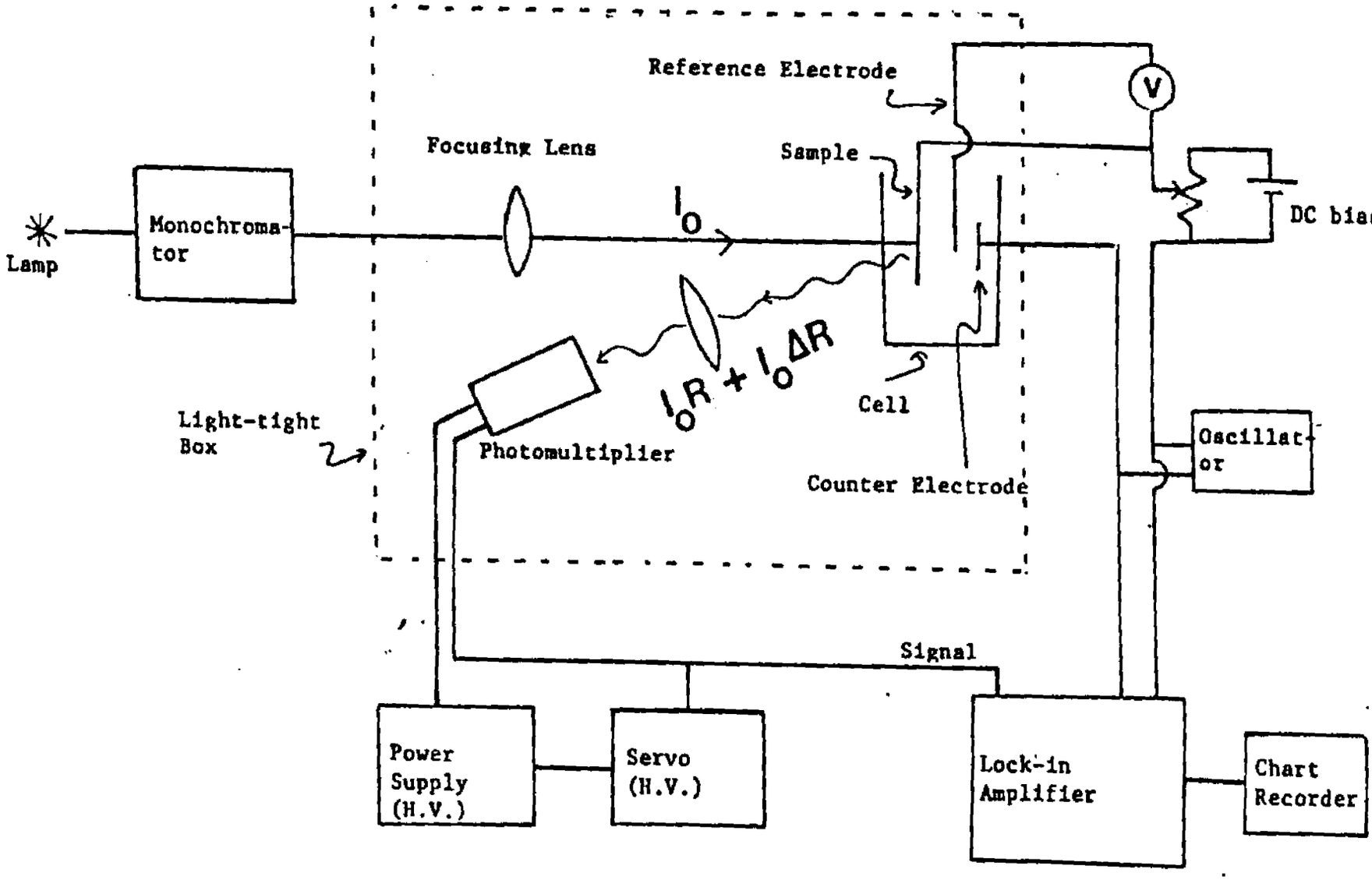

Fig. 2.5 Schematic functional block diagram of EER set up.

d.c. bias is applied between the semiconductor electrode and the counter electrode using a signal generator (hp 3311A). The reflected light from the sample surface is collected by a lens and focused onto the photomultiplier tube.

The reflected light coming onto the photomultiplier tube has two componenets: a d.c. value of $I_o R$ and a modulated value of $I_o \Delta R$. The a.c. component is detected by phase-sensitive detection using a lock-in amplifier (PAR 186-A) with a reference signal from the signal generator. The d.c. output of the photomultiplier is fed into the power supply to adjust the high voltage on the photomultiplier in order to keep the d.c. output constant. In this way the lock-in amplifier measures the realtive change in reflectance $\frac{\Delta R}{R}$ directly.

2.4 SAMPLE PREPERATION AND THE PEC CELL

TiO_2 single crystals were purchased from Atomergic and sawed to expose the (001) surface. The resulting waferes were reduced in a 10% H_2/Ar mixture at 600-850 ^{o}C for 30 min. These samples were then mechanically polished to 0.3 μm, boiled in 1N H_2SO_4 for 30 min and then washed with distilled water. The back contact on the samples were made by rubbing them with In-Ga alloy, and in each case the contact was checked with a curve tracer. The PEC cell shown in Fig. 2.6, constructed by Tomkiewicz [64], was employed. The electrodes were mounted in the cell by pressure fit between two silicon rubber gaskets, which also determined the elec-

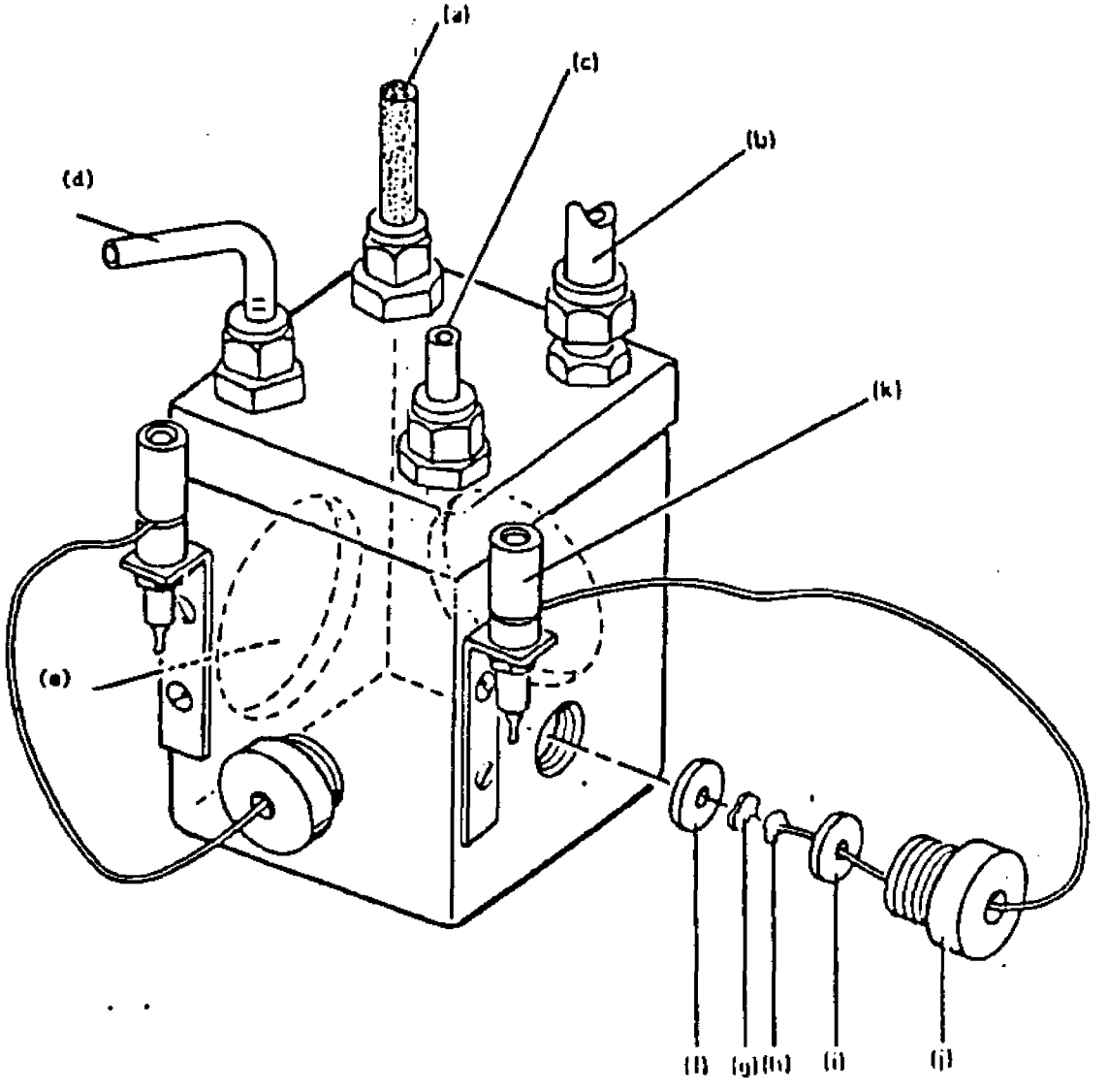

Fig. 2.6 The photoelectrochemical cell: (a) counter electrode; (b) reference electrode; (c) and (d) inlet and outlet for N_2; (e) optical windows; (f) and (i) silicon rubber gaskets; (g) sample; (h) platinum disk; (j) teflon screw; (k) electrical co-nector. (Ref. 64).

trode area that was being exposed to the electrolyte. As shown in Fig. 2.6,

a platinum disk attached to a platinum wire was pressed against the back contact of the sample. All chemicals were analytical grade and were used as such. The experiments were carried out in an oxygen-free enviornment by passing N_2 through the electrolyte. To stabilize the interface prior to each experiment, the semiconductor was allowed to equilibrate with the electrolyte for several hours and was then repetitively scanned beteween anodic and cathodic potentials ($\sim$ 3V) until a reproducible cyclic voltammetry emerged.

The $CdIn_2Se_4$ sample was kindly donated by Dr. R. Tenne (of the Weizman Institute of Science, Rehvolt 76100, Israel). These samples were grown and doped by Dr. W. Giriut (Center de Fisica, Ins. Venz. de Invest Cient., Caracas, Venezuela). The sample was polished to a 1 μm finish and then etched with aqua regia (1:4 HNO_3:HCl mixture). Ohmic contact was made by rubbing In-Ga alloy on the back surface of the crystal, and copper wire was attached to the crystal by means of silver epoxy. The electrode was sealed with an insulating epoxy except on the front surface, and the sample was mounted in an N_2-purged solution of Na_2S:S :NaOH = 1:1:1 M in a sealed plastic cell. A platinum foil was used as the counter electrode. Photoetching was carried out in 10 times diluted aqua regia by connecting the photoelec-

trode and a carbon electrode to a potentiostat and illuminating it at $\sim$ 1 AMI. The elelctrode was photoetched for 30 sec potentiostatically at 1V vs Pt [86].

Chapter III

RESULTS

3.1 IMPEDANCE MEASUREMENTS ON n-TiO_2/AQUEOUS ELECTROLYTE INTERFACE

3.1.1 General Impedance Characteristics of n-TiO_2 Electrodes in a PEC Cell

We have investigated the semiconductor/electrolyte interface of n-TiO_2 electrodes in different aqueous electrolytes by impedance measurements, using the relaxation spectrum analysis technique. Fig. 3.1 shows a typical impedance spectrum obtained for n-TiO_2 electrodes in a phosphate buffer solution. As is evident from this figure, the PEC cell behaves as a single resistor and capacitor in series in the high frequency range (see section 2.1). Also a single Lorentzian lineshape is evident in B_{ss} in the low frequency range.Similar impedance spectra were obtained at different electrode potentials in different electrolytes and for different samples with a wide range of doping densities. It is evident that for this system (n-TiO_2/aqueous-electrolyte interface), the equivalent circuit consists of two parallel RC elements shunted by a resistor.

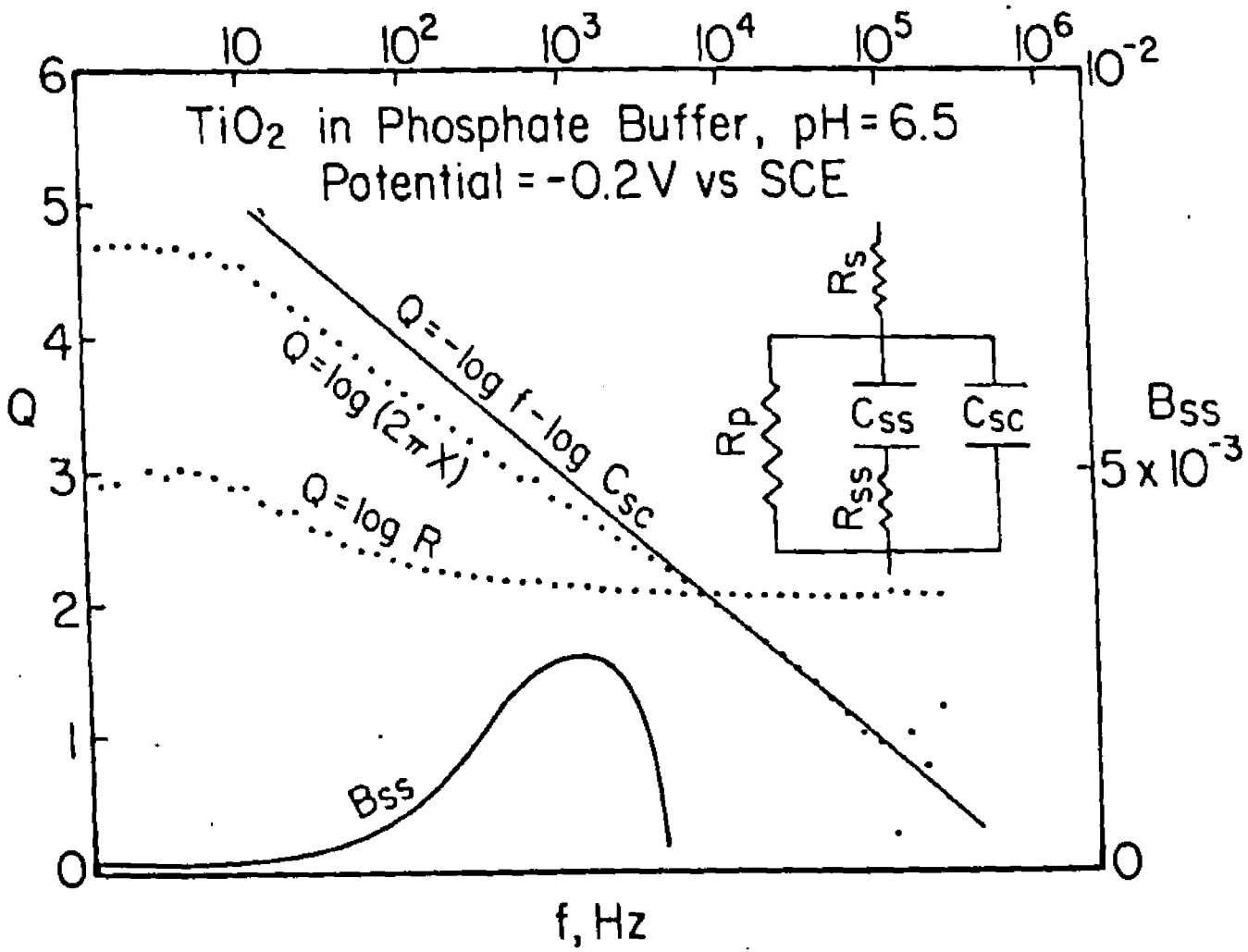

Fig. 3.1 Impedance response curves for n-TiO_2 in 0.33 M phosphate buffer. Sample area = 0.07 cm^2.

3.1.2 Potential Variations of the Space Charge Layer and the Surface State Capacitances

Fig. 3.2 shows the variations of the two capacitive elements, C_{sc} and C_{ss}, with potentials in two different electrolytes, 1M KF and 1M KI. The fastest relaxing capacitive element, C_{sc}, obeys the Mott-Schottky relation in both electrolytes, although the range is more limited in KI than in KF. The slope of the Mott-Schottky plots in both electrolytes is the same from which the doping level of 5×10^{19} /cm^3 was calculated. The slower capacitive element C_{ss}, exhibits significantly more structures. Also, it does not follow the Mott-Schottky relation, which excludes the possibility that the origin of C_{ss} may be due to a space charge layer [70]. Fig. 3.3 shows the similar Mott-Schottky plots and surface state capacitance variations for three different n-TiO_2 samples with the doping density range of 10^{17}-10^{19} /cm^3 in a phosphate buffer solution.

In all the samples and the electrolytes, the dominant state in the surface state capacitance is the one that tails from the conduction band edge, and additional structures apear at 0.8 eV and 1.3 eV below the conduction band. This basic distribution of surface state capacitance was observed with many samples, though the results varied somewhat from sample to sample. This variation is not surprising, however, in view of the anticipated sensitivity of c_{ss} to the surface conditions of the samples. Possible causes for this sensitivity might be the surface heterogeniety, the masking of

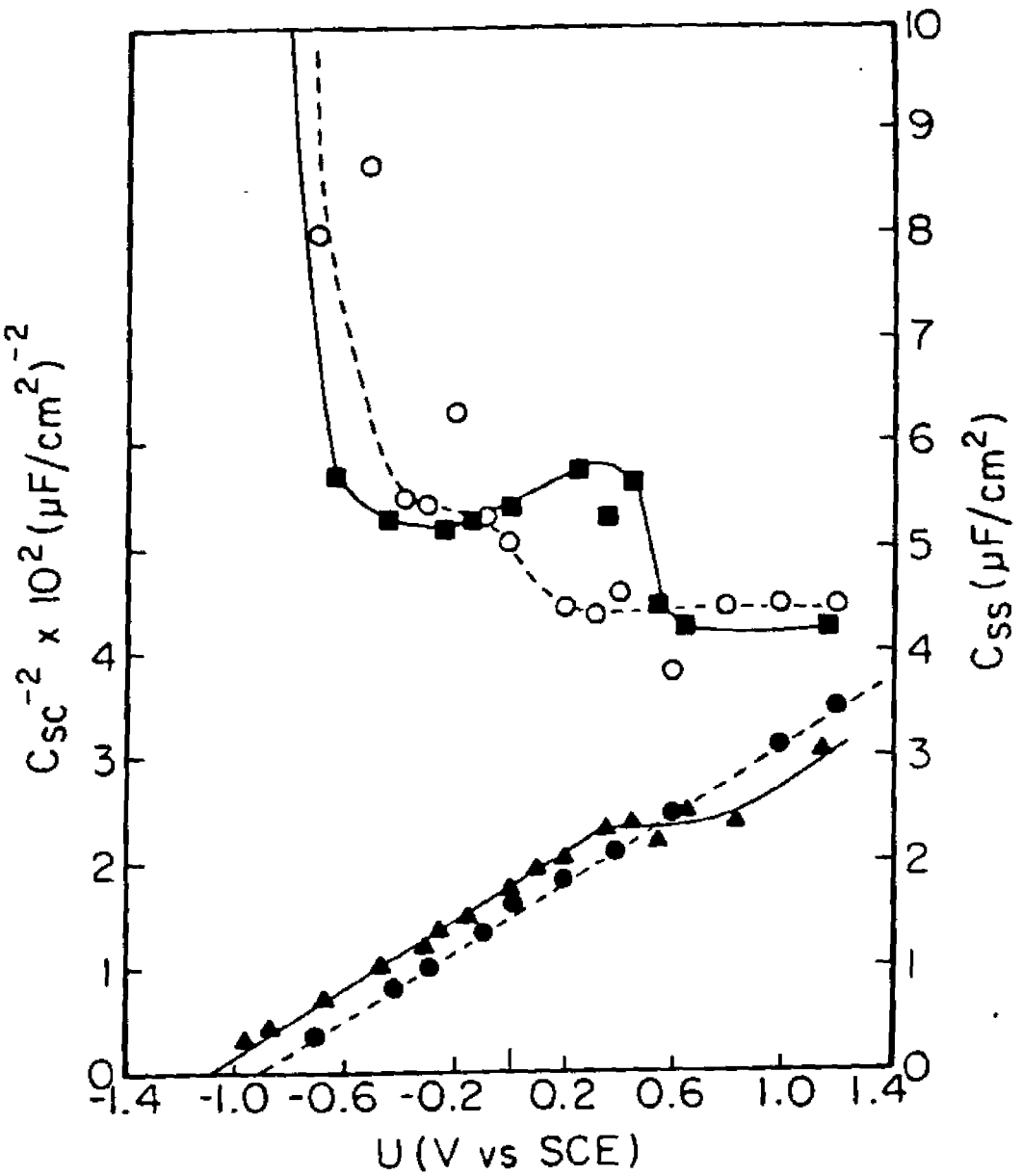

Fig. 3.2 Mott-Schottky plots (left scale) and the surface state capacitance variations with the potential (right scale) for n-TiO_2 in 1M KI and KF.
C_{sc}: ▲, 1M KI; ●, 1M KF.
C_{ss}: ■, 1M KI; o, 1M KF.

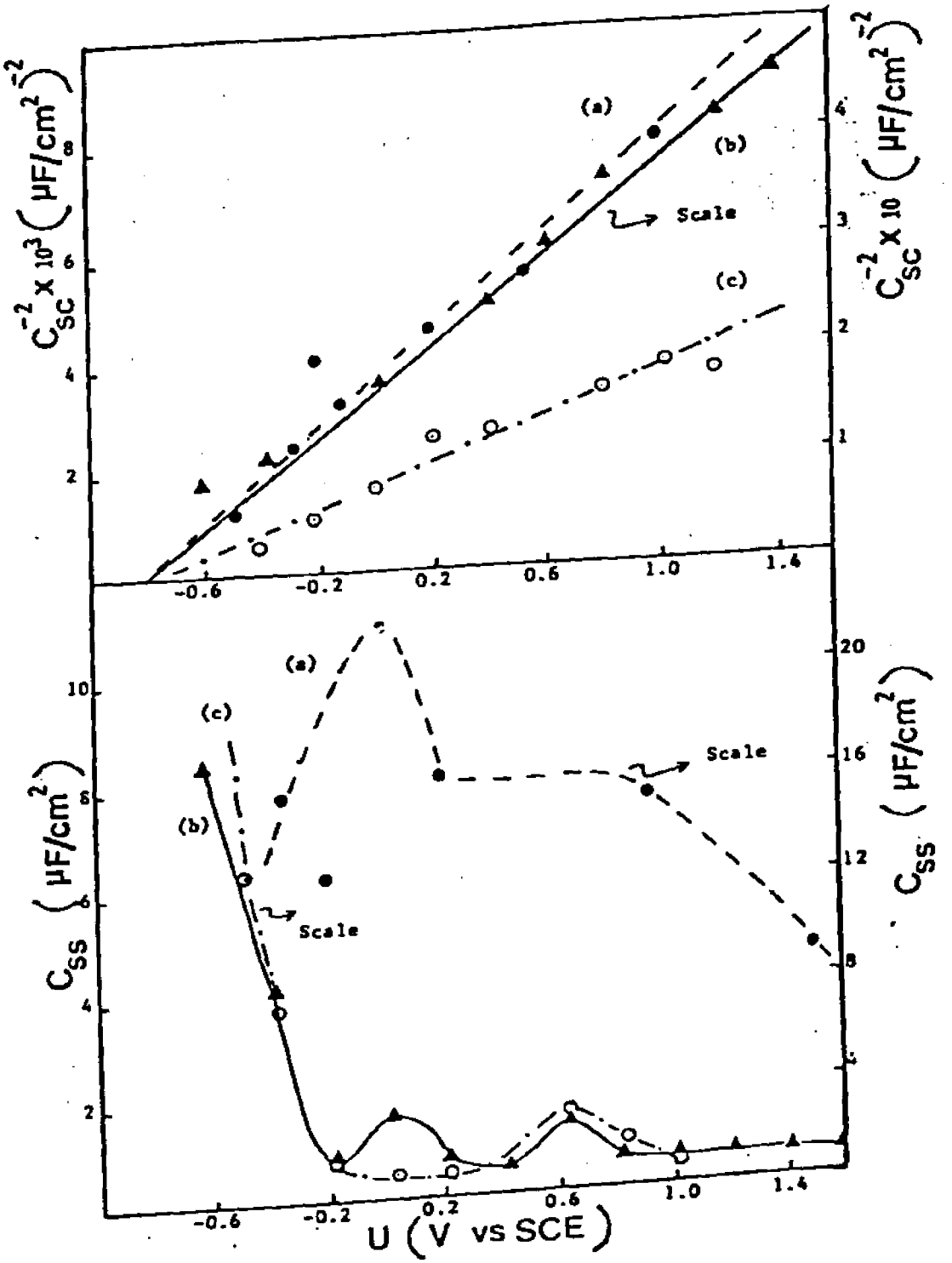

Fig. 3.3 Mott-Schottky plots (top) and surface state capacitance variations with potential (bottom) for three different n-TiO_2 samples in phosphate buffer.

one surface state by the other (e.g.,in Fig. 3.2, the surface state at 0.8 eV is masked by the surface state at 1.3 eV in KI), and a space charge layer capacitance with a different doping density [70], which could mix with the surface state capacitance if the relaxation times for both are in the same order.

3.2 EER MEASUREMENTS ON n-TiO_2 IN DIFFERENT ELECTROLYTES

An EER study was carried out in both the bandgap and the SBG energy regions of TiO_2 in different electrolytes. Unless otherwise specified, all measurements were taken with a modulating voltage of 200 mV peak to peak at the frequency of 83 Hz.

3.2.1 Bandgap EER

Fig. 3.4 shows the bandgap EER spectra for TiO_2 in the electrolyte 1M KI. Similar spectra were obtained in the other electrolytes, 1M KF and 1M KBr, and the phosphate buffer. Different halogens were chosen in order to study the semiconductor/electrolyte interface with different electrolyte species adsorbed on the electrode surface. The spectra shown in Fig. 3.4, a strong peak around 4 eV, agree well with the published literature [88,89]. Fig. 3.5 shows the variation of the 4 eV peak amplitude with the electrode potential in 1M KI and 1M KF. The potential in which EER amplitude changes sign, the flatband potential has shifted by 0.2 V in

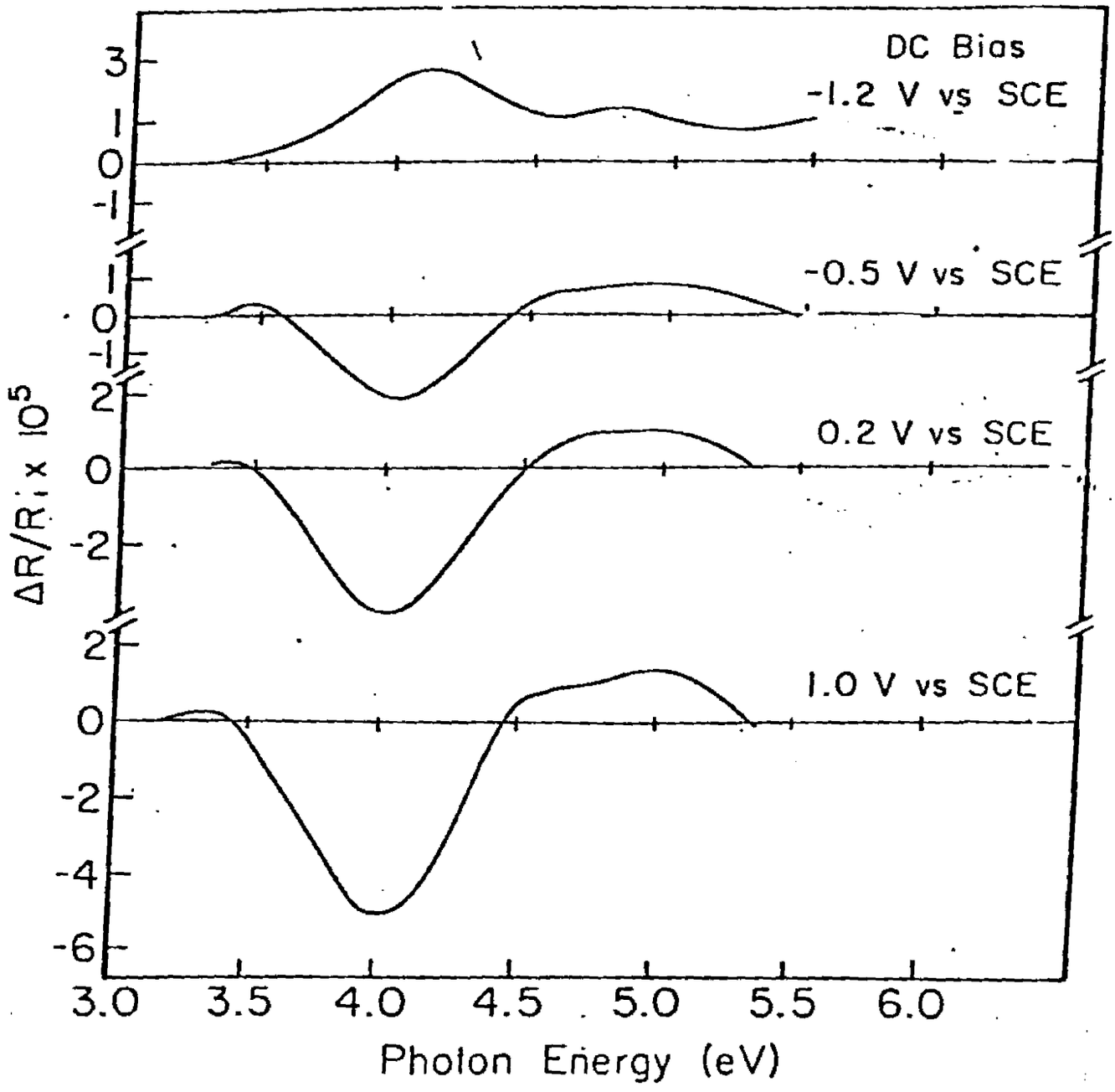

Fig. 3.4 EER spectra for TiO_2 in 1M KF.

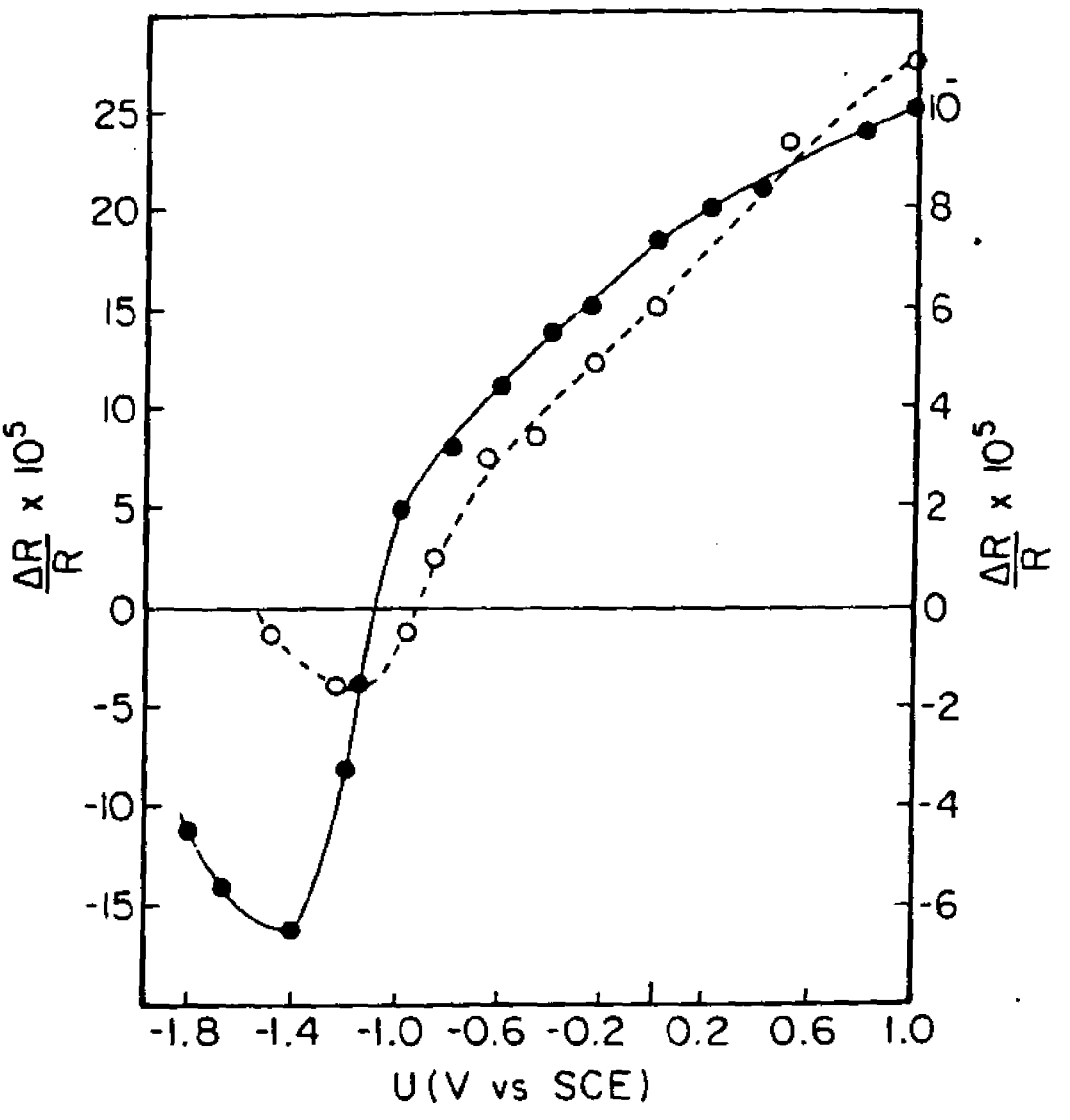

Fig. 3.5 Variation of the EER signal, photon energy 4 eV, with the potential for n-TiO_2 in 1M KI (left scale, ——) and 1M KF (right scale, ---).

KI, which is in good agreement with the data given in Fig. 3.2.

3.2.2 Sub-Bandgap EER

We have investigated the possibility of applying the EER technique to determine the surface states at the n-TiO_2/aqueous-elelctrolyte interface, and studied the SBG energy range in EER. Fig. 3.6 shows the SBG EER obtained for n-TiO_2 in a phosphate buffer. The broad peak around 1.3 eV is evidently independent of the applied bias voltage, though the amplitude strongly depends on it. As shown in the inset of Fig. 3.6, the SBG peak position is also independent of the doping density. The structure of SBG EER that we observed here is different from the ones previously reported [84]. The major difference is the independence of the peak position in relation to the electrode potential, within the voltage range where the structure could be observed. This result, along with the above mentioned independence in relation to the doping density, are crucial in determining that EER is not due to an interference effect. In the SBG energy range, it has already been reported that interference between the light reflected from the surface and the back of the space charge region for $SrTiO_3$ [90]. If the SBG EER structure that observed in TiO_2 is caused by such interference, the peak position should strongly depend on the thickness of the space charge layer. But, as shown in Fig. 3.6,

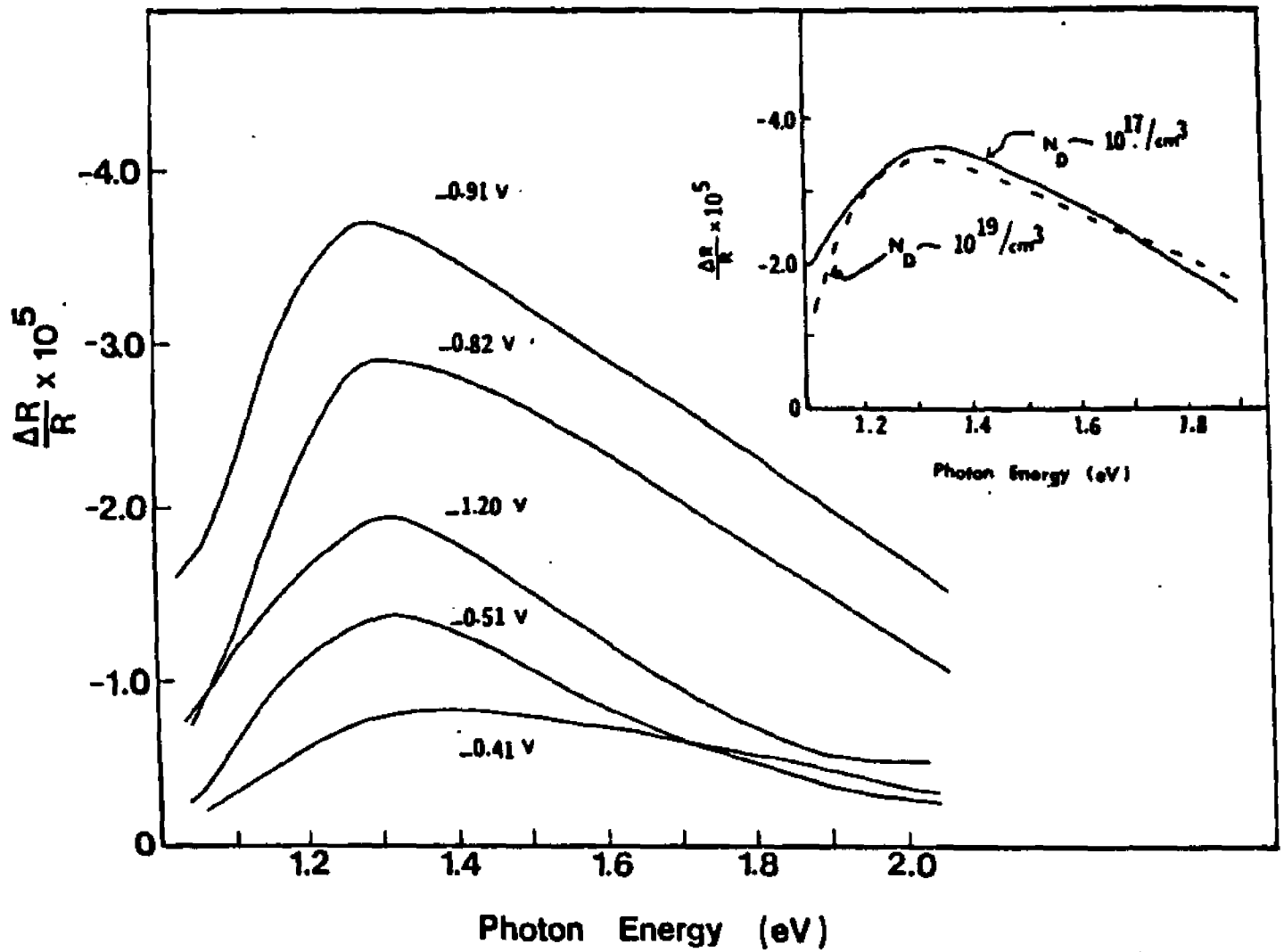

Fig. 3.6 SBG EER spectra for n-TiO_2 in phosphate buffer as a function of the electrode potential. Insert shows two spectra for two samples with different doping densities.

this is not the case here. Therefore, there is conclusive evidence here that the structure appearing in the SBG EER for TiO_2 can not be the result of the interference.

Fig. 3.7 shows the sensitivity of the SBG EER signal to the ambient in various electrolytes. The ionic strength of solutions was kept constant and all spectra were taken at the potential which shows the maximum response. The broad peak is centered around 1.3 eV and the peak position does not changed with the electrolyte but the intensity of the peak does. Within the halogen series, it follows the same trend as the expected strength of adsorption if the latter is dominated by substitution of the hydration shell of the ions [91]. Fig. 3.8 shows the variation of the SBG EER peak amplitude with the electrode potential for the various electrolytes. In all cases, the maximum response is 0.1 - 0.3 V more negative than the corresponding flatband potential.

3.3 PHOTORESPONSE AT THE n-TiO_2/ELECTROLYTE INTERFACE

We have investigated n-TiO_2 photoelectrodes in a phosphate buffer solution (pH=6.6), which is an example of photoelectrolytic solar cells. System response to the incident radiation was monitored by measuring the light-induced photocurrent in both the bandgap and the SBG energy ranges. Hence obtained result are presented below.

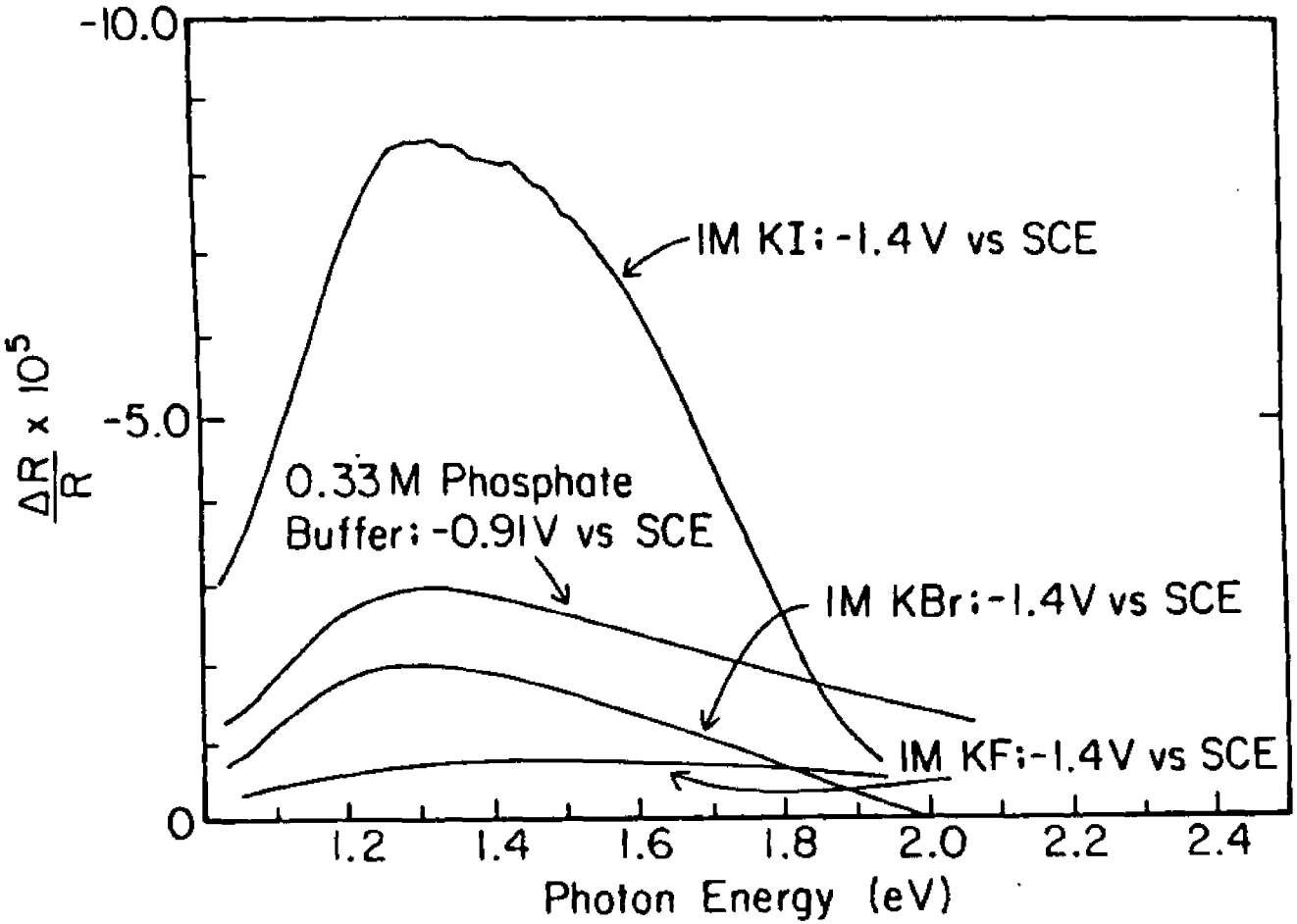

Fig. 3.7 SBG EER spectra for n-TiO_2 in different electrolytes.

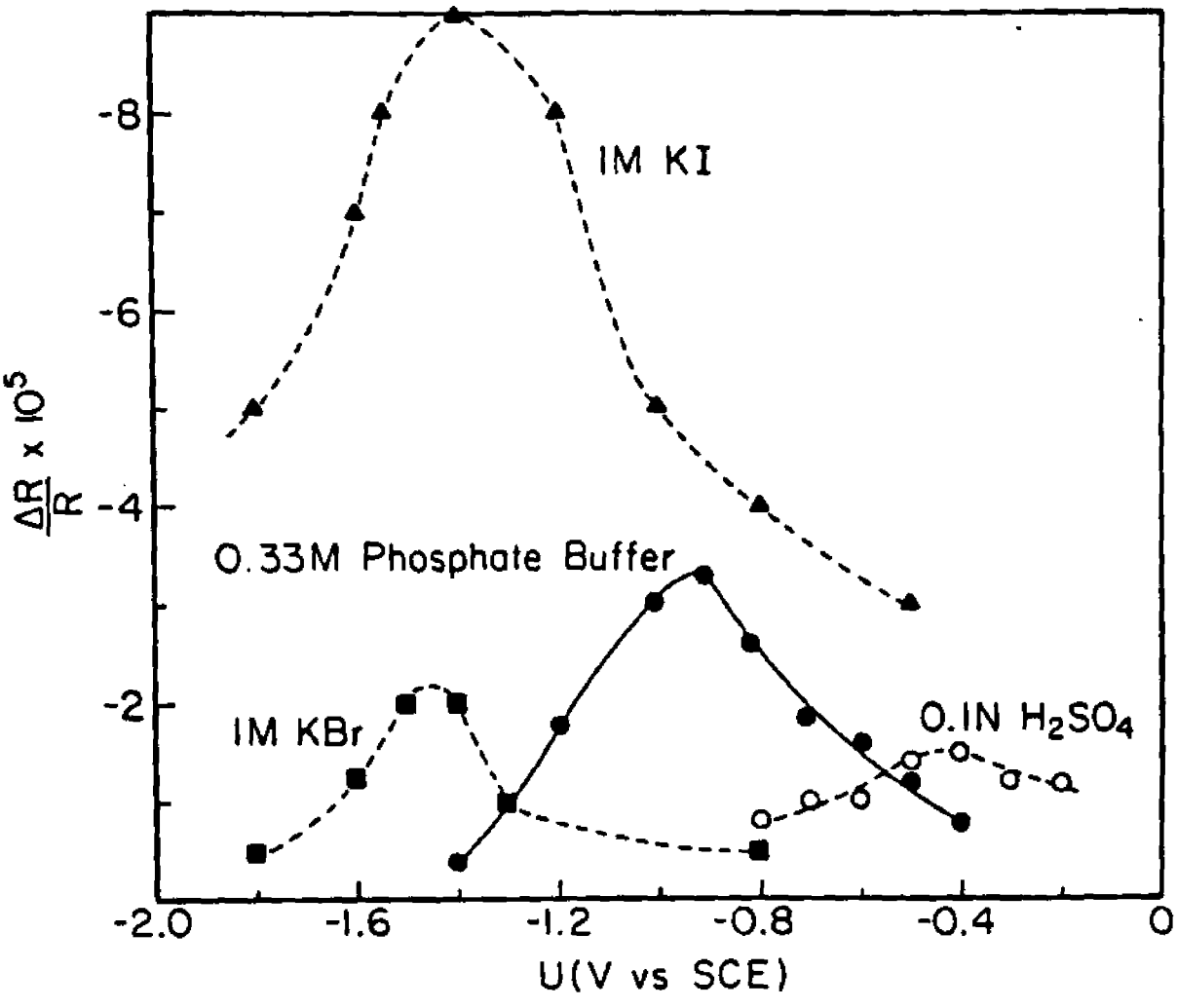

Fig. 3.8 Potential dependence of SBG EER signal (photon energy 1.3 eV) in differnt electrolytes.

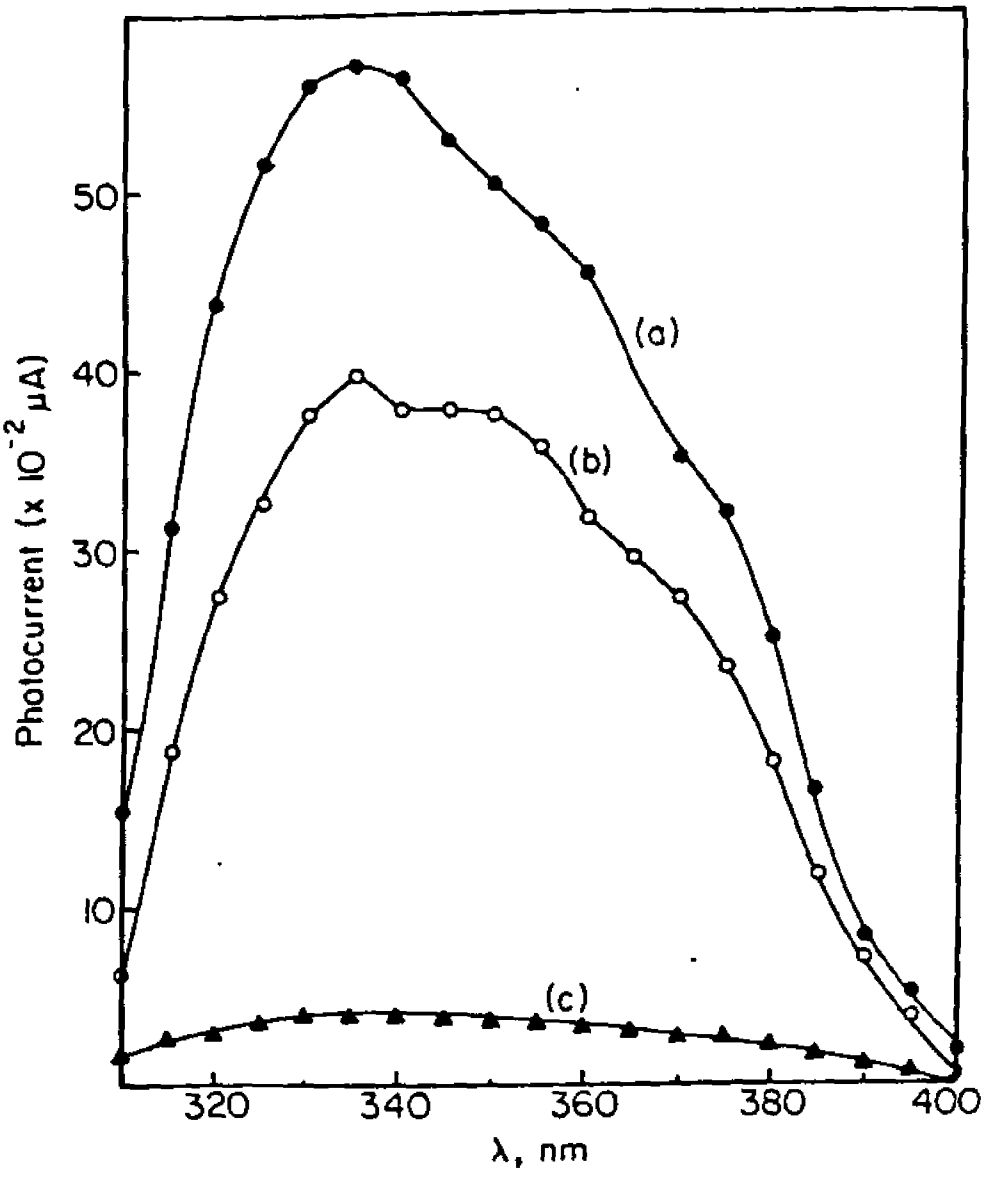

Fig. 3.9 Band to band spectral response for n-TiO_2 in phosphate buffer at different potentials. (a) U= 1.0 (V vs SCE) (b) U= -0.2 (V vs SCE) (c) U= -0.4 (V vs SCE).

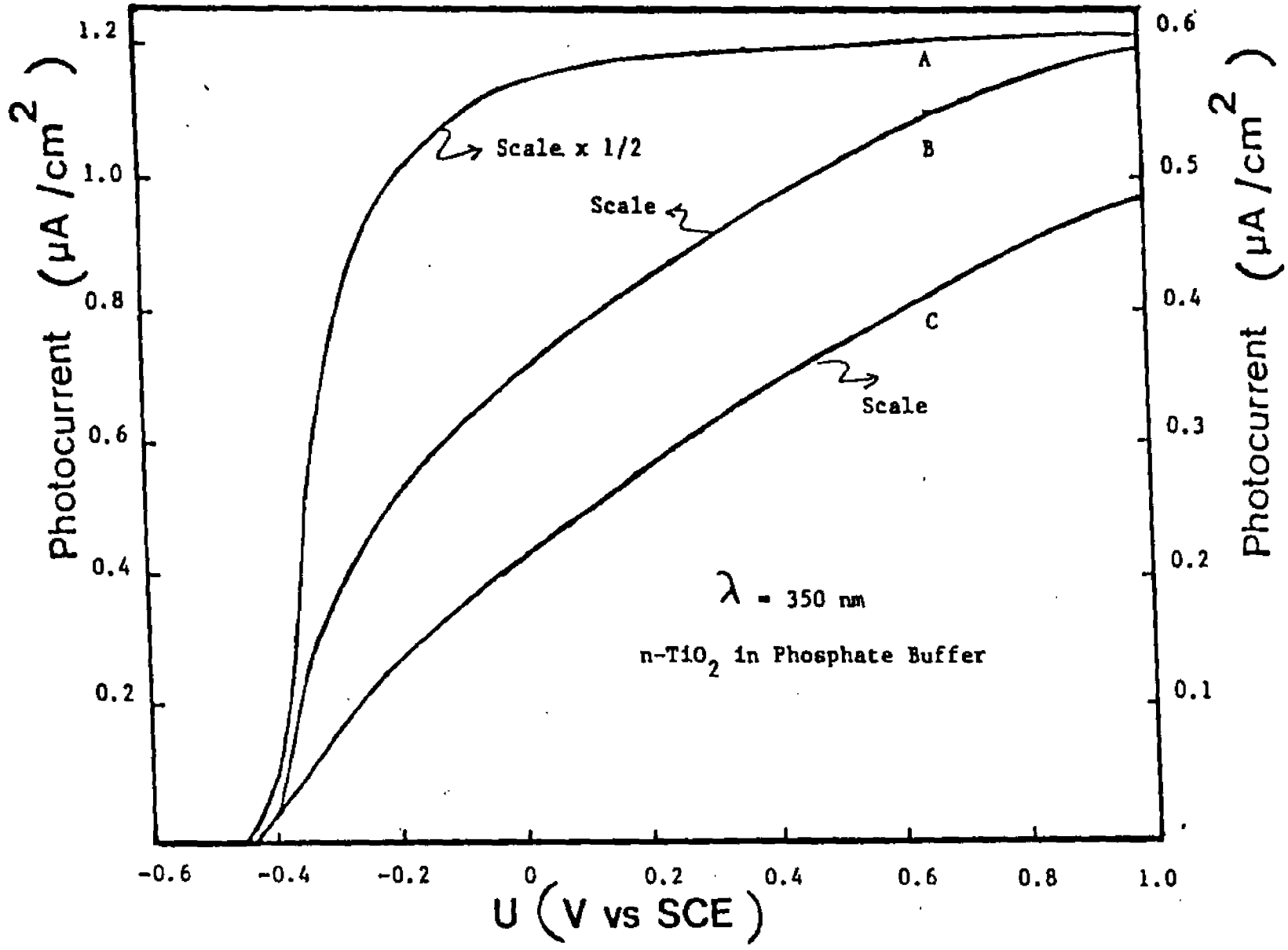

Fig. 3.10 Photocurrent-potential behavior for three different n-TiO_2 samples in phosphate buffer.

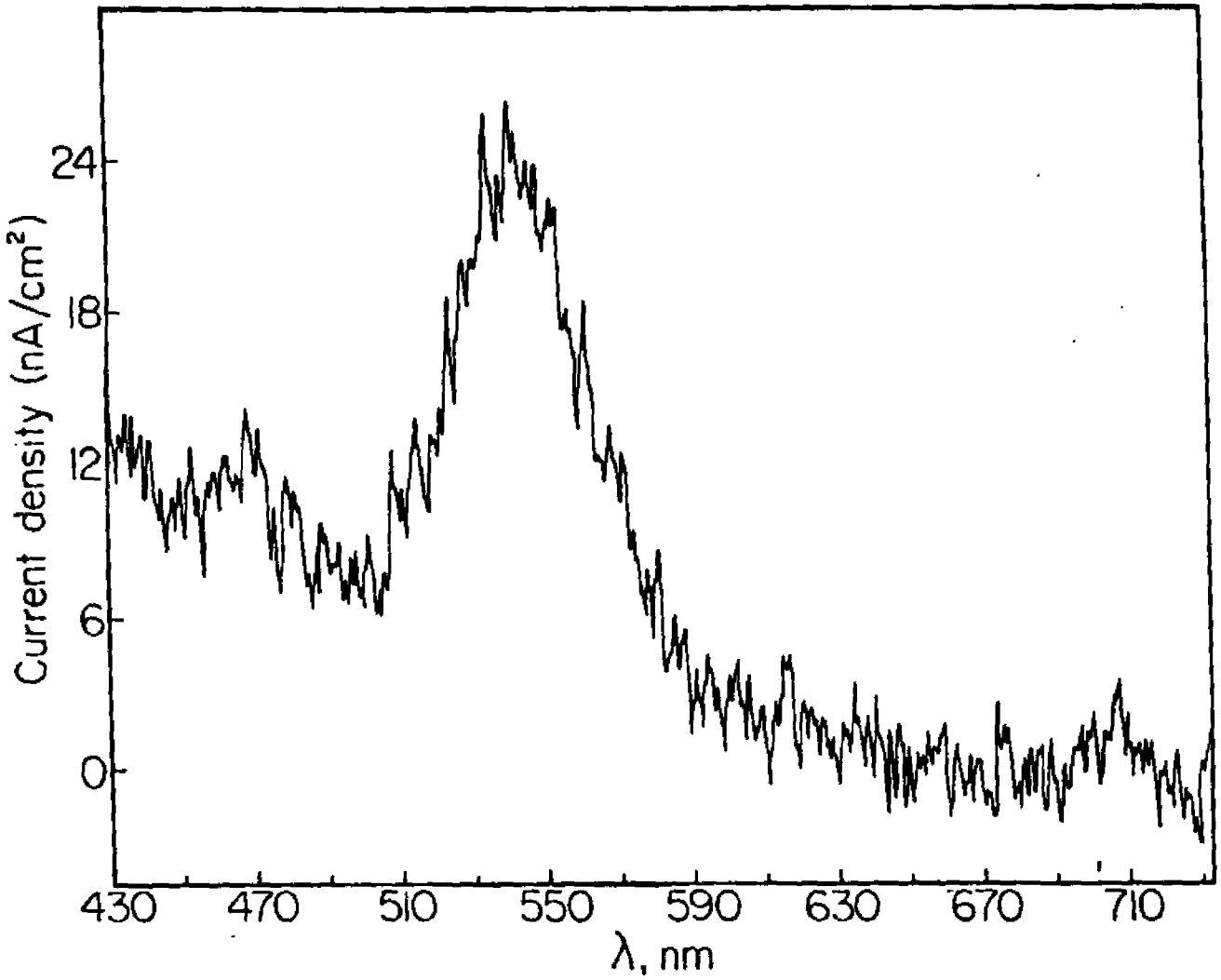
Current density (nA/cm²)
24
18
12
6
0
430
470
510
550
590
630
670
710
λ, nm

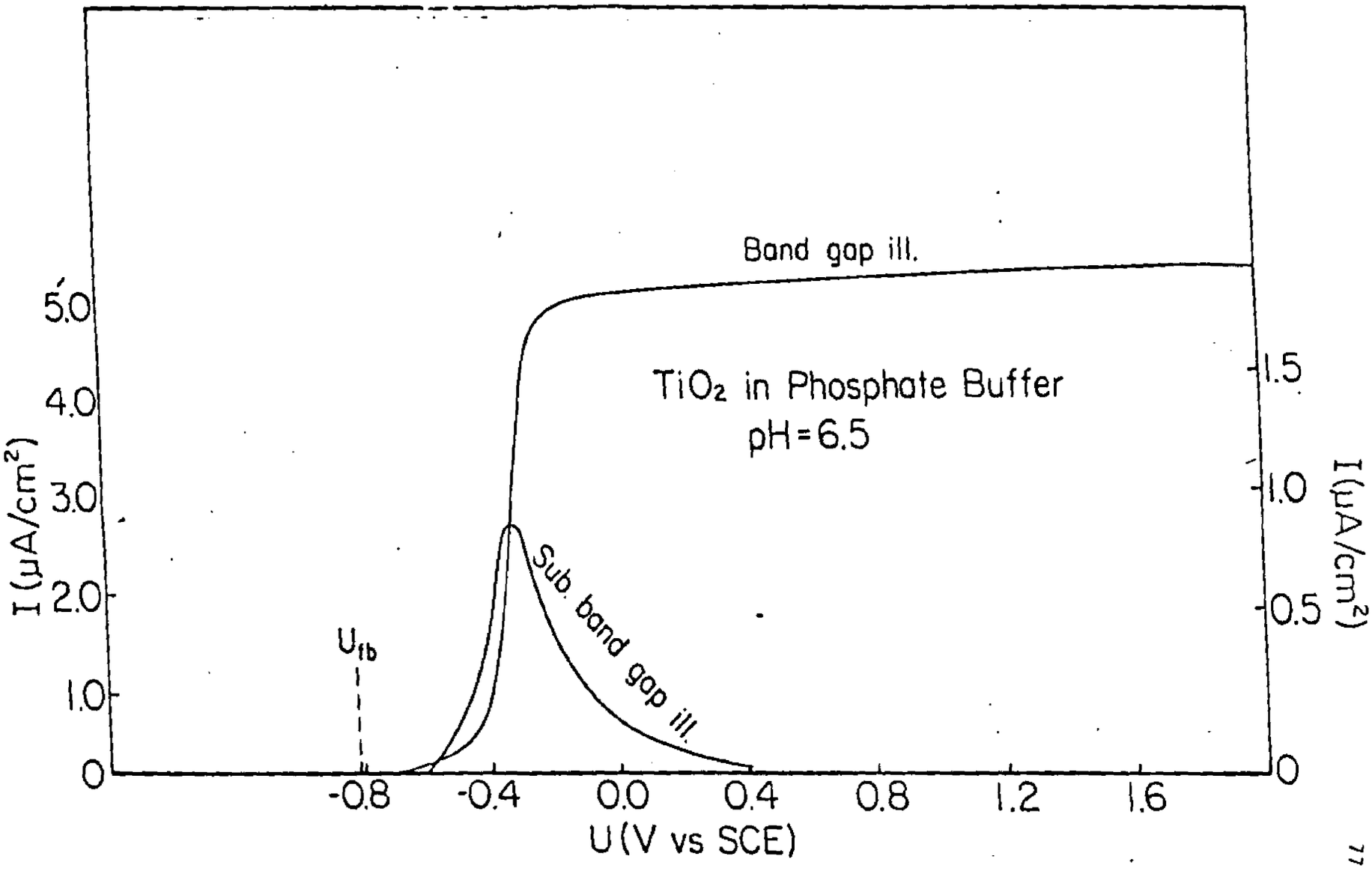

Fig. 3.12 The current-potential behavior of the band to band and SBG photoresponses. Left scale, bandgap illumination.

3.3.1 Bandgap Photocurrent

Fig. 3.9 shows a typical light-induced spectral response obtained for n-TiO_2 photoelectrodes in a phosphate buffer solution. This spectral response agrees well with the published results [87] and was the same for all the TiO_2 samples, although there were variations in the magnitude of the photocurrent from sample to sample. Also, as shown in Fig. 3.10, the bandgap photocurrent follows the established pattern of the photocurrent-potential behavior [31]. The figure shows only three samples, but this general behavior was true for all the samples we investigated. As anticipated, the exact photocurrent-potential behavior, magnitude of the photocurrent and the shape of the curve, varies from sample to sample owing to the influence of the doping density and the surface conditions of the samples.

3.3.2 SBG Photocurrent

The spectral response obtained in the SBG energy range is shown in Fig. 3.11. This spectrum shows a major optical transition at wavelength 550 nm, which corresponds to the energy 2.2 eV. As shown in Fig. 3.12, the SBG photocurrent-potential behavior is completely different from the bandgap photocurrent, showing a maximum around -0.35 V vs SCE. This anomalous SBG photocurrent-potential behavior is unique and common to all the TiO_2 samples in the study.At this point it became necessary to established that the SBG photoresponse

was not caused by the scattered bandgap radiation from the monochromator and that the photocurrent was indeed real. We repeated SBG-induced photocurrent measurements using an Argon laser with appropriate interference filters. For all the wavelengths available in the laser light, the SBG photocurrent-potential behavior was the same as in Fig. 3.12. Also, as shown in Fig. 3.13, within the limitations of both techniques, the SBG photocurrent spectra agreed with each other, indicating a major contribution from a transition at 550 nm =2.2 ev. The quantum effiency for SBG photoresponce at 500 nm was measured as $6x10^{-7}$, and with such a low effiency it was impossible to make direct d.c. measurements. However, this was essential to decide whether the current was Faradaic or a transient photocapacitive effect. Since the phase-sensitive detection technique with lock-in amplifier that we employed for measuring the photocurrent does not give any information on the real shape of the signal input, we were forced to use a wave-form eductor (PAR Model TDH-9), which measures all the main Fourrier components of the signal and analyses them to give the input signal wave form. Fig. 3.14 shows the comparisons of the SBG photocurrent signal and the chopped light input signal. The photocurrent signal closely follows the incident illumination, and hence the SBG signal was found to be a result of a Faradaic current. It was thus concluded that the observed SBG photo-signal was caused by an optical excitation of carriers in the energy range less than the bandgap energy of TiO_2.

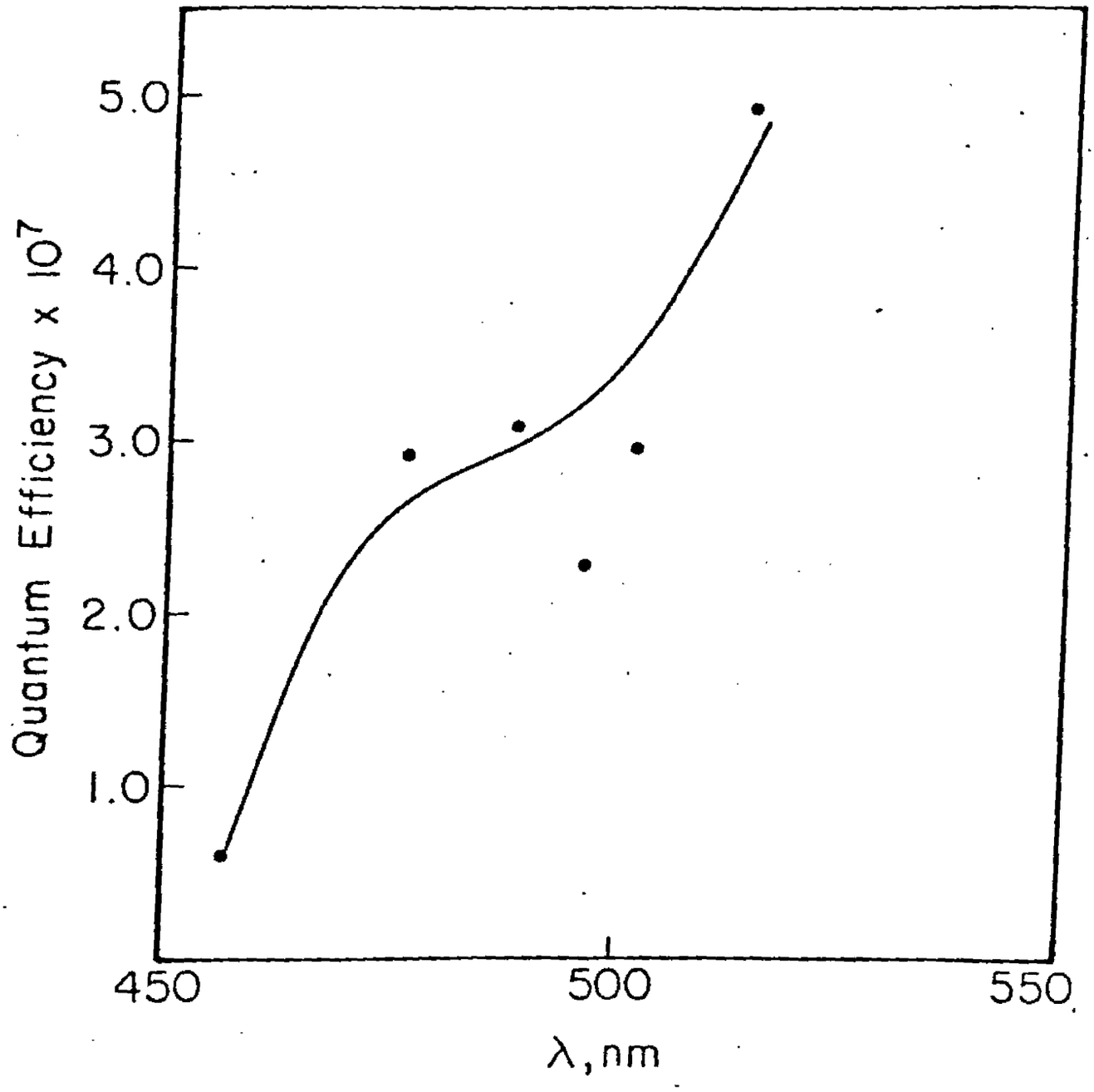

Fig. 3.13 SBG spectral response obtained with laser light.
U= -0.35 (V vs SCE).

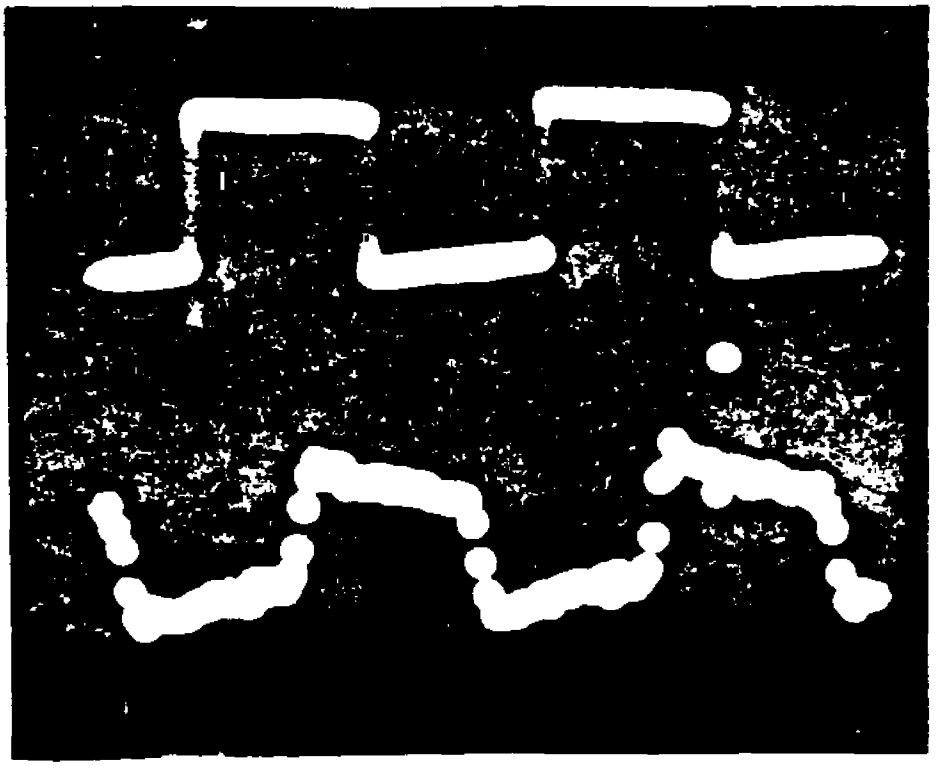

Fig. 3.14 SBG photocurrent (bottom) as measured by the wave form eductor and chopped light input signal (top) at the chopping frequency 26 Hz.

Fig 3.15 shows the sensitivity of the SBG photocurrent signal to the ambient condition, namely, oxygen in the electrolyte, indicating that oxygen quenches it. Fig. 3.16 shows that the SBG photocurrent is linear with the intensity at the power levels being used.

3.3.3 Background Illumination Effects on Bandgap Photocurrent

We have extended the study of photocurrent-potential behavior in order to achieve a better understanding of the surface recombination of photogenerated carriers. We used the two-beams experimental method, where the second beam creats additional photocarriers at the interface while the photocurrent is measured.

A typical photocurrent-potential behavior for n-TiO_2 in a phosphate buffer, as a function of background illumination, is shown in Fig. 3.17. The sample we have used to study the background illumination effect was the one that gave a comparatively simple potential behavior for C_{ss} (Fig. 3.3c). The scanning beam was held at 350 nm while the electrode potential was scanned at 2 mV/sec. Pronounced effects of background illumination were observed in the descending region of the photocurrent-potential curve, namely, at forward bias. This was true up to the highest intensity of background illumination that was measured here (16 mW/cm^2). More detailed measurements of this region are shown in Fig. 3.18. Special care was taken to eliminate the possibility

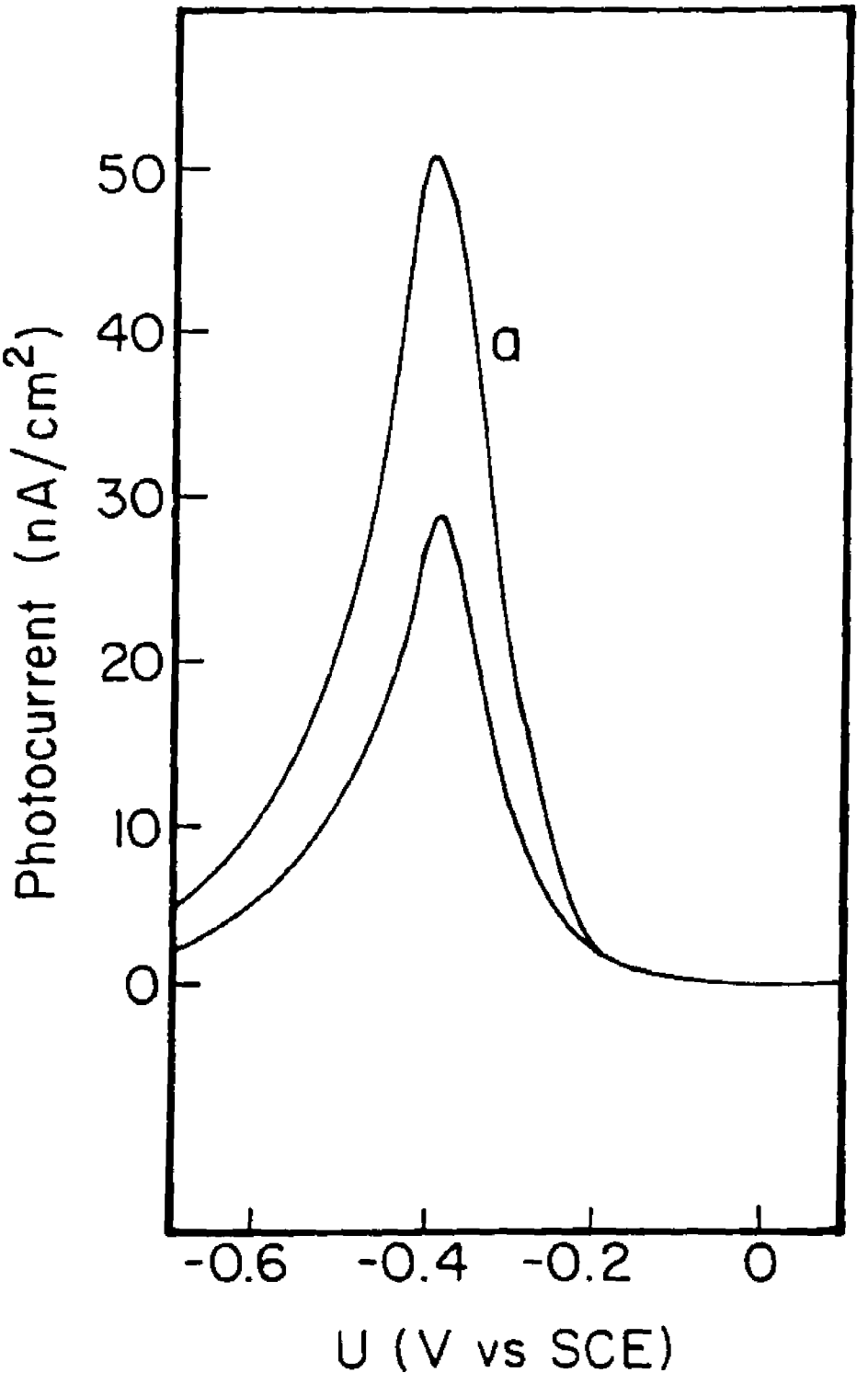

Fig. 3.15 The effect of O_2 on the SBG photocurrent.
(a) After passing N_2 for 15 min.
(b) After passing O_2 for 15 min.

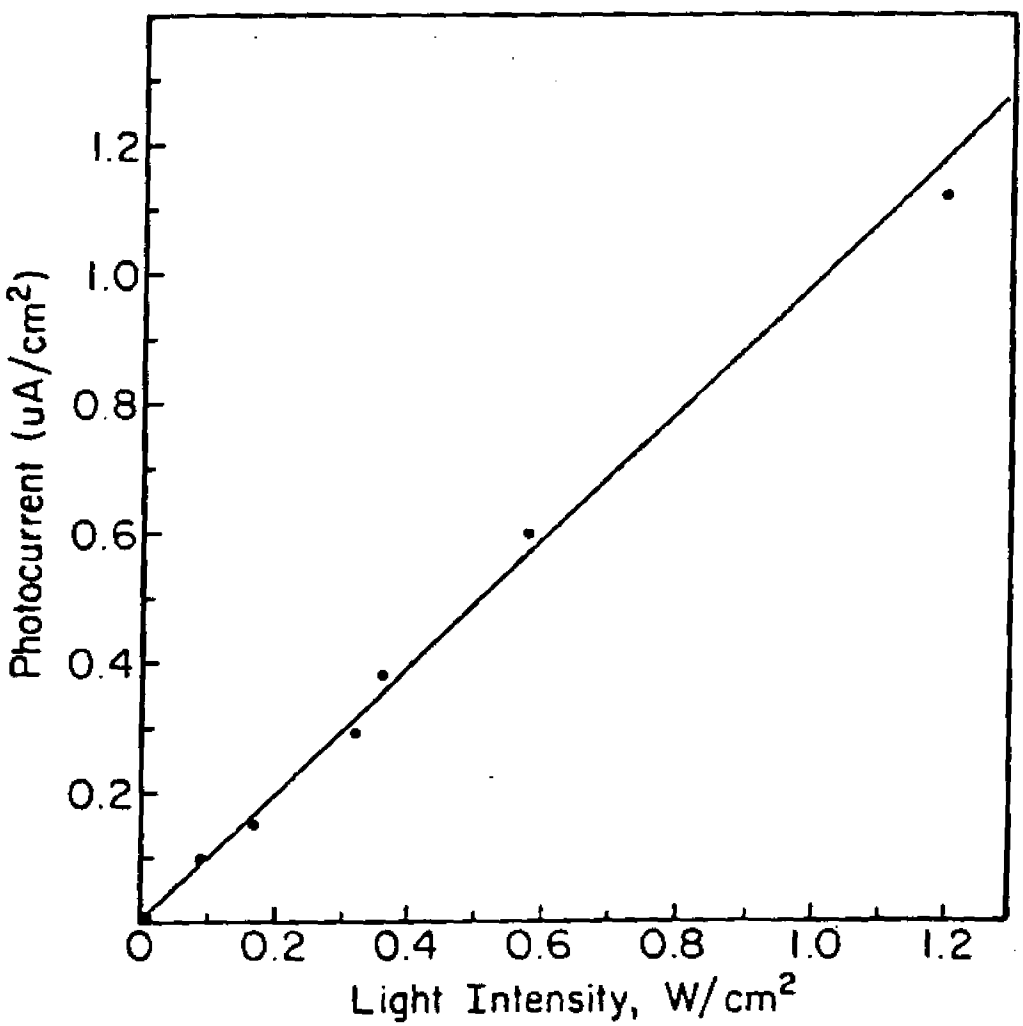

Fig. 3.16 SBG photocurrent variation with light intensity.

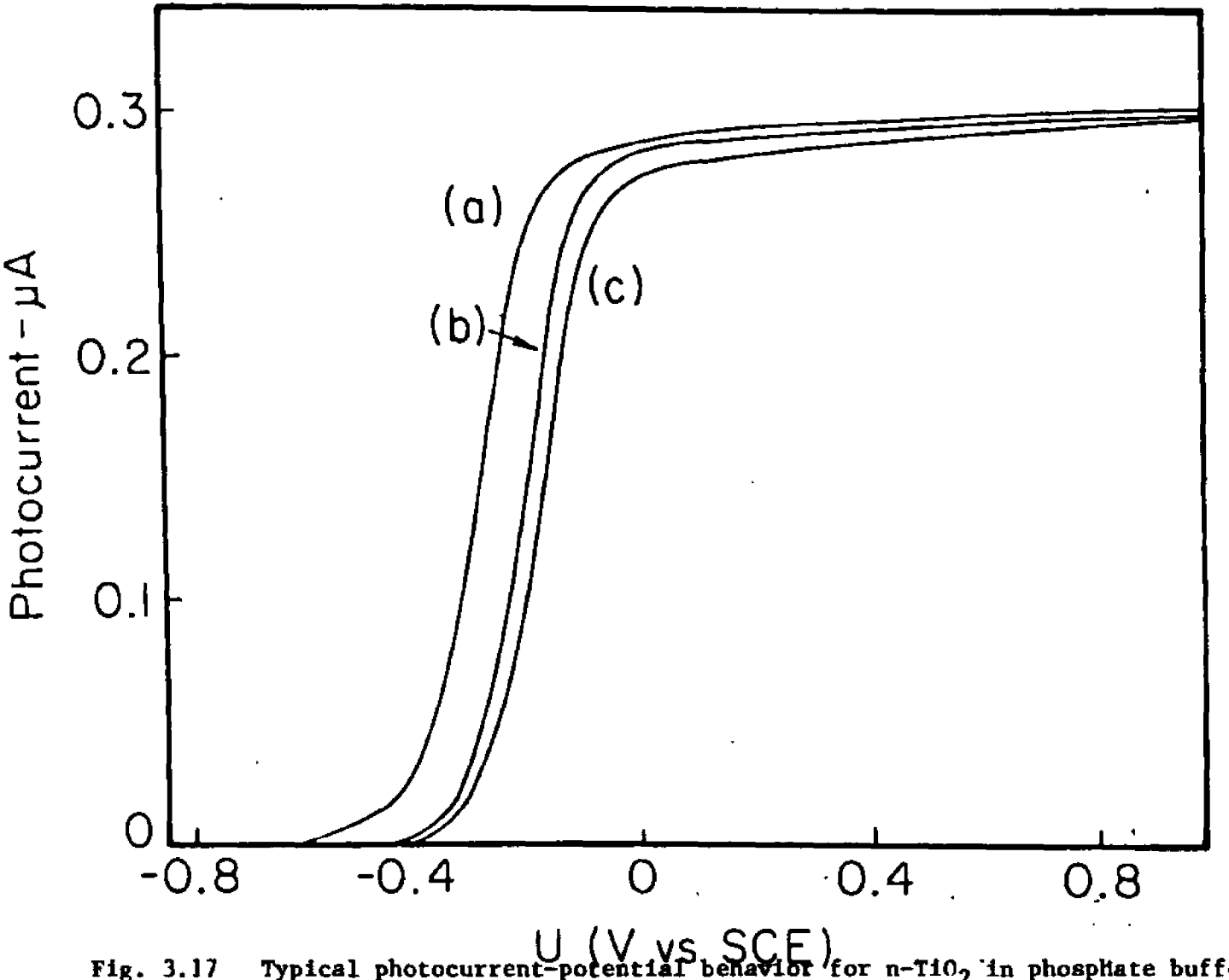

Fig. 3.17 Typical photocurrent-potential behavior for n-TiO_2 in phosphate buffer as a function of background illumination. (a) without background illumination. (b),(c) with background illumination of intensity 2.1 and 5.0 mW/cm^2,respectively.

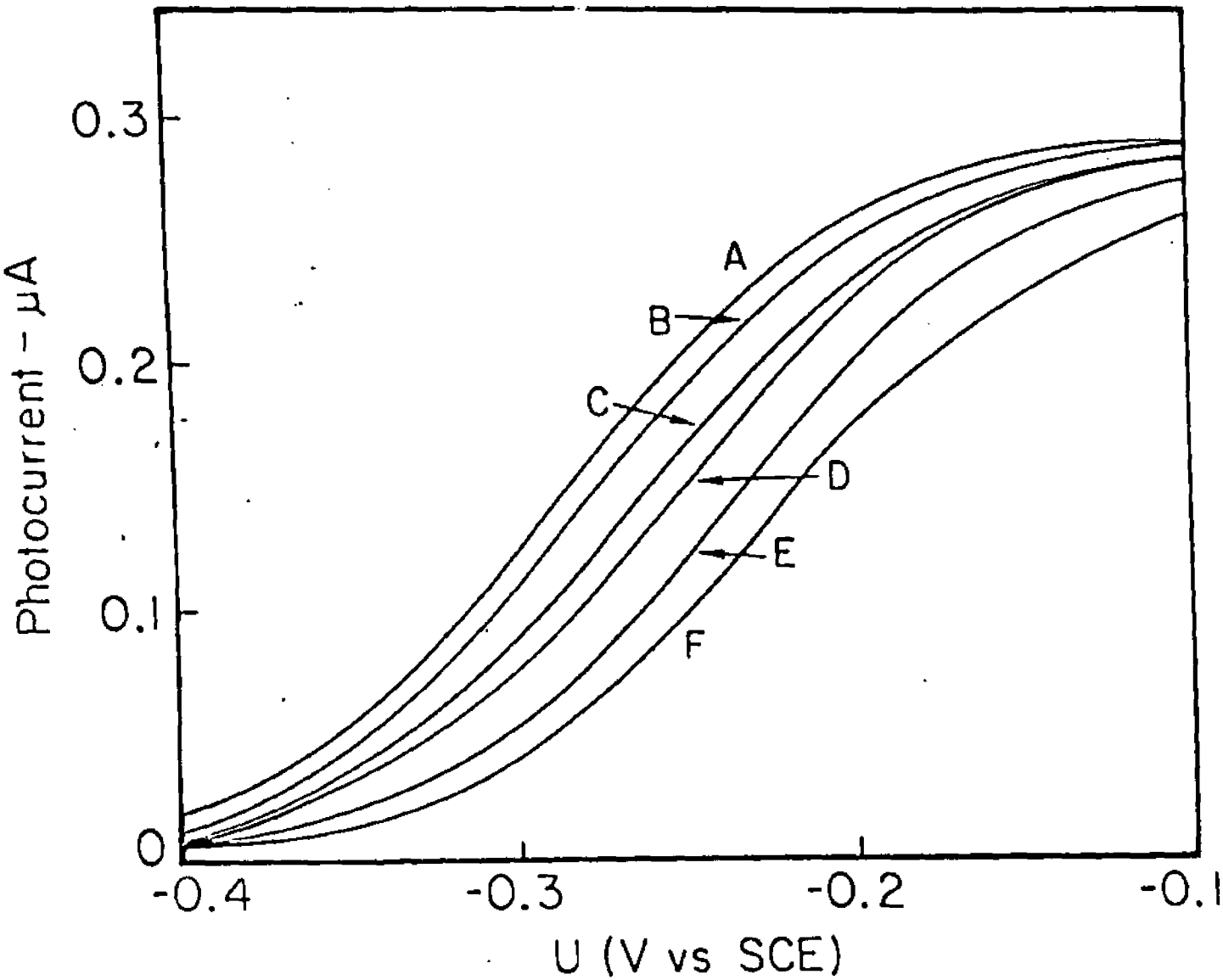

Fig. 3.18 Detailed measurements of background illumination effect in the potential region where it is prounced. (A) without background illumination, (B)-(F) with background illumination of intentsity 0.1, 1.3, 8.1 and 16.2 mW/cm^2, respectively.

that the effects which were observed in Figures 3.17 and 3.18 are due to a potential shift, caused by IR drop due to the d.c. photocurrent which is being induced by the background illumination. It was observed that the IR electronic compensation was practically not required for the electrochemical cell that we used here. Data were taken by placing the reference electrode close to the working electrode by using a Luggin capillary. There was no change observed. The decrease in photocurrent, at the electrode potential of -0.30 V vs SCE, due to the background illumination, was measured as function of the distance between the working electrode and the reference electrode. The decrease in photocurrent was independent of the position of the reference electrode.All these measurements have shown conclusively that the effect of background illumination can not be traced to to a potential shift caused by an IR drop.

Fig. 3.19 shows the spectral response as a function of background illumination. These curves are corrected for the spectral intensity distribution at the monochromator output. The shape of the spectral response curves do not change with background illumination, but the efficiency decreases sharply with the increased intensity of the background illumination. Harris and Wilson [87] have reported previously that under intense background illumination the spectral response is changed due to an aging effect. We repeated the spectral response measurements with and without background illumina-

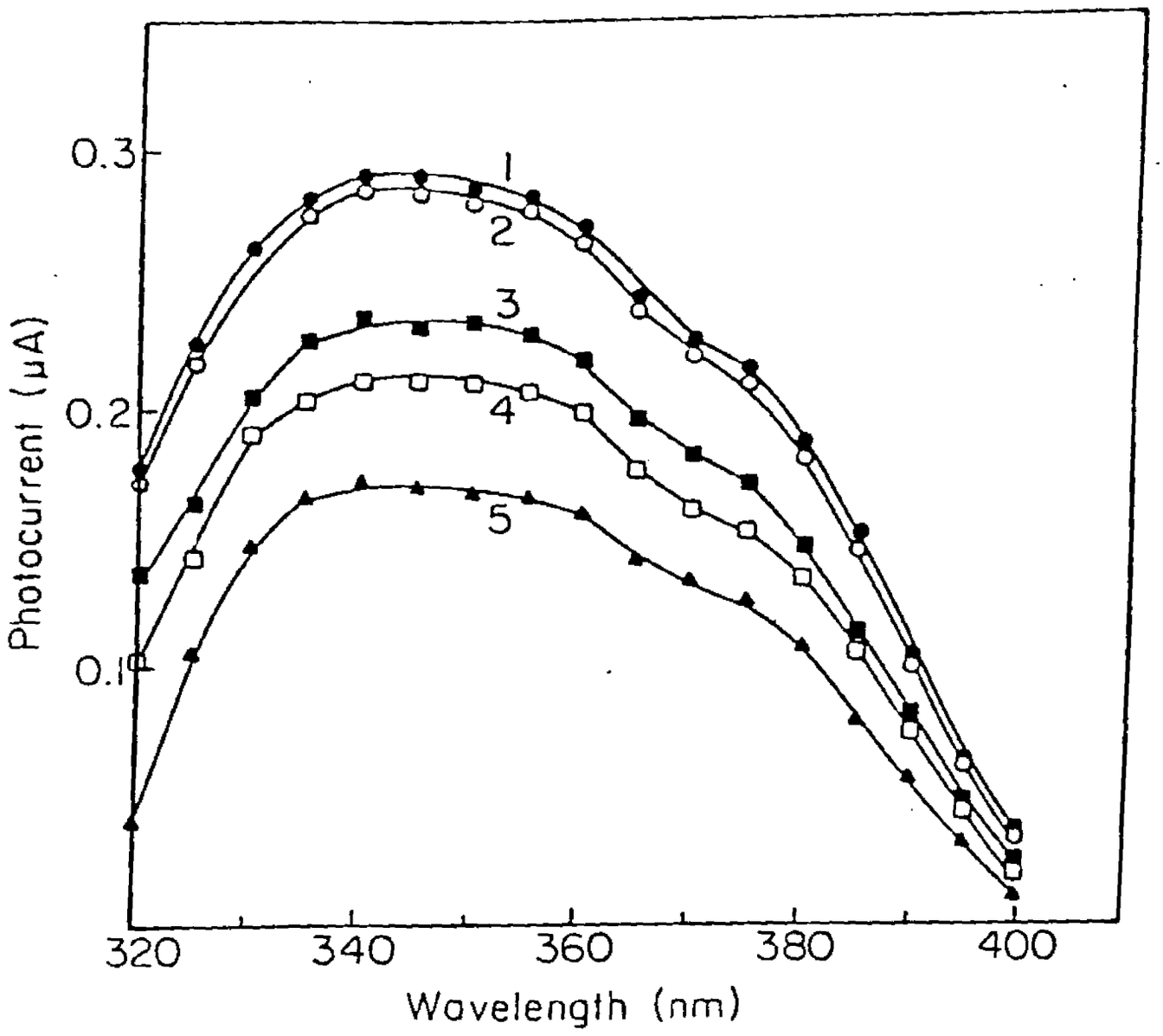

Fig. 3.19 Spectral response for n-TiO_2 as a function of background illumination. Curve 1 without background illumination. Curves 2-5 with background illumination of intensity 0.1, 2.1, 3.9, and 16.2 mW/cm^2, respectively.

tion and could not observe any significant difference. This eliminates the possibility that the observed decline of the photoresponse was due to an aging efect.

3.4 EER MEASUREMENTS ON $CdIn_2Se_4$ ELECTRODES IN AQUEOUS-POLYSULFIDE

We have chosen the single crystal $CdIn_2Se_4$/ polysulfide system for the detailed study of Fermi level pinning at the semiconductor/electrolyte interface, because (a)compared of TiO_2, this system provides a wide range of potentials in which the Fermi level pinning can be observed using EER, and (b) it is sensitive to the surface preperation conditions. Measurements were taken before and after photoetching the sample surface. Fig. 3.20 shows the EER spectra at a d.c. bias of -0.2 V vs Pt. before and after the photoetching. Fig. 3.21 shows the variations of the intensity of the EER signals as a function of the electrode potential. In both cases, before and after photoetching, the signal decreases dramatically as we move toward reverse bias.

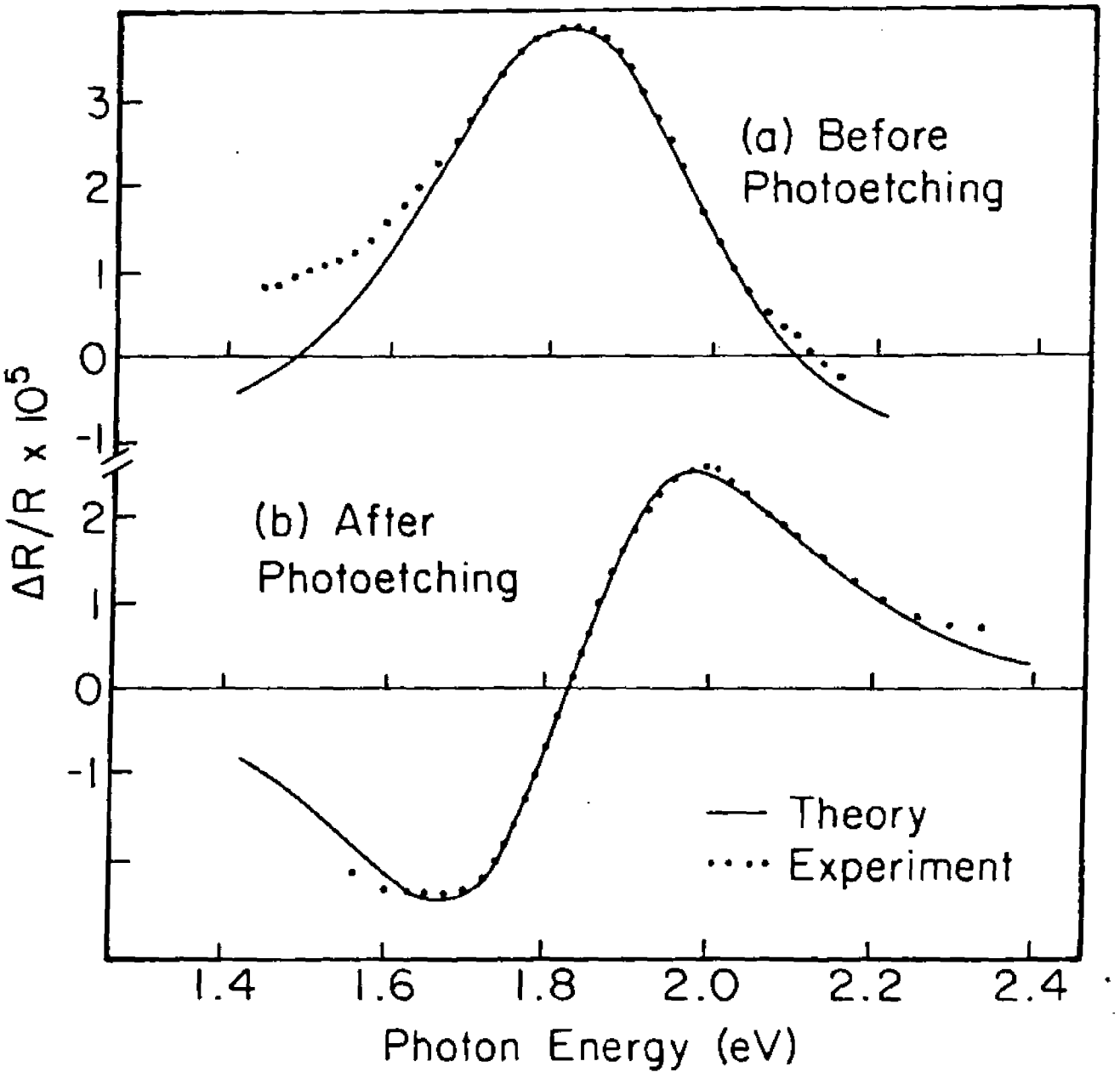

Fig. 3.20 EER spectra for $CdIn_2Se_4$ in aqueous polysulfide, at a d.c. bias of -0.2 V vs Pt.
(a) Before photoetching (b) After photoetching

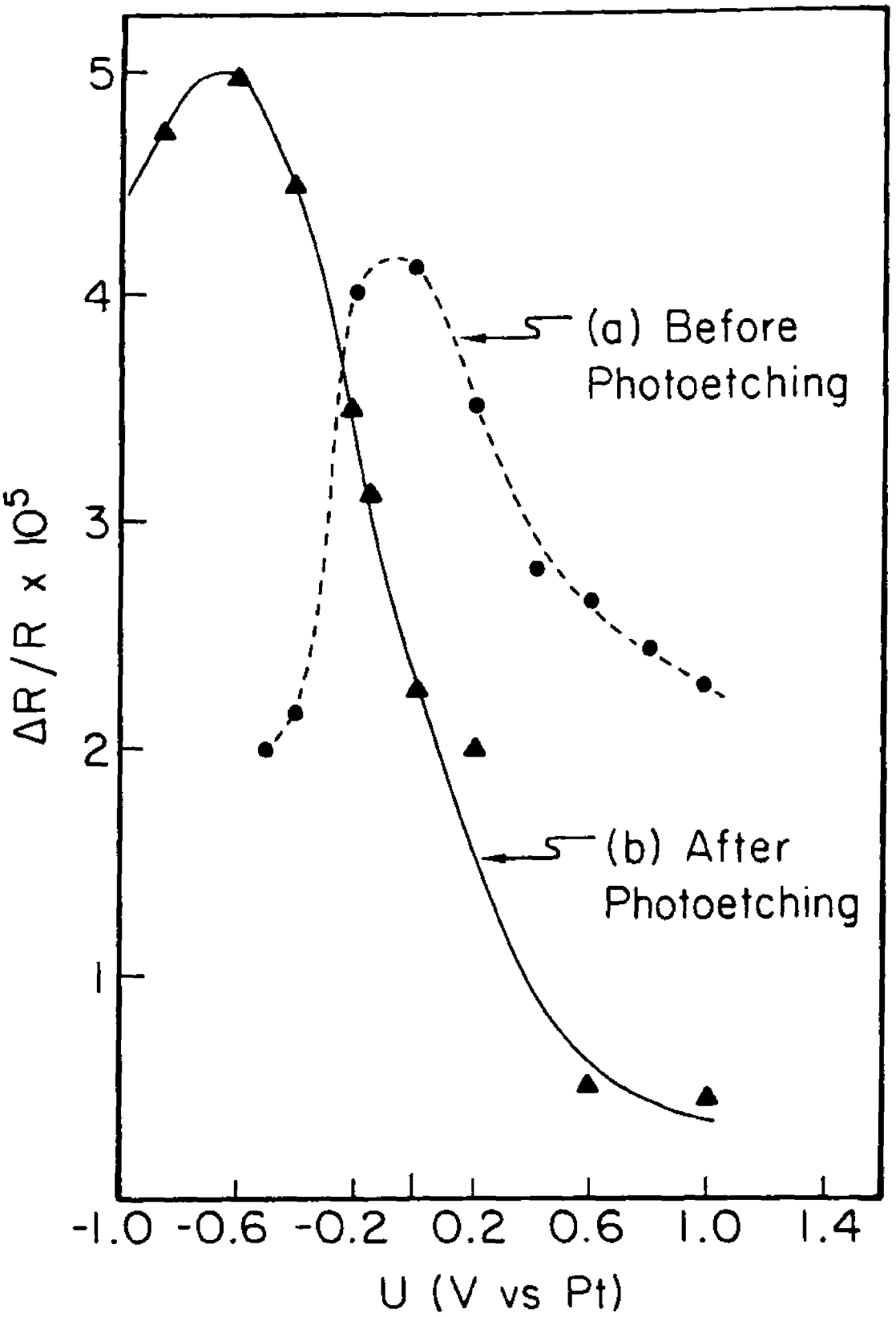

Fig. 3.21 Variation of the EER signal with potential for $CdIn_2Se_4$ in aqueous polysulfide.
(a) Before photoetching (photon energy=1.8 eV).
(b) After photoetching (photon energy=2.0 eV).

Chapter IV

DISCUSSION AND CONCLUSION

4.1 n-TiO_2 /AQUEOUS-ELECTROLYTE INTERFACE

4.1.1 Foreign Ions Adsorption and Potential Distribution at the n-TiO_2 /Aqueous-Electrolyte Interface

The results shown in Figures 3.2 and 3.5 demonstrate the interdependancy between the elelctrolyte species that can adsorb on the surface of the semiconductor electrode and the potential distribution at the semiconductor/electrolyte interface. It is clear that the presence of I^- ions in the electrolyte causes the flatband potential to be shifted by 0.2 V in the cathodic direction, or in other words, the total negative charge on the TiO_2 electrode surface increases in the presence of I^- ions compared with F^- ions in the electrolyte.The reason for this behavior can be understood by examining the different possible adsorption processes that compete with each other in determining the total charge on the electrode surface. The results shown in Fig. 3.3, involving n-TiO_2 electrodes in phosphate buffer (pH=6.6), also confirms this behavior where the flatband potential is about -0.8 V vs SCE. In the case of an oxide semiconductor and an aqueous electrolyte interface, the adsorption of water molecules on the electrode surface is inevitable. On the other

hand, adsorption of OH groups on the semiconductor surface is responsible for the pH dependence of the flatband potential (section 1.2.3). However, in the result shown in Fig. 3.2, above reasons may not be the case, because the ionic strength of both the electrolytes is the same. The negative shift in the flatband potential in KI compared with KF suggests that the total negative charge on the electrode surface increases by the adsorption of I^- ions. The shift in flatband potential due to I^- has been already reported [25]. The surface concentration of I^- causing this shift can be calculated using the relation:

$$\delta U_{fb} = \delta V_H = eN_t/C_H \qquad (4.1)$$

which was obtained from Equation 1.16, where N_t is the surface concentration of adsorbed I^- ions. If we take the value of the Helmholtz layer capacitance to be 40 $\mu F/cm^2$, then N_t is 5 $x10^{13}/cm^2$ or approximately 5% of a monolayer.

The reason for the adsorption of I^- than F^- ions can easily be understood by examining the differences in the hydration energy of these ions in aqueous electrolytes. In an aqueous electrolyte each ion is surrounded by the polar H_2O molecules and hence form a solvation sphere. The solvation energy of ionic species are different from one another, e.g.,for F^- it is larger than for I^-. Thus F^- stays outside the inner Helmholtz layer, while the I^- is enable to

penetrate into the inner Helmholtz layer and adsorb on the surface of TiO_2 [91]. Alterantively, if the strength of the metal-halogen bond is the determining factor, then we can expect the order of adsorption to be reversed.Yates et al. [92] claimed it to be the case with TiO_2 powder. However, our experimental result, namely, a cathodic shift in the flatband potential in the presence of I^-, suggests that different solvation energies are the more likely cause. As shown in Fig. 3.2, in addition to the shift in the flatband potential, a nonlinear Mott-Schottky behavior is evident in KI. This behavior could not be the result of a nonuniform doping or the presence of deep doping levels in the sample, because the same sample in KF shows the linear behavior throughout the potential range. The alternative explanation appears to be the existence of mid-gap surface states that can be charged by the applied bias voltage. This bias dependent surface charge determines the instantaneous flatband potential at the interface and hence leads to a nonlinear Mott-Schottky plot. A similar result has been reported by Tomkiewicz [24] on TiO_2 electrodes, but under different surface preparation conditions. This Fermi level pinning effect will be discussed in more detail in the latter part of this chapter. In the following section we will explore the surface states that emerge in the results of various measuremetnts given in chapter 3.

4.1.2 Surface States at the n-TiO_2/Aqueous-Electrolyte Interface

The general surface state distribution at the n-TiO_2/aqueous-electrolyte interface is evident from the impedance measurements shown in Figures 3.2 and 3.3. The dominant state is the one that tails from the conduction band and it is present in all samples and in all the electrolytes used. The high density of surface states might be able to communicate efficiently with the conduction band electrons and hence participate actively in the surface recombination of photogenerated carriers. This particular aspect, as well as the possible origin of this surface state, will be discussed in more detail in the forth coming sections. In addition to the tailing surface state band, two other distinct surface states, one at 0.8 eV and other at 1.3 eV below the conduction band of TiO_2, are present at the interface. In the latter part of this chapter we will show the correlation between the surface state at 0.8 eV and the SBG photocurrent. The other surface state, appearing at 1.3 eV below the conduction band, is shown to be correlated to the SBG EER structure shown in Figures 3.6 and 3.7.

4.1.3 "Intrinsic" Surface State at the TiO_2/Aqueous-Electrolyte Interface

The combined results of the measurements shown in Figures 3.2 and 3.3 and the SBG EER measurements shown in Figures 3.6 and 3.7 are in excellent agreement in regard to the location of the surface state at 1.3 eV. The SBG EER peak at

1.3 eV must result from the optical transition between the filled surface states and the conduction band. Since in situ measurements of the type being described here do not provide unique information about the spatial location of the states involved, we are left with the alterantive definition of surface state as states that have energies within the forbidden gap and are sensitive to the interaction with the ambient material. The peak amplitude of the SBG EER spectra are strongly dependent on the species in the electrolyte, but the peak position is not. The dependence of the peak amplitude on the electrolyte is the same as the expected tendancy of adsorption of the halogen ions at the electrode surface, as discussed previously. Since the peak position is independent of the nature of the adsorbate, the associated surface states must be "intrinsic" to the semiconductor. In other words these surface states do not originated from the orbital interactions between the surface and the adsorbate atoms.

The potential behavior of SBG EER in Fig. 3.8 shows that the EER signal becomes stronger in the potential region where the junction is in a weak accumulation mode, i.e.,when it is closer to the flatband condition. This is not surprising in view of the enhanced surface effects resulting from the localization of applied a.c. potential at the surface.As we approach flatband conditions, the differential capacitance of the space charge layer increases untill it

becomes the same order of magnitude as the one caused by the Helmholtz layer. In relatively heavily doped semiconductors, such as those under investigation, the capacitance under flatband conditions is completely dominated by the Helmholtz region. Thus, the electric field induced perturbation, under the above mentioned condition, is localized at the surface. This could be the main reason that the SBG EER can be detected only in a weak accumulation mode. In all cases shown in Fig. 3.8 the peak potential follows the flatband potential whether the latter varies because of change in pH or because of adsorption.

Now we have to investigate the possible reasoning for the observed "intrinsic" nature of the surface states. If these surface states were created by orbital interactions between the semiconductor surface and the adsorbates, one would expect the peak position, both in EER and in surface state capacitance, to be strongly dependent on the adsorbates. But it was not the case here. On the other hand, we can not exclude the possibility that these surface states actually originated in the presence of the adsorbates, because without them they could not be detected.

When the surface is fully solvated,and the Helmholtz layer is free of adsorbed species, the intrinsic surface states interact with solvent to shift their energy toward the band edges (section 1.4.2b) and become undetectable. On the other hand, with the adsorbed species, substituting for solvent, the states resume their intrinsic energy provided that ad-

sorption is purely electrostatic with negligible orbital interactions between the surface states and the adsorbates. In this case the energy will be independent on the nature of the adsorbate but the number of available states will depend on the number of solvent molecules that were displaced. As discuussed earlier, this number also depends on the adsorbates, because due to the different hydration energy. Thus, this "intrinsic" surface state concentration is dependent on the nature of the adsorbate. Alternatively, if the adsorbed ions form a chemical bond with the surface that is stronger than the solvation energy, then the enrergy of the bonded state shifts further into the bands, and we would not be able to detect the surface states.

The surface state at 1.3 eV below the conduction band of TiO_2 that we observed here is in excellent agreement with the previously reported results on TiO_2 with different experimental techniques. Frank and Bard [42] reported the existance of surface states at about 1.2 eV below the conduction band of TiO_2 using electrochemical measurements. Morisaki et al. [61] found the same state with SBG photocurrent measurements. Tomkiewicz [24] also found evidences of it with impedance measurements on the TiO_2/aqueous-electrolyte interface. Apart from these measurements all involving a TiO_2/electrolyte ineterface, Henrich and Kurtz [93] observed a surface state at 1.3 eV below the conduction band of a vacuum-fractured (001) surface of

TiO_2 using ultraviolet photoemission measurements (UPS), a result that agrees well with our result not only in regard to the location of the surface state in the bandgap, but also to the predicted "intrinsic" nature of it.

4.1.3 (a)The Atomic Nature of the Surface States at the TiO_2 surface

It is now clear from the previous discussion how necessary it is to examine the real atomic nature of the TiO_2 surface in contact with an aqueous electrolyte.We will first concentrate only on the bare TiO_2 surface. As shown in Fig. 4.1, in rutile structure each Ti atom is coordinated to six O atoms and each O atom is coordinated to three Ti atoms, whereas on TiO_2 (001) surface each Ti atom is fourfold oxygen-coordinated.Kasowski and Tait [94] treated the (001) surface of TiO_2 theoretically, showing that a large number of empty surface states should exists in the upper half of the bulk bandgap because the surface Ti atoms are only fourfold oxygen-coordinated compared to the bulk sixfold oxygen-coordination. However, attempts to fill those states by doping or reducing the crystal push the surface state up into the bulk bandgap [95].

Also, it is common for semiconductor surfaces to reconstruct and/or relax the surface atoms in order to incearse the local coordination and eliminate the bandgap states [96]. Kasowski and Tait [94] mentioned that although the (001) surface of TiO_2 is unstable owing to the presence of

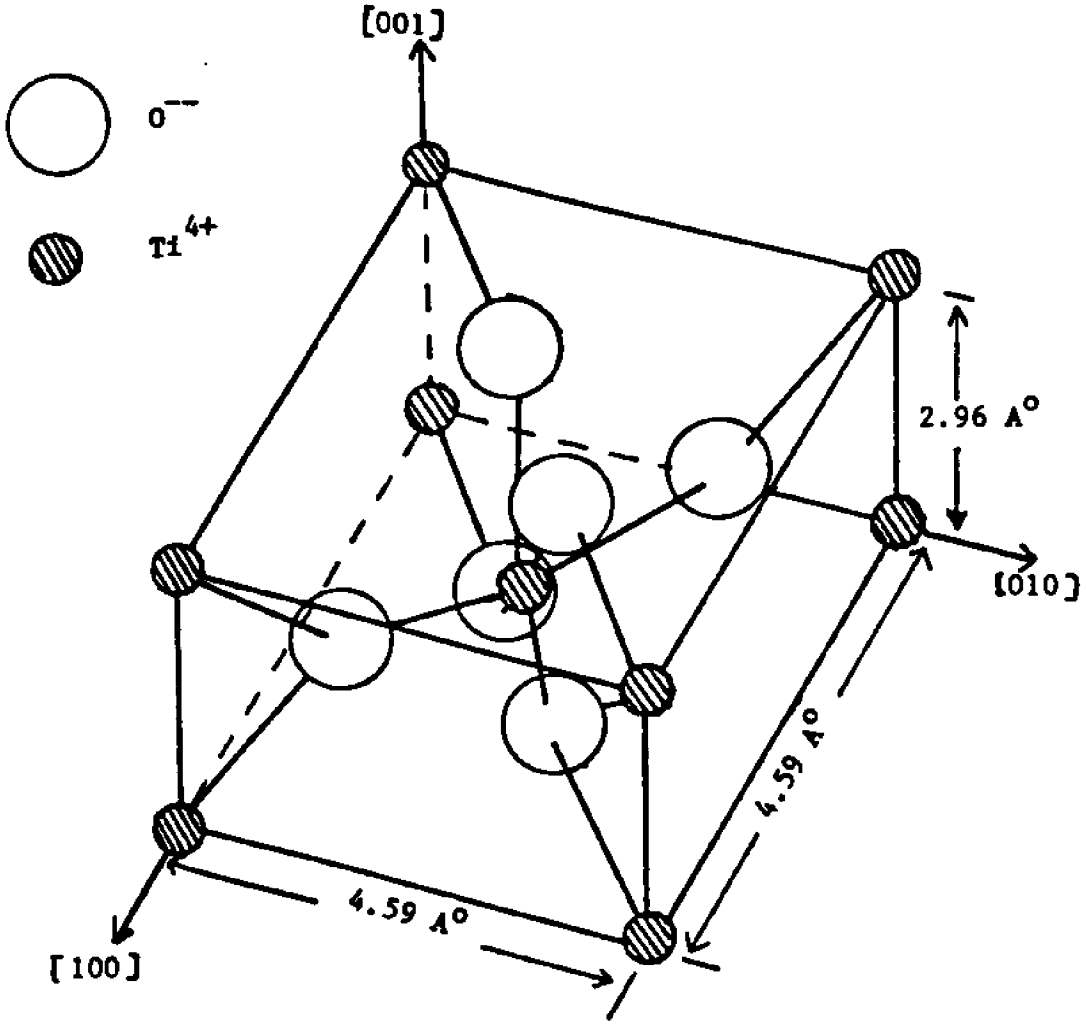

Fig. 4.1(a) Rutile structure of TiO_2.

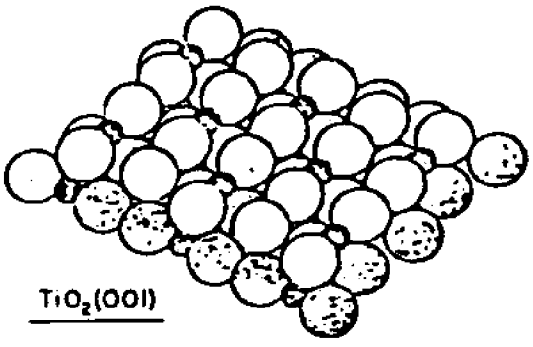

Fig. 4.1(b) Model of the (001) surface of TiO_2.

quite a large surface state band, still they can not be removed completely by a simple relaxation of surface atoms. However, low-energy electron diffraction (LEED) measurements on polished faces of TiO_2 shown [97,98] that these surfaces are extreamely unstable on annealing. Nevertheless, Henrich et al. [99] found no evidence of reconstruction or faceting of reduced TiO_2 sample surfaces by vacuume fracturing.

Henrich and Kurtz [93] assinged the UPS peak at 1.9 eV above the valence band of vacuum-fractured (001) surface of TiO_2 (Fig. 4.2) to a defect surface state created by the O vacancy at the surface. They suggest the origin of this bandgap surface state is the incomplete screening of pairs of surface cations at defect sites. In view of the "intrinsic" surface state observed here for the reduced (001) surface of TiO_2 in contact with an aqueous electrolyte, the defect surface state argument agrees very well. The unsolvated surface without orbital interactions with the adsorbed ions closely resembles the bare surface and hence this surface can be expected to bring back defect surface states into the bandgap at the TiO_2/electrolyte interface. Removal of surface states by solvation was predicted by Kowalski et al. [50] on theoretical cosiderations and experimentally verified by Kurtz and Henrich [100] by UPS measuremtns. Indeed, our experimental observations on SBG EER and impedance measurements support this behavior and clearly show that the TiO_2 (001) surface is unsolvated in KI than in KF.

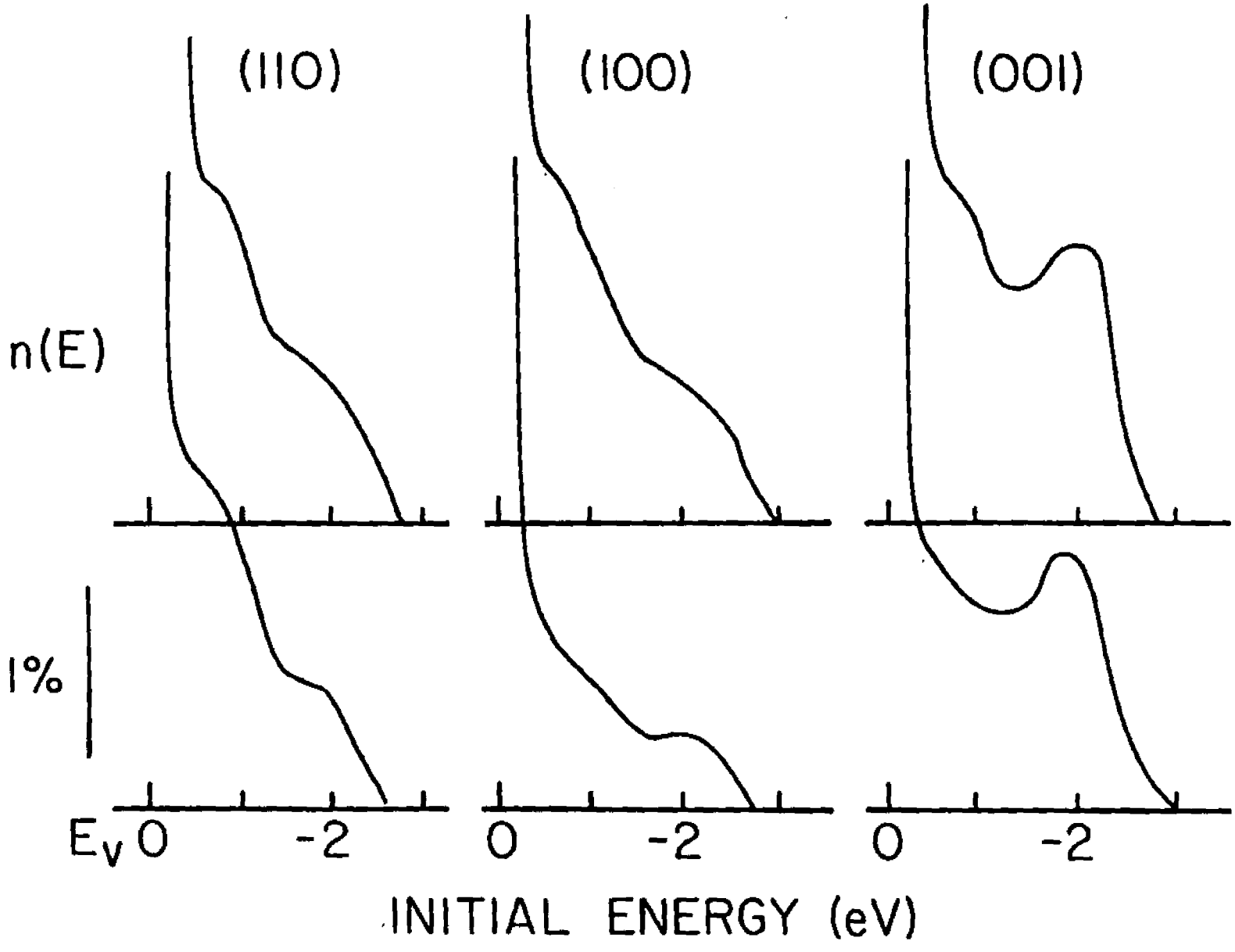

Fig. 4.2 UPS spectra for three different surfaces of TiO_2. (Ref. 93).

The location of this "intrinsic" surface state in the bandgap of TiO_2 is an ideal situation for the photoelectrolysis process, because this state overlaps with the O_2/H_2O couple in the electrolyte. Overlapping provides an intermediate electronic energy state for transferring the photogenerated holes from the valence band to the reduced states in the electrolyte. In the folowing section we will evaluate the concentration of "intrinsic" surface states.

4.1.3 (b) Concentration of "intrinsic" Surface States

We can use the potential variation of the surface state capacitance in Fig. 3.2 to estimate the "intrinsic" surface state concentration induced by the adsorption of I^- ions on the TiO_2 surface. The surface state capacitance owing to the "intrinsic" states is readily obtainable by substracting the tailing part of the two curves in Fig. 3.2. The applicability of the Gausssian energy distribution for the surface states present at the semiconductor/electrolyte interface was reported by Tomkiewicz [52]. In the following we will adapt this distribution to obtain the surface states concentration resulting from the adsorption of I^- ions.

A gaussian energy distribution of surface states is given by [52]

$$N_{ss}(E) = \frac{N_t}{\sigma e\ (2\pi)^{1/2}} \quad \exp\left[\frac{-(E_t-E)^2}{2(\sigma e)^2}\right] \qquad (4.2)$$

where σ_e is the standard deviation in energy, E_t is the energy at the maximum density, and N_t is the total surface state concentration. The number of ionized states is given by:

$$N_{ss}^{+}(E) = \int_{E_v}^{E_c} \frac{N_{ss}(E)\, dE}{1 + e^{(E_F-E)/kT}} \qquad (4.3)$$

for $\sigma_e >> kT$:

$$\frac{1}{1 + e^{(E_F-E)/kT}} = \Gamma(E_F-E) \qquad (4.4)$$

where $\Gamma(E_F-E)$ is the unit step function defined as

$$\Gamma(E_F-E) = \begin{cases} 1 & \text{for } E > E_F \\ 1/2 & \text{for } E = E_F \\ 0 & \text{for } E < E_F \end{cases} \qquad (4.5)$$

Inserting Equations 4.5 and 4.2 into Equation 4.3 will result in [24]:

$$N_{ss}^{+}(E_F) = \frac{N_t}{2}\left[\text{erf}\ \frac{(E_t-E_F)}{\sigma\sqrt{2}} - \text{erf}\ \frac{(E_t-E_c)}{\sigma\sqrt{2}}\right] \quad (4.6)$$

where $\text{erf}(x) = \frac{2}{\sqrt{\pi}}\int_0^x e^{-x^2}\,dx$.

Neglecting the energy difference between the Fermi level and the bottom of the conduction band in the bulk of the semiconductor, we can relate the energy (E) to electrode potential (U) as follows:

$$E_F = -eU$$
$$E_t = -eU_t$$

and (4.7)

$$E_c = -eU_{fb}$$

(For simplicity, Fermi level pinning has been omitted from this analysis, but will be discussed in the latter part of this chapter.) From Equation 1.14, the potential drop across the space charge layer is given by:

$$V_B = U - U_{fb} = \Delta\Phi_s \quad (4.8)$$

Thus,

$$N_{ss}^{+}(U) = \frac{N_t}{2}\left[\text{erf}\ \frac{e(U_{fb}+\Delta\varphi_s-U_t)}{\sqrt{2}\,\sigma} - \text{erf}\ \frac{e(U_{fb}-U_t)}{\sqrt{2}\,\sigma}\right] \qquad (4.9)$$

The differential surface state capacitance is therefore given by [24]

$$C_{ss}(U) = \frac{dN_{ss}^{+}}{d(\Delta\varphi_s)} = \frac{eN_t}{\sigma\sqrt{2}}\ \exp\left[-\frac{(U-U_t)^2}{2\sigma^2}\right] \qquad (4.10)$$

Using Equation 4.10, we found the "intrinsic" surface state concentration to be $5\times10^{12}/cm^2$ for the surface state capacitance shown in Fig 3.2 owing to the I^- adsorption. According to Henrich and Kurtz the "defect" surface states at the TiO_2 originate from the O vacancies created on the sample surface during the reduction of the electrode. For the sample with a doping density $N_D \sim 10^{19}/cm^3$, the surface concenrtation of O vacancies is $(N_D)^{2/3} \sim 10^{13}/cm^2$, a value that agrees with the one obtained for the "intrinsic" surface state concentration obtained above from the impedence measurements in KI.

4.1.4 Influence of Surface States on the Photoresponse at the n-TiO_2 /Aqueous-Electrolyte Interface

The current-potential behavior of the band-to-band photoresponse shown in the Figure 3.10 and the spectral response shown in Figure 3.9 give an indication of surface recombination of the photogenerated carriers at the TiO_2/electrolyte interface. Photocurrent-potential behavior shows that even at a band bending of 400 mV, the photocurrent onset is about 400mV anodic to the flat band potential, suggesting that a high density of surface states present at the interface and that these states quench the photocurrent at lower band bendings. Also, the low photoresponse in the high -energy portion of the spectral response suggests that the photocarriers generated at the surface of the electrode, where high-energy photons are absorbed closer to the surface because of the high absorption cofficient, are recombined much faster owing to the presence of surface states. In the following sections we will attempt to evaluate this surface recombination effect in more detail, using normal photocurrent-potential behavior and the background illumination effect on photoresponse.

4.1.4 (a)Photocurrent-Potential Response with no Background Illumination

The surface recombination rate given in Equation 1.32 is expressed in terms of the total number of occupied states (n_t). Assuming a gaussian density of surface states (Equation 4.2) we can write n_t as

$$n_t = \frac{N_t}{e\sigma\sqrt{2\pi}} \int_{E_v}^{E_c} \frac{e^{-(E_t-E)^2/2(\sigma e)^2}}{1 + e^{(E-E_F)/kT}} \, dE \qquad (4.11)$$

Following a similar procedure to the one that led to Equation 4.6, we can show [24]

$$n_t = \frac{N_t}{2} \left[\text{erf} \frac{(E_t-E_v)}{\sigma e\sqrt{2}} - \text{erf} \frac{(E_t-E_F)}{\sigma e\sqrt{2}} \right] \qquad (4.12)$$

By inserting Equation 4.12 into Equation 1.32, the surface recombination rate S_r can be written as [64]

$$S_r = \frac{1}{2} k_r^h N_t \left[\text{erf} \frac{(E_t-E_v)}{\sigma e\sqrt{2}} - \text{erf} \frac{(E_t-E_F)}{\sigma e\sqrt{2}} \right] \qquad (4.13)$$

where $k_r^h = \sigma_r v_{th}$. For surface states close to the bottom of the conduction band [64],

$$(E_t-E_v)/e\sigma >> 1$$

and

$$S_r = \frac{1}{2} k_r^h N_t \left[1 - \text{erf} \frac{(U-U_t)}{\sigma\sqrt{2}} \right] \qquad (4.14)$$

where energy has converted to potential (U) using the Equation 4.5.

The Mott-Schottky plot and the surface state capacitance variation for the sample we have chosen to illustrate the surface recombination effect is shown in Figure 4.3. The solid line is the best fit to the surface state capacitance variation given by Equation 4.10 with the following parameters. U_t =-1.0 V vs SCE, σ =0.21 V, and N_t =6.6x10^{14} /cm^2. From the Mott-Schottky plot, N_D = 2.2 x10^{20}/cm^2 and U_{fb}=-0.8 V vs SCE. Hence, the space charge layer thickness (d) is expressed in terms of

$$d = (U + 0.8)^{1/2} \; 10^{-6} \text{ cm.} \qquad (4.15)$$

At positive potentials, surface recombination becomes zero because n_t tends to zero. Hence, using the Equation 1.37 and knowing α and d, we can evaluate L_p at positive potentials. For λ =350 nm and α =10^4 cm^{-1} the calculated value of L_p=5.5 x 10^{-6}cm. Equation 1.35 fits into the experimentally obtained quantum efficiency-potential curve with Equation 4.14. The best fit between experiment and theory is shown in Fig. 4.4, and the only adjustable parameter is $k_r^h N_t/2S_t$ = K/2 = 3.5 x 10^3. The other parameters are the same as the previously determined values. The adjustable parameter $k_r^h N_t/2S_t$ describes the relative rate of the surface recombination and the charge transfer process. The mechanism of transfering the minority carriers from the valence band to the reduced electrolyte states determines the charge transfer rate S_t.

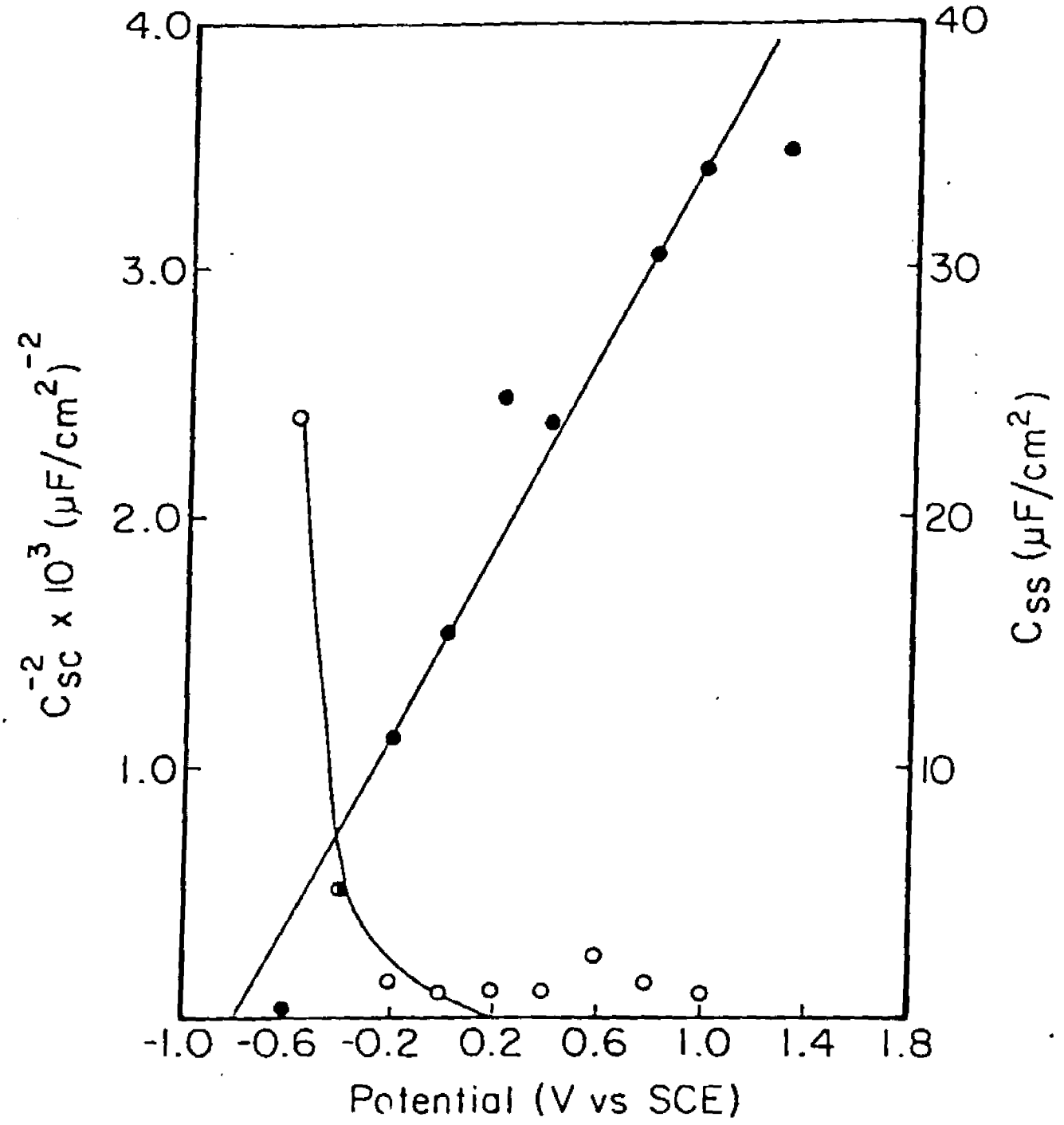

Fig. 4.3 Mott-Schottky plot of space charge layer (C_{sc}) and the variation of the surface state capacitance (C_{sc}). The solid line is the best fit to the Gaussian line-shape for C_{ss} with the following parameters. U_t=-1.0 (V vs SCE), σ =0.21 V, and N_t=6.6x10^{14}/cm^2.

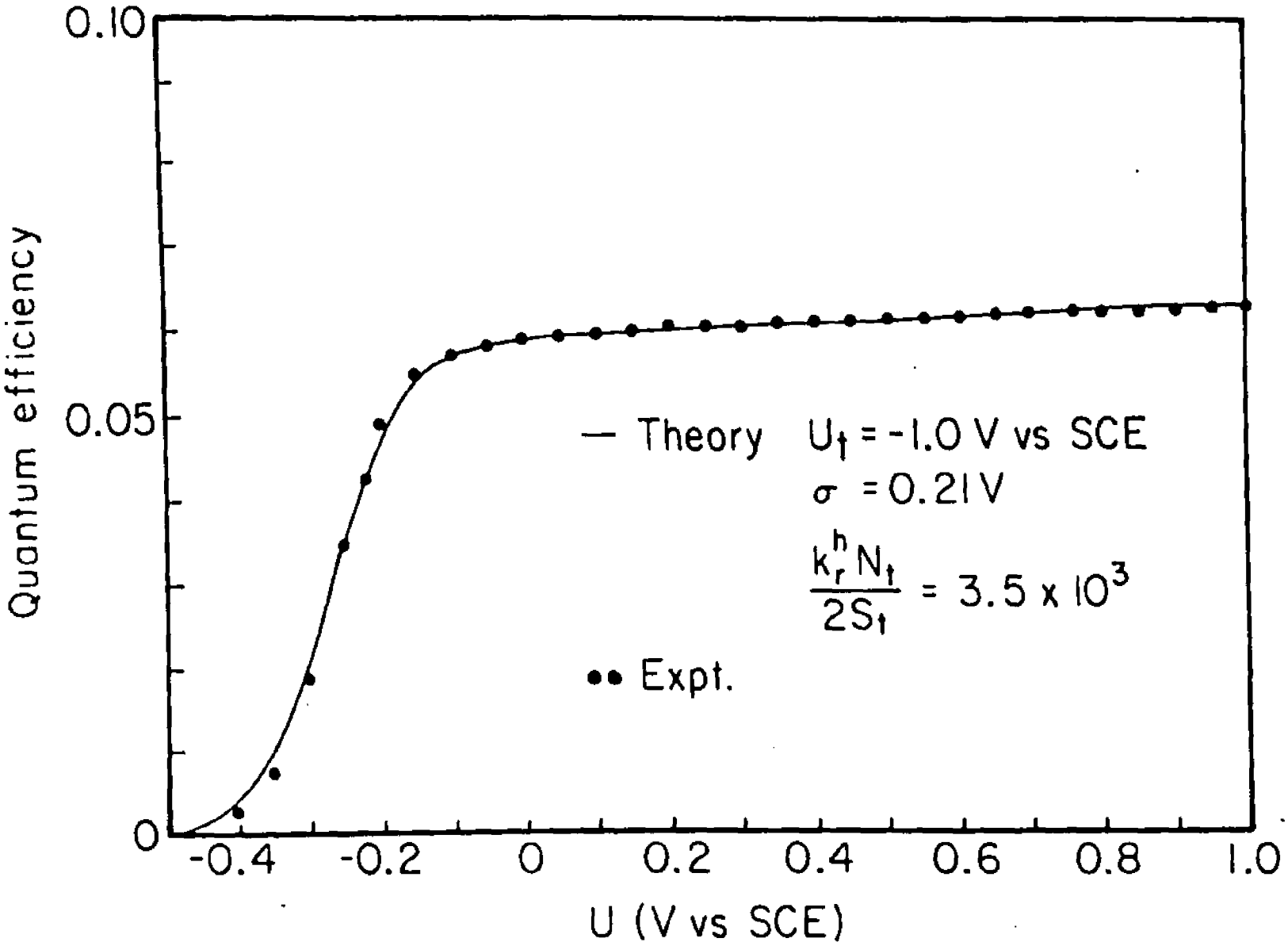

Fig. 4.4 Quantum efficiency vs electrode potential for n-TiO_2 in phosphatte buffer.

We assume here that the surface states participate as charge transfer intermediates (section 1.3.2). Assuming, in addition, that there is an isoenergetic charge transfer between the intermediate surface state and the reduced electrolyte states, S_t is limited by the available intermediate surface states. Hence, from Equation 1.32 we can estimate S_t as

$$S_t = v_{th} \sigma_t N_t^i \qquad (4.16)$$

where N_t^i is the concentration of the intermediate surface states. For simplicity, assume that hole capture cross section for recombination (σ_r) and for charge transfer (σ_t) is the same. Then, after inserting $N_t = 6.6 \times 10^{14}/cm^2$ in

$$k_r^h N_t / 2S_t = \sigma_r N_t / 2 \sigma_t N_t^i = 3.5 \times 10^3,$$

we obtained $N_t^i \sim 10^{11}/cm^2$.

As discussed in section 4.1.3(a), an efficient charge transfer between the valence band of TiO_2 and the O_2/H_2O redox couple must be via surface states, and the states that most likely to participate in this transfer process are those lying at 1.3 eV below the conduction band. The order of magnitude for the intermediate surface state concentration was estimated to be $10^{11}/cm^2$ in the electrolyte phosphate buffer, while the "intrinsic" surface state concentration

was actually found to be about $10^{12}/cm^2$ in 1M KI. The difference in order of magnitude is not surprising, because as we have already seen, the concentration of "intrinsic" surface states strongly depends on the nature of the electrolyte species, and it is much larger for KI than for the phosphate buffer.

4.1.4 (b)Photocurrent-Potential Response with Background Illumination

Since both the probe beam and the background illumination have energies above the bandgap of TiO_2, they are absorbed and induced the formation of carriers in a similar way. From Fig. 3.17 and Fig. 3.18 it is evident that the background illumination reduces the quantum efficiency in a similar way, as shifting the electrode potential toward flatband, and since we have shown already that surface recombination is the dominant recombination mechanism at potentials in which the sharp drop in quantum efficiency is observed, we are being forced to conclude that the dominant effect of the background illumination is through its contribution to surface recombination. In what will follow we will attempt to quantify this statement and test it for agreement with the experimental results.

The conventional interpretation of photoeffects on semiconducting electrodes assumes contribution from light induced minority carriers only, section 1.32. The argument is being that because of high concentration of majority carri-

ers, their incremental contribution is undetected. Recently, it was recognized that at negative potentials (for n-type semiconductors), light-induced majority carriers can penetrate through the barrier and make a contribution to the photoeffects [66,103]

A schematic diagram of the electron and hole fluxes at the interface is shown in Fig. 4.5. We do not know a priori what is the mechanism of penetration of majority carriers would be around or through the barrier, to interact with electrolyte. Regardless of the mechanism, we can assume it to follow a generalized Tafel-type equation [14,16]:

$$J_c^o = J_{oo} \exp(-\beta \Delta U) \qquad (4.17)$$

where J_{oo} is the exchange current at $\Delta U=0$, $\Delta U=U-U_{fb}$ is the barrier height, and J_c^o is the dark current. The constant β carries the information on the majority carrier transformation mechanism at the interface.

We will assume that when the semiconductor is illuminated, certain fraction of the light induced majority carriers will also penetrate the same barrier and flow to the surface. This methodology has been used before [103] to explain the decrease in collection efficiency for strongly absorbed light in Shottky diodes. Thus with this contribution, Equation 4.17 will be modified to yield,

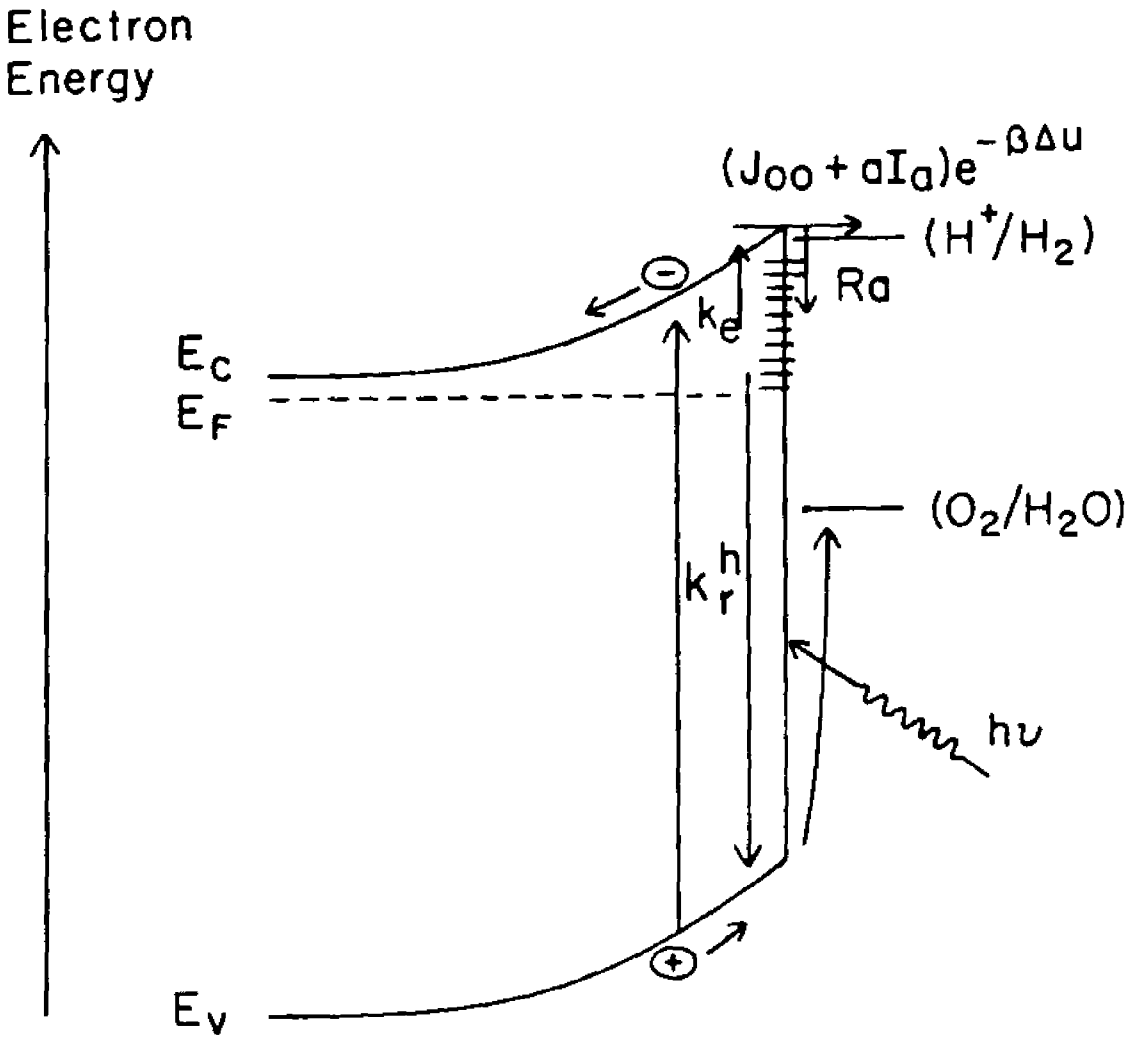

Fig. 4.5 Schematic diagram of the electron and hole fluxes at the semiconductor/electrolyte interface.

$$J = (J_{oo} + aI_a) \exp(-\beta\Delta U) \qquad (4.18)$$

where J is the total cathodic dark current and a is the quantum efficiency for light induced electrons to reach the surface when $\Delta U=0$.

The electron reaching the surface either interacts with the electrolyte or is captured by empty surface states. If $\varphi_{s.s}$ is the probability that these electrons will be captured by the surface states when all the avialable states are empty, then the rate of filling of the surface states, R_a, will be given by

$$R_a = \varphi_{s.s} \frac{(N_t - n_t)}{N_t} (J_{oo} + aI_a) \exp(-\beta\Delta U) \qquad (4.19)$$

where n_t is the density of occupied states. The emission rate of the electrons from the occupied surface states can be either emission to the conduction band at the rate $k_e n_t$ or recombination with minority carriers at the rate of $k_r p_s n_t$, where p_s is the hole density at the surface (see section 1.3.2). Since the anodic photocurrent can be expressed as

$$J_a = e S_t P_s \qquad (4.20)$$

and quantum efficiency as

$$\varphi = J_a/eI_a = S_t P_s/I_a \tag{4.21}$$

and

$$k_r^h P_s = (k_r^h \varphi/S_t) I_a = \gamma I_a \tag{4.22}$$

The total emission rate is

$$k_e n_t + \gamma I_a n_t \tag{4.23}$$

At steady state the emission rate will be equal to the rate of filling of the states, and from Equation 4.19 and 4.23 we arrive at

$$\varphi_{s.s} \frac{(N_t - n_t)}{N_t} (J_{oo} + aJ_a) e^{-\beta\Delta U} = k_e n_t + \gamma I_a n_t \tag{4.24}$$

and

$$\frac{n_t}{N_t} = \frac{(J_{oo} + aI_a)\varphi_{s.s} \exp(-\beta\Delta U)}{N_t k_e + N_t \gamma I_a + (J_{oo} + aI_a)\varphi_{s.s} \exp(-\beta\Delta U)} \tag{4.25}$$

For $I_a \longrightarrow 0$, i.e., when there is no illumination

$$\frac{n_t^o}{N_t} = \frac{J_{oo} \varphi_{s.s} \exp(-\beta\Delta U)}{k_e N_t + J_{oo} \exp(-\beta\Delta U)} \tag{4.26}$$

combining Equations 4.24,4.25 and 4.26

$$n_t = \frac{J_{oo} + a I_a}{J_{oo}/n_t^o + aI_a/N_t + \dfrac{k_r^h \varphi I_a e^{P\Delta U}}{S_t \varphi_{s.s}}} \qquad (4.27)$$

From equation 1.35

$$\varphi = \frac{S_t}{S_t + S_r} \varphi_{s=0}$$

where $\varphi_{s=0}$ is the quantum efficiency if there were no surface recombination. Using Equation 1.32, we can write:

$$k_r^h n_t = S_t (\varphi_{s=0}/\varphi - 1) \qquad (4.29)$$

Also, from the previous section:

$$k_r^h N_t/S_t = K = 7 \times 10^3 \qquad (4.30)$$

Thus we can write:

$$K n_t = N_t (\varphi_{s=0}/\varphi - 1) = N_t \qquad (4.31)$$

and

$$K\, n_t^o = N_t\,(\varphi_{s=0}/\varphi_o - 1) = N_t\,\Gamma_o \qquad (4.32)$$

where φ_o is the quantum efficiency with no background illumination. Substituting Equations 4.31 and 4.32 into 4.27 and rearranging the terms will yield

$$\frac{\Gamma^2 + (1-\Gamma_o) - \Gamma_o}{(1-\Gamma^2/K)I_a} = \left\{\frac{a\Gamma_o}{J_{oo}}\left[1-1/K-\frac{\varphi_{s=0}\exp(\beta\Delta U)}{a\varphi_{s.s}}\right]\frac{\Gamma}{(1-\Gamma^2/K)}\right\} + a\Gamma_o/J_{oo} \qquad (4.33)$$

The linear relation between the lefthand side of Equation 4.33 and $\Gamma/(1-\Gamma^2/K)$, at various electrode potentials, are shown in Fig 4.6. Γ and Γ_o were evaluated from Fig. 3.17 and Fig. 3.18.. From Equation 4.33, the ratio between the slopes and intercepts of the straight lines should give

$$\frac{\text{slope}}{\text{intercept}} = 1 - 1/K - \frac{\varphi_{s=0}\exp(\beta\Delta U)}{a\varphi_{s.s}} \qquad (4.34)$$

For $\delta = 1 - 1/K - \dfrac{\text{slope}}{\text{intercept}}$,

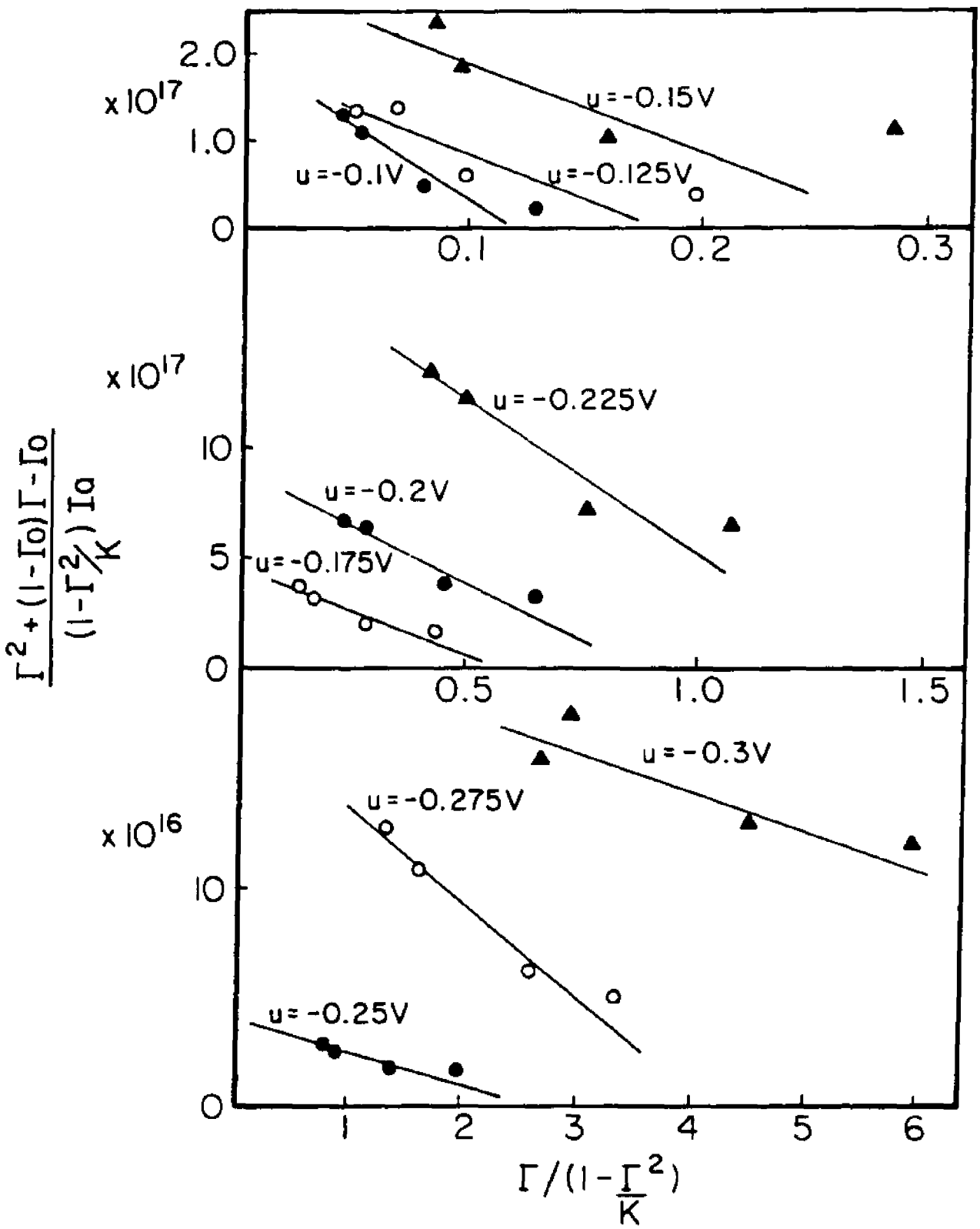

Fig. 4.6 $\frac{\Gamma^2 + (1-\Gamma_0)\Gamma - \Gamma_0}{(1-\Gamma^2/K)\, I_a}$ vs $\frac{\Gamma}{(1-\frac{\Gamma^2}{K})}$ at different electrode potentials. For more details see the text, Equation 4.33.

$$\ln(\delta/\varphi_{s=0}) = -\ln(a\varphi_{s.s}) + \beta U \qquad (4.35)$$

This relation is shown in Fig. 4.7. From the slope in Fig.4.7, β was found to be 13.1 V^{-1}. The linear relations found from Equations 4.33 and 4.35 represent the validity of the model we had proposed for the enhancement of the surface recombination due to background illumination. The extent of the validity of the assumptions that were made in Equations 4.18 and 4.24 can be tested by direct measurements of the dark current.

The potential dependence of the dark current is shown in Fig. 4.8, and the lograthemic representation of this current is shown in the insert of the same figure.As we have mentioned, in Equation 4.17, we did not know a priori the mechanism by whch the electrons are transferred from the semiconductor to the electroyte. However, this mechanism determines the value of β . From Fig. 4.8 one can clearly distinguish between two distinct mechanisms for the dark current, one that operates at potentials negative to -0.3 V vs SCE and one at potentials positive to that potential.

It is evident also from Fig. 4.7 that the linear realtion predicetd by Equation 4.35 breaks down near U=-0.3 V vs SCE, which is not surprising since Equation 4.17 invokes only a

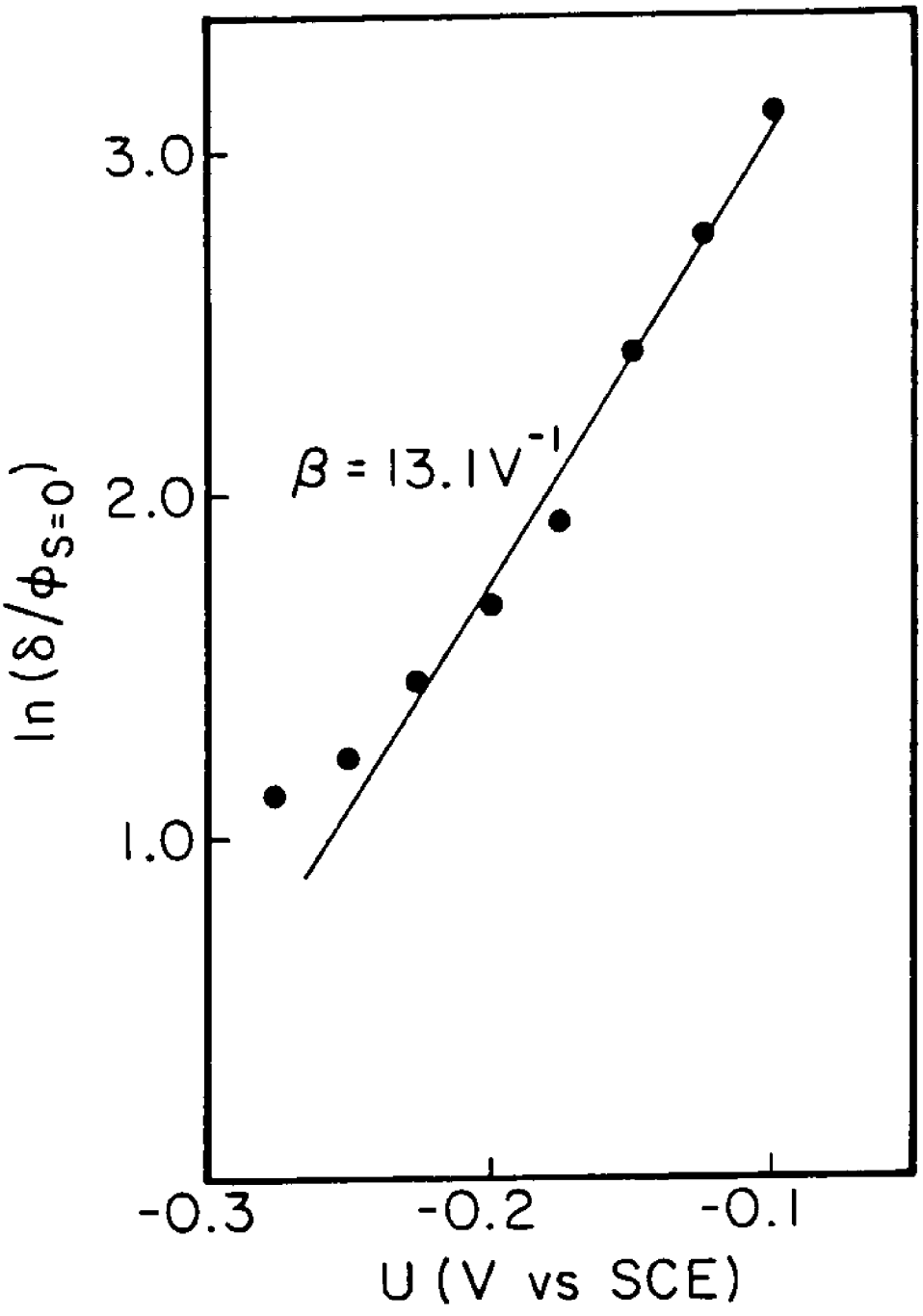

Fig. 4.7 $\ln(\delta/\Phi_{s=0})$ vs U.

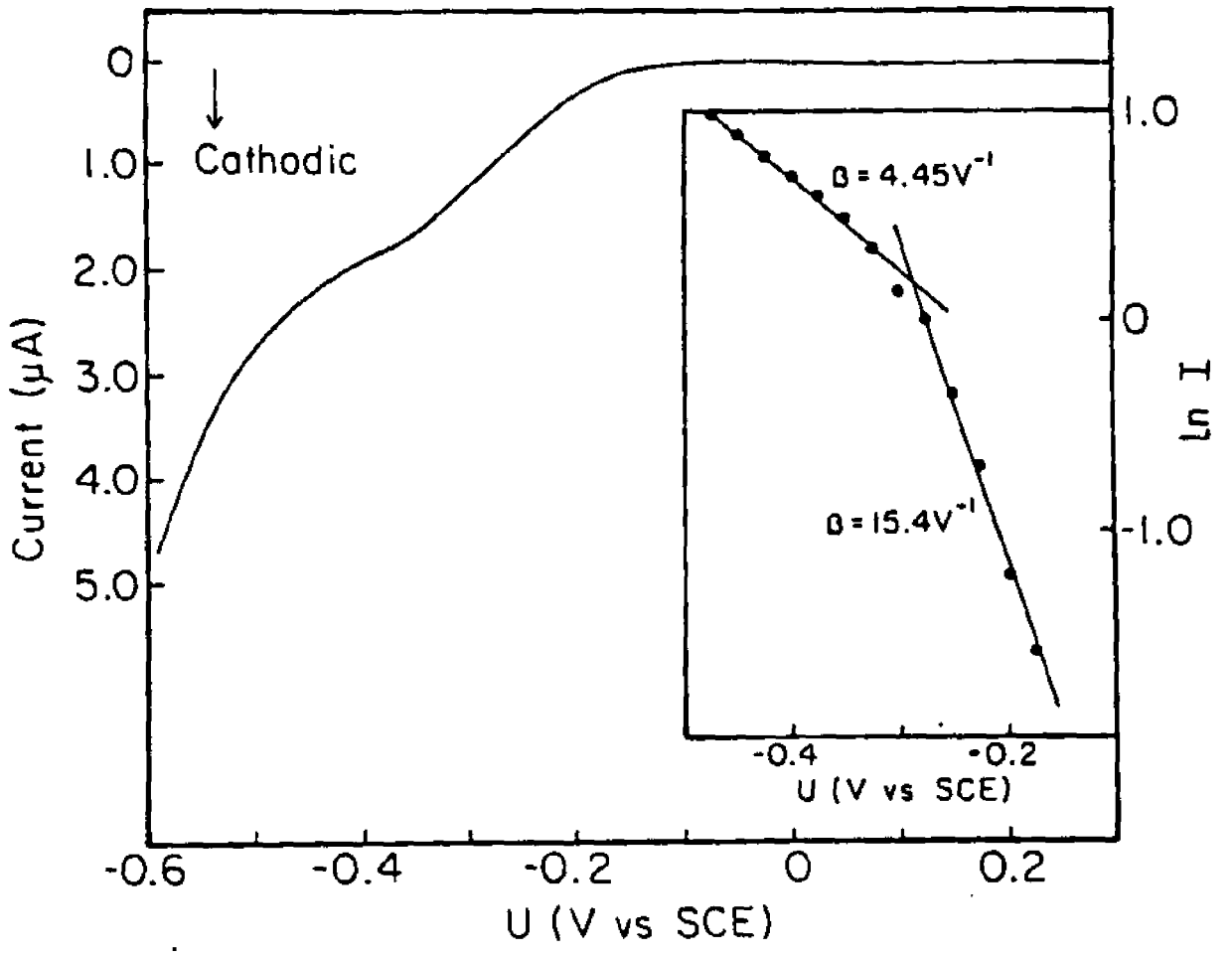

Fig. 4.8 Potential dependence of dark current, I, for n-TiO_2 in phosphate buffer. In the inset, logarithm of the dark current is shown.

single mechanism for the back reaction. The value of β obtained in Fig. 4.8 (in the potential range where the Fig. 4.7 shows a linear behavior) is 15.4 V^{-1}. This agreement in β beteween Figures 4.7 and 4.8 is an evidence of the validity of the assumptions made about the majority carrier transferring mechanism from semiconductor to electrolyte and also to the model presented for the background illumunation effect. It is of course, possible to extract from Figures 4.6, 4.7 and 4.8, the parameters appear in the model. However, inspite of the close agreement in β between Fig. 4.7 and 4.8, the 15% discrepancy beteween them and the exponential dependence on β makes such an evaluation unwarrented.

4.1.5 SBG Photoresponse and Dark Charge Transfer Intermediate at the n-TiO_2/Aqueous-Electrolyte Interface

As shown in Fig. 3.12, the SBG photoresponse follows a completely different current-potential behavior comparison with the bandgap photoresponse. This anomaly not only suggests that the generation and transfer mechanisms of SBG induced photorcarriers must be different from the bandgap photocarriers, but it excludes the possibility that the SBG photocurrent might have been caused by a bulk impurity band or by excitons. If the origin of photocarriers could be attributed to either of these reasons, we could then expect that the current-potential behavior should follow the same bandagp behavior. The SBG spectral response (Fig. 3.11), measured in the potential region where there is a maximum in

SBG photoresponse, shows a major optical transition around 2.2 eV. Hence, the combined result of the spectral response shown in Fig. 3.11 and the impedance measurements shown in Figures 3.2 and 3.3 indicate that the anodic SBG photocurrent is caused by light induced electrons injection from the valence band to the surface state lying at 0.8 eV below the conduction band. This state of event is shown in the band diagram in Fig. 4.9. The quenching of the SBG photocurrent (as shown in Fig. 3.15) due to the presence of oxygen in the electrolyte shows an alternative path for the photoexcited electrons, which could only be expected to exist if the SBG photocurrent was caused by a surface effect. The decline of the SBG and band-to-band photoresponse at cathodic potential is due to recombination at or near the surface. However, the decline of the photoresponse at anodic potential, which is unique, constitutes the essence of involvement in surface states. In the following we will show that this potential dependence of SBG photocurrent is consistent with the presence of surface states only when these states are formed dynamically by the dark current.

Hydrogen is seen to evolve at sufficiently negative potentials and we will assume that the reduction of water or hydronium ions to molecular hydrogen is responsible for the dark current. The large bandgap of TiO_2 and the position of the flatband potential necessiates that all dark current reactions take place via the conduction band. Base on these

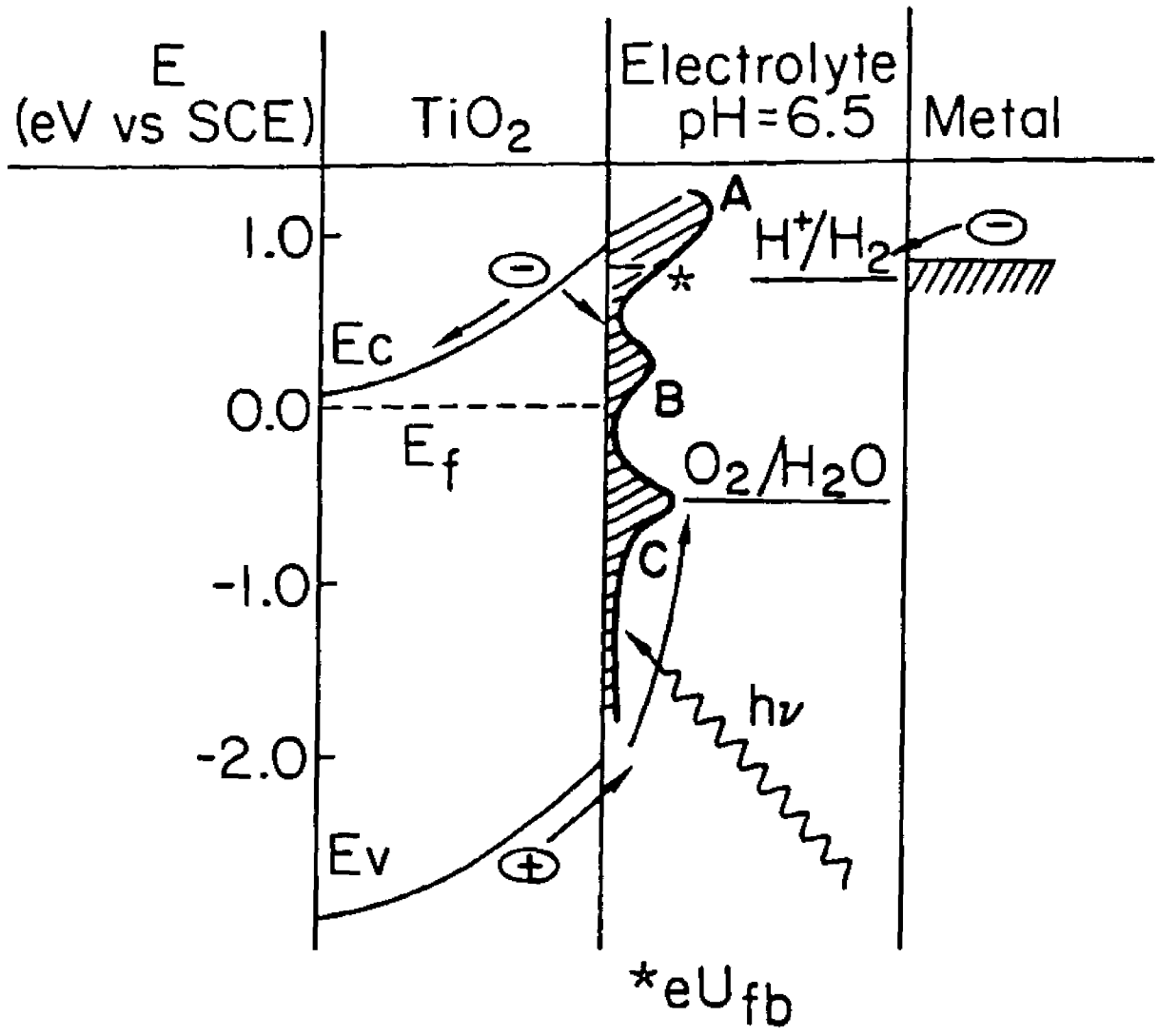

Fig. 4.9 Schematic representation of the energy band diagram of n-TiO_2/aqueous electrolyte interface.

assumptions we can write the following mechanism for the dark reaction:

$$e_d^- + TiO_2 + H_{aq}^+ \xrightarrow{k_1} TiO_2\text{—}H \qquad (4.36)$$

$$TiO_2\text{—}H + H_{aq}^+ + e_d^- \xrightarrow{k_2} TiO_2 + H_2 \qquad (4.37)$$

where TiO_2-H is the intermediate of the dark reaction and its energy lies within the bandgap of TiO_2, e_d^- is the conduction band electron that participates in the dark current, and H_{aq} is the proton in the aqueous elelctrolyte.

When the semiconductor is illuminated with SBG illumination electrons are excited from the valence band to the surface state at the rate of $\alpha\varphi I_a$, where φ is the quantum efficiency of the seperated electron hole pair, I_a is the incident photon flux, and α is the absorption coefficient of the SBG response. These electrons will compete with Equation 4.37 for the intermediate in the following way:

$$TiO_2\text{—}H + H_{aq}^+ + (h\nu)_{SB} \xrightarrow{\alpha\varphi I_a} h^+ + TiO_2 + H_2 \qquad (4.38)$$

Holes from the valence band will oxidize water to form molecular oxygen in the usual way. This mechanism is sche-

matic and should not be viewed as implying knowledge of the nature of the interacting electrolyte. If reaction 4.37 is rate limiting, then the d.c. dark current takes the the following form:

$$J_c = 2 e k_2 [H^+] n_d n_t \tag{4.39}$$

where n_d is the concentration of majority carriers at the surface, n_t is the concentration of active sites occupied by TiO_2-H, and e is the electronic charge. The steady state surface concentration of the intermediate is

$$n_t = \frac{k_1 n_d [H^+] N_t}{n_d [H^+](k_1+k_2) + \alpha \varphi I_a} \tag{4.40}$$

where N_t is the total concentration of the active sites on the TiO_2 surface. Inserting Equation 4.40 into Equation 4.39,

$$J_c = \frac{2ek_1k_2n_d^2 [H^+]^2 N_t}{[H^+]n_d(k_1+k_2) + \alpha \varphi I_a} \tag{4.41}$$

The dark current without the SBG illumination is:

$$J_c^o = \frac{2ek_1k_2 [H^+]n_d N_t}{(k_1 + k_2)} \tag{4.42}$$

If n_d can be determined by the elctrode potential in the dark, then the ratio between the two currents is:

$$\frac{J_c^o}{J_c} = 1 + \frac{2ek_1k_2N_t\alpha\varphi I_a}{(k_1 + k_2)^2 J_c^o} \tag{4.43}$$

The measured anodic a.c. signal, or the modulation of the dark cutrrent, is given by:

$$\Delta = J_c^o - J_c \tag{4.44}$$

$$= \frac{\alpha\varphi I_a}{K + \alpha\varphi I_a/J_c^o} \tag{4.45}$$

where

$$K = (k_1 + k_2)^2/2ek_1k_2N_t$$

The linear dependence of the SBG phtocurrent (shown in Fig. 3.16) implies that:

$$\alpha\varphi I_a/J_c^o << K \tag{4.46}$$

and therefore

$$\Delta = \alpha\varphi I_a/K \tag{4.47}$$

At positive potentials J_c^o becomes very small, and Equation 4.47 will no longer holds. We can express the dark current in terms of a Tafel-type equation given by 4.17, and inserting 4.17 into 4.45 results in

$$\Delta = \frac{\alpha\varphi I_a}{K + \dfrac{\alpha\varphi I_a}{J_{oo} \exp(-\beta\Delta U)}} \tag{4.48}$$

We have shown previously that at the maximum of the SBG photcurrent-potential curve, Equation 4.47 holds. Therefore:

$$\Delta^{max} = \alpha\varphi I_a/K \tag{4.49}$$

Using Equation 4.49 in Equation 4.48 and rearranging the terms gives

$$\ln(\Delta^{max}/\Delta - 1) = \ln(\Delta^{max}/J_{oo}) + \beta U \tag{4.50}$$

This equation is plotted in Fig. 4.10, and it explains quantitatively the decline of the signal at more positive potentials. The decline of the signal cathodic to the maximum is due to the inability for Equation 4.38 to compete with Equation 4.37, at these potentials, thus causing the quantum efficiency for the charge seperation to decline as we approach the flatband potential. This process is not reflected in Equation 4.48, which saturates in the negative potential range owing to the omission of the recombination process in the kinetic formulation. The SBG photoexcitation is not responsible for a new kind of photoanodic current. Since this radiation induces simultaneous oxidation and reduction of the electrolyte, it is more appropriate to view it as recombination through the electrolyte. However, because of the limited number of adsorption sites, the photogenerated electrons compete with majority carriers for the limited number of sites, thus reducing the d.c. dark current that will manifest itself as an a.c. anodic photocurrent.

In a recent publication by Dare-Edward et al. [66], the photogeneration of hydrogen on a p-type semiconductor was investigated using a similar method and achieving similar findings to those presented here for n-TiO_2. They estimated that p-GaP-H is about 800 mV anodic of the total energy of the hydrogen evolution reaction. Considering that the flatband potential of TiO_2 is about 100 mV negative of the standard hydrogen electrode and the surface state lies around

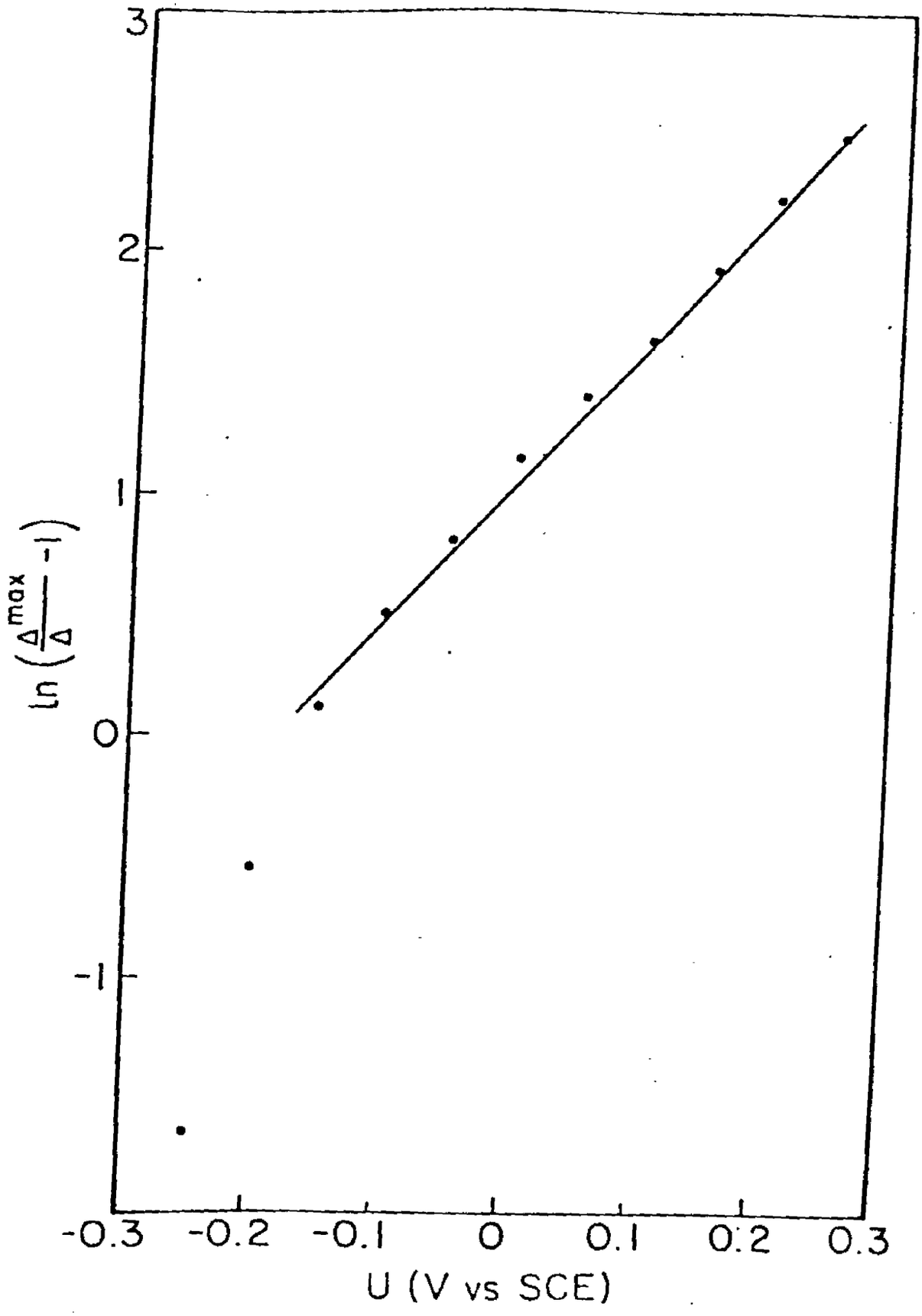

Fig. 4.10 $\ln(\frac{\Delta^{max}}{\Delta} - 1)$ vs U.

0.8 eV below the bottom of the conduction band, the energy of the intermediate state is identical and within the accuracy of all these determinations, independent of the nature of the electrolyte.

4.1.6 Surface States Tailing from the Conduction Band Edge at the n-TiO_2/Aqueous-Electrolyte Interface

The dominant state in the surface state density distribution at the n-TiO_2/aqueous-elelctrolyte interface is the one that tails from the edge of the conduction band into the bandgap of TiO_2. We have seen in section 4.1.4 that this surface state band is mainly responsible for the surface recombination of the photocarriers at the interface. Similar surface state density distribution has been reported by Tomkiewicz [52,64] on the surface modified TiO_2 electrodes. Wilson [31] also found evidence of similar surface state distribution with TiO_2 electrodes in contact with aqueous electrolytes. It is therefore important to understand more about the nature of this surface state band.

As already mentioned, there are many possible reasons for a tailing surface state band. One possibility is the chemisorption of OH^- radicals at the surface cation sites via their negative O atoms. Kowaski et al. [50] have shown theoretically that this type of adosrption gives rise to surface states in the upper half of the bandgap of TiO_2. Tomkiewicz [52] has proposed that a broad surface state band may result at the TiO_2/aqueous electrolyte interface due to OH adsorp-

tion, and further, this band may provide efficient charge transfer intermediates at the interface. Gutierrz and Salvador [69] have suggested that not one but two types of surface states, one at the conduction band and the other at the valence band, may result at the TiO_2/aqueous-electrolyte interface due to OH adsorption. Thus, adsorption of OH radicals may be a possible reason for the existence of a tailing surface state band.

Another reason might be the unsolvated intrisic surface states available at the TiO_2 surface. According to Kasowaski and Tait [94], there is a large number of empty states available at the conduction band of TiO_2. Some of these surface state may move away from the bandgap as a result of doping,but as already mentioned in regard to "intrinsic" (defect) surface states, we can expect some of them to remain in the bandgap of an unsolvated surface.

We have mentioned before that when the surface is solvated, or when the intrinsic (or defect) surface states interact orbitaly with the adsorbed species, the surface states move away from the bandgap. The new surface states may form a tail part extending into the bandgap as a result of the band broadening process.

Taking into account all the possibilities mentioned above, it is not possible to give an exact reason for the tailing surface state band. However, it is clear that this surface state band has a great influence on the efficiency

of this system as a photelectrolytic solar cell because it is able to act as an efficient surface recombination center.

4.2 FERMI LEVEL PINNING AT THE SEMICONDUCTOR/ELECTROLYTE INTERFACE

We have already mentioned in the previous sections that Fermi level pinning at the semiconductor/electrolyte interface is due to the presence of a high density of mid-gap surface states, and that is governed entirely by the charging and discharging of these states. Complete Fermi level pinning, where the Fermi level at the interface is determined solely by the surface states and not by the applied bias, means that the Fermi level at the surface is fixed and that externally applied voltage only appears across the Helmholtz layer. In a partially pinned surface, externally applied voltage is shared by both the space charge layer and the Helmholtz layer, resulting in a potential dependent flatband potential at the interface. This modification in the potential distribution necessarily gives rise to new interfacial characteristics and greatly influences the device performance.

We have seen before that the n-TiO_2/aqueous electrolyte interface does not show much evidence of Fermi level pinning. However, a $CdIn_2Se_4$/aqueous-polysulfide system does show strong evidence of it because of potential dependence of EER. The EER signal in Fig. 3.21 strongly depends on the applied d.c. bias, owing to the fact that in the presence of

surface states that are fast enough to equilibrate at the modulation frequency, the modulation voltage drops somewhat partially across the Helmholtz layer resulting in a decrease in the modulation amplitude on the space charge layer. This decrease in modulation amplitude causes a decrease in the EER signal as given in Equation 2.24. In addition to this effect, it is evident from Figures 3.20 and 3.21 that the EER lineshape and the potential variation of the EER signal are sensitive to the surface photoetching of the sample. In the following sections we will investigate the possible cause for this surface effect and study the Fermi level pinning in more detail.

4.2.1 EER Spectra for $CdIn_2Se_4$ in Aqueous Polysulfide Electrolyte

As shown in Fig. 3.20, the lineshape of the EER signal sharpenes considerebly with photoetching, and the characteristic third derivative [78] lineshape appears once the surface is treated in this way. In view of the gross differences in the lineshape of the EER before and after photoetching, as well as the apparent shift in the peak position, the main question is whether chemical changes involved in the photoetching process are actually selective and give rise to different band structure parameters, or that change in ER can be accounted for by the selective photoetching of defects that manifest themselves through changes in the field distribution at the surface and the intrin-

sic line width of the EER signal. The answer to this question is essential to the study of surface states and Fermi level pinning at the interface. The phase factor θ , one of the parameters that determines lineshape (Equation 2.25), in addition to a contribution from the Seraphin Coefficient [104], will contain contribution from electron-hole coulomb interaction and from inhomogenieties in the electric field distribution in depth determined by the penetration depth of the light [79]. We would expect that if photoetching does not alter the chemical composition through selective etching, but changes drastically the defect concentration, that will be the most sensitive parameter that will be modified by the treatment, while n and E_g remain unchanged. The four parameters that determine lineshape were fitted to the spectra of the sample after photoetching. The best fit of the experimental data to the theoretical lineshape function is shown in Fig. 3.20 (b) with the parameters:n=2.5, E_g=1.825 eV, and θ =315.5^{o} , and Γ =0.316 eV.

The fitting of Equation 2.25 to the spectrum of the sample before photoetching was done by keeping E_g and n constant and changing only θ and Γ . The experimental and theoretical curves for this sample are shown in Fig. 3.20(a). A shift of 98^{o} to 217.5^{o} is shown in θ ,while the broadening parameter increases by about 30% to 0.416 eV. Since we do not expect the Seraphin coefficient and the electron-hole coulombic interactions to change from the surface treatment,

we conclude that this large change in θ is entirely due to changes in the inhomogeinieties in the electric field distribution owing to the surface treatment. This conclusion is supported by the considerable improvement in performance after photoetching [86]. The energy gap found here is on the high energy side of previously reported values that were evaluated by photoresponse [86],absorption measurements [105], and thermoreflectance [105].

4.2.2 Fermi Level Pinning at the $CdIn_2Se_4$/Aqueous-Polysufide Interface

We can obtain a quantitative expression for the decrease in the EER signal due to Fermi level pinning by examining the change in modulating voltage across the space charge layer. According to Equation 1.13, the modulating voltage (δU) is diveded as:

$$\delta U = v_{sc} + \delta V_H \tag{4.51}$$

where v_{sc} is the modulated voltage drop across the space charge layer, and δV_H is the drop across the Helmholtz layer. Also, from Equation 4.1

$$\delta V_H = \frac{e}{C_H} \delta N_{ss}^{+} \tag{4.52}$$

where N_{ss}^{+} is the area concentration of the ionized surface states. Combining Equations 2.24, 4.51, and 4.52 results in an expression for the EER signal, which demonstrates the effect of Fermi level pinning:

$$\frac{\Delta R}{R} = K \left(1 - \frac{e}{C_H} \frac{dN_{ss}^{+}}{dU} \right) \tag{4.53}$$

where

$$K = - \frac{2eN_D}{\epsilon_s} L(\hbar\omega) \tag{4.54}$$

The modulating potential dU is taken to be a small displacement of the d.c. electrode potential. Within the low-field regime, $\frac{\Delta R}{R}$ should be independent of the d.c. potential and decreases for $dN_{ss}^{+}/dU > 0$, namely for n-type semiconductors when anodic shift of the electrode potential results in an incremental ionization of the surface states. Within this regime, $\frac{\Delta R}{R}$ is maximum for $dN_{ss}^{+}/dU = 0$ and decreses inversely with dN_{ss}^{+}/dU. This behavior is demonstrated in our result shown in Fig. 3.21, and it can be expressed in close form as

$$P = \frac{e}{C_H} \frac{dN_{ss}^{+}}{dU} = 1 - \frac{\Delta R/R}{(\Delta R/R)_{max}} \tag{4.55}$$

Equation 4.55 is valid provided that $(\Delta R/R)_{max}$ occurs when $dN_{ss}^{+}/du = 0$, still within the low-field regime. If this condition is satisfied, EER provides direct measuremtns of $\frac{1}{C_H}\frac{dN_{ss}^{+}}{dU}$ and is advantageous because it involves direct differential measurements, not the total system response as do the measurements of impedance. Since changes in the flatband potential originate from the changes in the potential drop across the Helmholtz layer (Equation 4.1), it follows from Equation 4.55 that

$$P = \frac{dU_{fb}}{dU} \tag{4.56}$$

and therefore

$$U_{fb} = U_{fb}^{o} + \int_{U_{max}}^{U} P\, dU \tag{4.57}$$

where U_{max} is the potential at which $(\Delta R/R)_{max}$ is maximum.

Equation 4.57 is valid within the assumptions that led to equation 4.55, which can be restated in terms of U_{fb}^{o} such that at $U=U_{max}$, the flatband potential is still U_{fb}^{o} because $dN_{s}^{+}/du=0$. Since $\int_{U_{max}}^{U} Pdu$ can be evaluated directly from the EER data (see Fig. 3.20). Equation 4.57 provides an experimentally accessible way for determining U_{fb} as a function of electrode potential. Fig. 4.11 shows the estimated shift in the flatband potential of $CdIn_2Se_4$ before and after the pho-

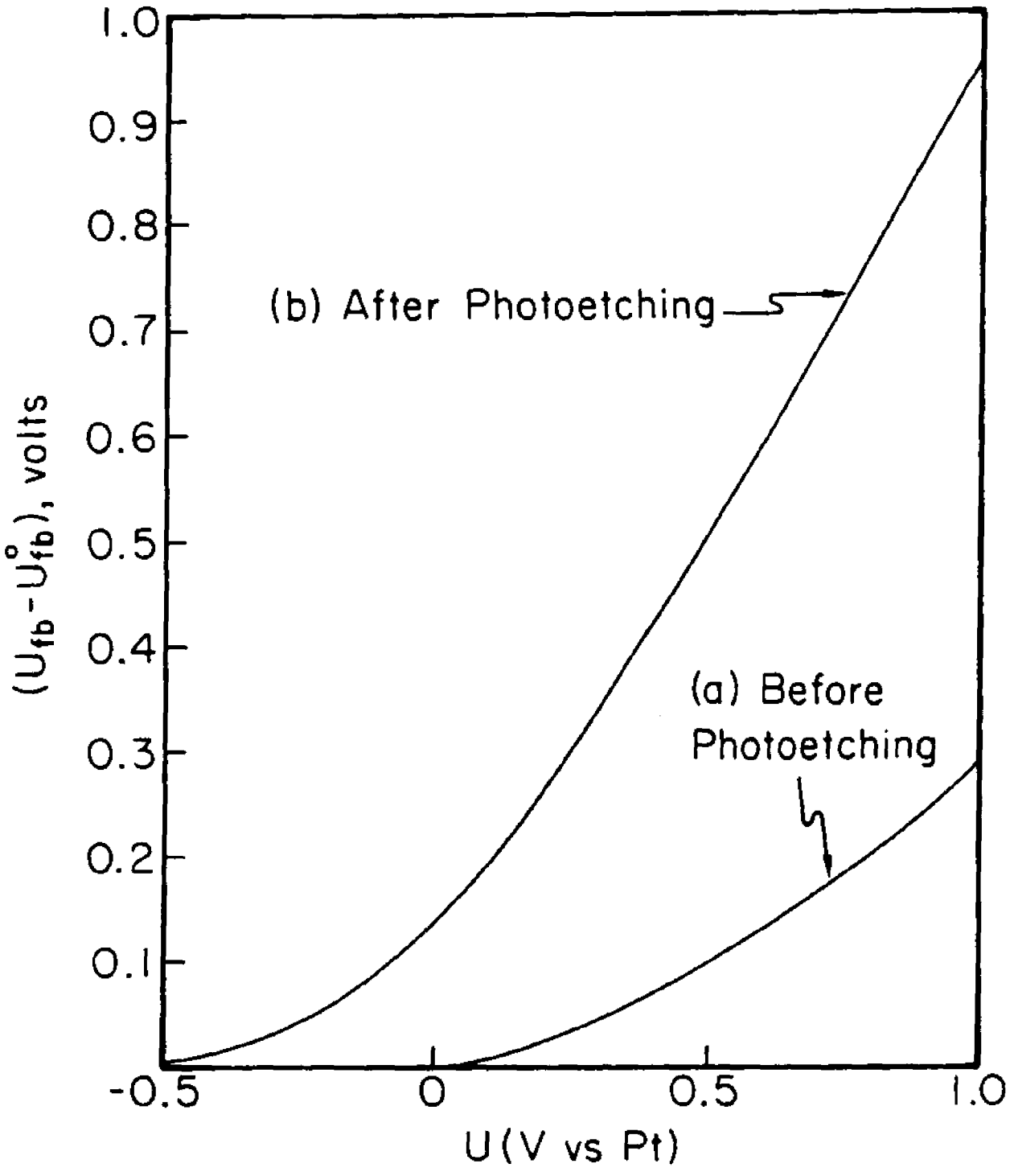

Fig. 4.11 Shift in the flatband potential with the potential for $CdIn_2Se_4$ in aqueous polysulfide, befor (a) and after (b) photoetching.

toetching experiment. Consistent with Fig. 3.21, the photoetching increased the pinning of the Fermi level. The observation that the Fermi level is getting more pinned upon photoetching is surprising. We do not offer a satisfactory explanation for this phenomena. It is assumed that for the potential U_{max} in which $\Delta R/R$ is maximum, $U_{fb}=U_{fb}^{o}$ and there is no pinning. If this assumption proves to be incorrect, and at $U=U_{max}$ the Fermi level is already pinned to a different degree in the two samples, then of course Fig. 4.11 will have to be modified and the conclusion derived from this figure re-evaluated.

In order to clarify this point, we have to find conditions in which the Fermi level is unpinned throughout the potential region. In addition, an independent evaluation of both U_{fb} and the doping level has to be made and variations in these parameters caused by photoetching have to be studied. We were unable to carry out these experiments because only one small wafer was avilable to us and by the time we had finished the theoretical treatment and realized what additional parameters needed to be measured, the crystal had severe corrosion because it was remained in the polysulfide solution for a few months.

4.2.3 Characterization of the Surface Sates Responsible for the Fermi Level Pinning

We assume a gaussian energy distribution of surface states given by the Equation 4. 2. The transformation equations given in 4. 7 are redifened using Equation 4.57 to accomodate the Fermi level pinning, such as

$$F_F = -eU$$

$$E_c = -eU_{fb} = -eU_{fb}^o - e\int_{U_{max}}^{U} P\,dU \qquad (4.58)$$

$$E_t - E_c = E_t^o - E_c^o = -eU_t^o + eU_{fb}^o$$

Using Equations 4.9 and 4.58 leads to the folowing expression for the number of ionized surface states

$$N_{ss}^{+}(U) = \frac{N_t}{2}\left[\operatorname{erf}\frac{-U_t^o+U-\int_{U_{max}}^{U} P\,dU}{6\sqrt{2}} - \operatorname{erf}\frac{-U_t^o+U_{fb}^o}{6\sqrt{2}}\right] \qquad (4.59)$$

Differentiation of Equation 4.59 with respect to U and application of Equation 4.55 and 4.56 yield

$$\frac{P}{1-P} = \frac{eN_t}{C_H 6(2\pi)^{1/2}}\left[\exp -\frac{1}{2\sigma^2}\left(U_t^o - U + \int_{U_{max}}^{U} P\,dU\right)^2\right]$$

(4.60)

The three unknown parameters in Equation 4.60 are U_t^o, and N_t/C_H . The solid lines in Fig. 4.12 are the best fit of Equation 4.60 to the experimental results that were calculated from the data in Fig. 3.20. The parameters that were evaluated from this fit are:

before photoetching:

$$U_t^o = 0.823 \text{ V vs Pt}, \sigma = 0.4 \text{ V}, \text{ and } eN_t/C_H = 0.88 \text{ V}$$

and afetr photoetching:

$$U_t^o = 0.172 \text{ V vs Pt}, \sigma = 0.1 \text{ V}, \text{ and } eN_t/C_H = 6.88 \text{ V}$$

The fit is good in both case for the reverse bias conditions. It is not as good under forward bias conditions, where the degree of pinning is small, since (a)P/(1-P) is less sensitive to $(\Delta R/R)_{max}$ as we go towards reverse bias, and (b) the low-field regime assumption breakes as we go towards forward bias when the penertation depth of the light exceeds the penetration depth of the electric field. If we take $C_H = 30\ \mu F/cm^2$, then $N_t = 1.7 \times 10^{14}/cm^2$ applies for the chemically etched surface and $N_t = 1.3 \times 10^{15}/cm^2$ applies for the photoetched surface. Since this analysis is based on the same data as the one in Fig. 4.11, it is not surprising that the coverage of surface states increases with photoetching. The total coverage is smaller when the sample is etched chemically, but the width of the surface state band is considerably greater than when the surface is photoetched. The difference in width is not due to overlap or to the reorganization of solvent, but more likely to surface heteroge-

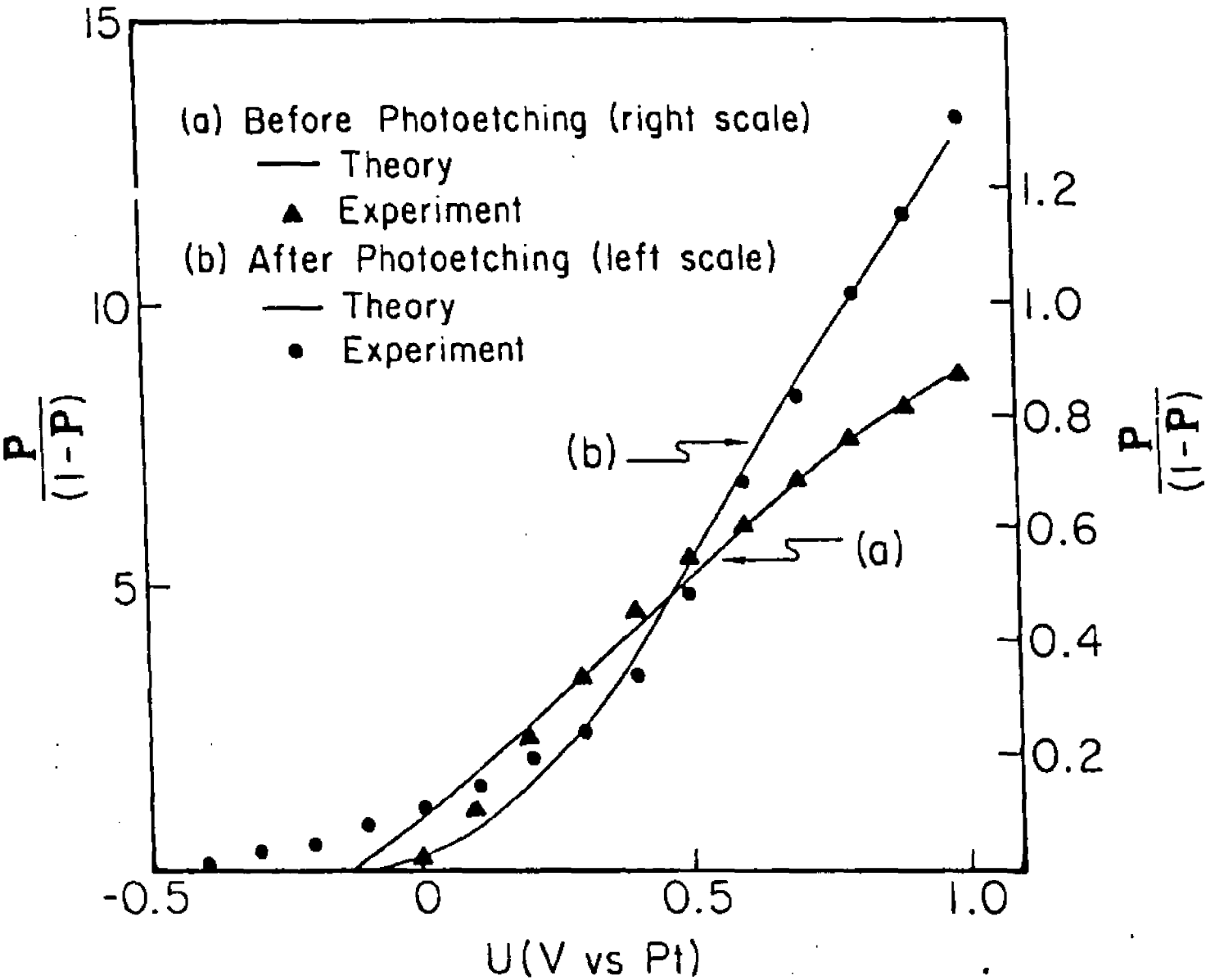

Fig. 4.12 P/(1-P) vs potential.

niety (section 1.4.3), which is much more pronounced in the chemically etched surface than in the photoetched one. This result is consistent also with the EER lineshape parameters derived in section 4.2.1.

Since surface heterogeniety plays a much less important role in the photoetched sample, the number of states are easier to identify using the photoetched sample. U_t^o agrees with the rest potential of the electrode, which is determined by the oxidation-reduction of the adsorbed ions according to the following equation

$$S_x \rightleftharpoons xS + 2e^- \qquad (4.61)$$

It is also the potential of counter electrode.

If the adsorbed polysulfide constitutes the surface states which are responsibe for the Fermi level pinning, it is clear that it will be impossible to remove them without destroying the cell as a photovoltaic device. In that case, the only accessible way to remove Fermi level pinning is to slowing down the dark reaction responsible for the ionization of these states. It has been demonstrated that removal of Fermi level pinning is possible, since single crystal CdSe in polysulfide electrolyte did not show any evidence of Fermi level pinning, while a strong pinning effect similar to the ones that were observed here was indeed present in the same electrolyte with polycrystalline CdSe [67.68].

4.3 SUMMARY AND CONCLUSIONS

Three experimental techniques, relaxation spectrum analysis, photocurrent spectroscopy, and electrolyte electroreflectance spectroscopy, were employed to identify and characterize the surface states at the n-TiO_2/aqueous-electrolyte interface of photoelelctrolytic solar cells. These measurements resulted in three distinct surface states at this interface. Measured photocurrent-potential behavior was fully accounted by the proposed surface recombination mechanism of photogenerated carriers. The EER study on a $CdIn_2Se_4$/aqueous polysulfide system showed that EER spectra are sensitive to the surface preparations of the semiconductor and that there is strong evidence for Fermi level pinning at the interface. Evaluation of the surface state density distribution responsible for the pining was made.

From the combined results of the impedance measurements and the SBG photocurrent measurements, it was found that a surface state band exists at about 0.8 eV below the conduction band of TiO_2 photoelectrodes in contact with aqueous electrolytes. The SBG photoresponse was found to be the result of the excitation of electrons from the valence band to these surface states. Origin of the states were identified as dark charge-transfer intermediates, and their proposed mechanism of dynamic formation and annihilation was fully accounted for the unique SBG photocurrent-potential behavior.

Surface states located at 1.3 eV below the conduction band of TiO_2 were detected with SBG EER measurements in the presence of electrolytes that can adsorb on the surface of TiO_2. The energy of these states was found to be independent of the nature of the electrolyte, but the intensity of the transition correlated with the expected tendency of adsorption. The potential distribution at the interface as a function of the electrolyte was investigated with impedance measurements using the relaxation spectrum analysis technique. It was found that not only does the adsorption of foreign ions influence the potential distribution at the interface by shifting the flatband potential, but that the surface states at 1.3 eV appeared as a direct consequence of this adsorption process. This results were interpreted in terms of "intrinsic" surface states of the unsolvated surface that shift towards the band edges as they interact with the solvent and reappear when an adsorbate can dispalce the solvent molecules without orbital interaction with these states. Further, it was recognized that these "intrinsic" surface states were the previously reported defect surface states at the (001) surface of TiO_2.

Impedance measurements has given evidence of the existence of a dominant surface state band that tails from the conduction band of TiO_2. The possible origin of this surface states (e.g., those caused by the adsorption of the electrolyte species and/or solvent molecules and the unpopulated

intrisic ones at the conduction band edge etc.) was discussed. Some uncertanity, however, remain as to the origin of this tailing surface state band.

The photocurrent-potential behavior of n-TiO_2 photoelectrodes in an aqueous electrolyte was investigated. A surface recombination process fully was fully accounted for the observed photocurrent-potential behavior. A total of four parameters were used to characterize the surface states involved in this surface recombination mechanism, two of which appear in the expressions for the quantum efficiency-potential dependence and the capacitance resulting from these states. The other two parameters appear sepertely in conjunction with each experiment. Further, the intermediate states involved in the charge transfer process between the valence band of TiO_2 and the electrolyte (i.e., the catalytic process of photo-oxidation of water) was speculated to be the involvement of "intrinsic" surface states located at 1.3 eV below the conduction band of TiO_2. The effect of background illumination was interpreted as the change in the equilibrium distribution of the surface states resulting in the increase in surface recombination of photocarriers. The final step in this procedure enabled us to predict the rate of change of the dark current with electrode potential which agrees well with direct measurements of the dark current.

EER was used to evaluate the optical properties of $CdIn_2Se_4$ in polysufide solution before and after photoetch-

ing. The variation of the signal intensity with electrode potential was used to trace the band position as a function of potential, the effect of Fermi level pinning. It was found that the optical transition fits a three-dimensional parabolic model of the density of states, with direct transition at 1.825 eV. When the crystal is photoetched, there is a shift of 98 in the phase factor and a decrease in the broadening parameter from 0.42 to 0.32 eV. The signal variation with the potential showed that, irrespective of photoetching, the Fermi level is pinned as we approach reverse bias conditions. We calculated the variation of the flatband potential with the electrode potential and also the energy distribution and density of surface states, that responsible for the Fermi level pinning. We ascribe the Fermi level pinning to the surface states that had originated from the adsorption of the electrolyte.

The main conclusions that can be drawn from this work are as follows:

1. Three experimetal techniques, relaxation spectrum analysis, photocurrent spectroscopy, and electrolyte electroreflectance, prove to be applicable in conjunction with each other for the detailed study of surface states at the semiconductor/electrolyte interafce of n-TiO_2 electrodes in aqueous electrolytes.

2. In general, three major surface states bands are present at the TiO_2/aqueous-electrolyte interface. The dominant

one is the surface state that tails from the conduction band edge to the bulk bandgap, and the other two are located at 0.8 eV and 1.3 eV below the conduction band.

3. The surface state located at 0.8 eV is associated with the charge transfer intermediate TiO_2-H at the interface, and this state is responsible for the observed SBG photocurrent through the mechanism of dynamic formation and annihilation.

4. The surface state located at 1.3 eV is "intrinsic" in nature, and it is associated with the defect sites at the (001) surface of reduced TiO_2. At the n-TiO_2/aqueous-electrolyte interafce, these "intrinsic" surface states appear when the surface is unsolvated. They shift toward the band edges while interacting with the solvent and reappear when an adsorbate can displace the solvent molecule without orbital interactions.

5. The large tailing surface state band at the n-TiO_2/aqueous-electrolyte interface may be the result of the adsorption of electrolyte and/or solvent molecules (or ions) and the existance of unpopulated intrinsic surface states, but the exact cause is not clear. This surface state band is mainly responsible for the surface recombination of photogenerated carriers.

6. EER spectroscopy in the SBG energy range can be used to identify the surface states at the semiconductor/elelctrolyte interface by localizing the electric field modula-

tion at the surface of the electrode, i.e., by maintaining the near flatband conditions. This was responsible for the EER peak observed at 1.3 eV in the presence of electrolytes that can adsorb on the surface of TiO_2.

7. The bandgap photocurrent-potential behavior of n-TiO_2 photoelectrodes in aqueous elelctrolytes is fully accounted by the surface recombination of photocarriers. The tailing surface state band is responsible for the surface recombination process. High injection of majority carriers at the interface may enhance the surface recombination process in forward bias condition by the increase in occupied surface state concentration, accounting for the observed decline in photocurrent due to background illumination.

8. At the TiO_2/aqueous-electrolyte interface, the "intrinsic" surface state present at 1.3 eV below the conduction band has been shown to be an active participant in the photoproduction of oxygen (i.e., catalizes the photoelectrolysis process).

9. The potential distribution at the semiconductor/electrolyte interface could be modified by (a) the specific adsorption of foreign ions on the electrode surface and (b) a high density of surface states. TiO_2 electrodes in aqueous electrolyte such as KI demonstrate this effect.

10. EER can be used to evaluate the surface state density distribution at the semiconductor/electrolyte interaface, that is responsible for the Fermi level pinning. A

$CdIn_2Se_4$/aqueous polysulfide system showed this effect, and a detailed analysis led to the surface state density distribution at this interface.

4.4 FUTURE WORK

As a direct result of the work we have performed, we can suggest the following future work that may lead to further understanding on the semiconductor/electrolyte interface in general, and on the TiO_2/electrolyte interface in particular.

The general surface state distribution we observed with TiO_2 was directly or indirectly associated with the aqueous electrolytes. The same study on TiO_2 electrodes in nonaqueous electrolytes is important, since the unsolvated surface would result in different surface characteristics. Furthermore, different adsorption processes in different species can be studied using the same experimental techniques exploited here.

The study of surface orientations in contact with aqueous and nonaqueous electrolytes may also result in different surface characteristics, owing to differences in Ti and O coordination in different surfaces of TiO_2.

The detailed study of photocurrent-potential behavior of TiO_2 in different electrolytes might be a subject for further investigation of the involvement of "intrinsic" surface state band on photocatalytic activity. These experiments, in

conjunction with impedance and SBG EER, can be used for a quantitative evaluation of photcatalytic behavior.

The specific adsorption process that led to a surface state band at 1.3 eV below the conduction band of TiO_2 can be further investigated by varying the concentration of ions in the solution until saturation in the adsorption process is reached. Saturation can be monitored with impedance and SBG EER measurements, and the saturation point could be correlated with (a) the maximum "intrinsic" surface states available on the TiO_2 surface, (b) the competing mechanism of solvation, and (c) the orbital interactions between the surface states and the adsorbates that remove the surface states from the bandgap.

BIBLIOGRAPHY

1. E. Becquerl; Compt. Rend 9, 561 (1839).

2. W.G. Adams and R.E. Day; Proc. Royal Soc.A 25, 113 (1877).

3. H. Gerisher in "Solar Power and Fuels", J.R. Boltan, Editor, Acadamic Press, New York (1977).

4. L.A. Harris and R.H. Wilson; Ann. Rev. Mater. Sci. 8, 99 (1978).

5. M.S. Wrighton, J.M. Bolts, A.B. Bocarsly, M.C. Palazzotto, andE.G. Walton; J. Vac. Sci. 15, 1429 (1978).

6. H.P.Marusaka and A.K. Ghosh; Sol. Energy 20, 443 (1978).

7. W.A. Gerrad and L.M. Rouse; J. Vac. Sci. Tech 15, 1155 (1978).

8. A.J. Nozik; Ann. Rev. Phys. Chem. 29, 189 (1978).

9. M. Tomkiwicz and H. Fay; Appl. Phys.18, 1 (1979).

10. M.A. Butler and D.S. Ginely; J. Mater. 15, 1 (1980).

11. A.J. Nozik, Phil. Trans. R. Soc. Lond.A 295, 453 (1980).

12. for up-to-date review see: "Proceedings of the Symposia on Photoelectrochemical Process and Measurements Techniques for Photoelectrochemical Solar Cells", Electrchemical Soc., N.Y. 1982, W.L. Walace, A.J. Nozik, S.K. Deb and R.H. Wilson eds.

13. A. Fujishima and K. Honda; Nature (London) 238, 37 (1972).

14. V.A. Mymalin and Y.V. Pleskov;"Electrochemistry of Semiconductors" (Plenum Press, New York, 1967).

15. C. Kittel; "Introduction to Solid State Physics", 5th Edition, John Wiley, New York 1976.

16. S.R. Morrision; "The Chemical Physics of Surfaces", Plenum Press, New York, 1977.

17. S.M. Sze; "Physics of Semiconductor Devices", Wiley-Interscience, 1969.

18. D.R. Frankl; "Electrical Properties of Semiconductor Surfaces", Pergmon Press, 1967.

19. H. Gerisher; Surface Sci.,18, 97 (1969).

20. R.H. Wilson; Solid State Mater. Sci. 10, 1 (1980).

21. J. Bardeen, Phys. Rev., 71 653 (1947).

22. H. Gerisher; "Physical Chemistry, An Adavance Treatise", Vol IXA, H. Eyring, Editor, Acadamic Press, New York, 1970.

23. E.C. Dutoit, F. Cardon, W.P. Gomes; Ber. Bunseng. Phys. Chem. 80, 447 (1976).

24. M. Tomkiewicz; J. Electrochem. Soc. 126, 1505 (1979).

25. P.J. Boddy; Surf. Sci. 13, 52 (1969).

26. (a) W. Schottky; Z. Phys. 113, 367 (1939); 118, 539 (1942). (b) N.F. Mott; Proc. Roy. Soc. A117, 27 (1939).

27. J.I. Pankove; "Optical Processes in Semiconductors",pp 36-38, prentice Hall, Englewood, N.J. (1971).

28. E.J. Johnson; "Semiconductors and Semimetals", Edited by R.K. Willardson and A.C. Beer, Vol.3, Acadamic Press, New York (1967).

29. W.W. Gartner; Phys. Rev. 116, 84 (1959).

30. M.A. Butler; J. Appl. Phys. 48, 1914 (1977).

31. R.H. Wilson; J. Appl. Phys. 48, 4292 (1977).

32. R.N. Hall, Phys. Rev. 87, 387 (1952).

33. W. Shockley and W.T. Read ; Phys. Rev. 87, 835 (1952).

34. A.L. Vanden Berge, F. Cardon and W.P. Gomes; Sur. Sci. 39, 368 (1973).

35. J. Reichaman; Appl. Phys. Lett. 36, 574 (1980).

36. H.S. Jarret; J. Appl. Phys. 52, 4681 (1981).

37. F.El. Guibaly, K. Colbow and D.L. Funt; J. Appl. Phys. 52, 3480 (1981).

38. M. Gleria and R. Memming; J. Electroanal. Chem. 65, 163 (1975).

39. J.G. Mavroides, J.A. Kafalas, D.F. Kollesar; Appl. Phys. Lett. 28, 241 (9176).

40. M.A. Butler, R.D. Nasbi, R.K. Quinn; Solid State Commun. 19, 1011 (1976).

41. L.A. Harris and R.H. Wilson, J. Electrochem. Soc. 123, 1010 (1976).

42. S.N. Frank and A.J. Bard; J. Am. Chem. Soc. 97, 7427 (1975).

43. J.-N. Chazalviel, Surf. Sci. 88, 204 (1979).

44. J.-N. Chazalviel, J. Electrochem. Soc. 127, 1822 (1980).
45. J.-N. Chazalviel, J. Electrochem. Soc. 129, 963 (1982).

46. W. Shockley and G.L. Pearson; Phys. Rev. 74, 232 (1948).

47. I. Tamm; Physik. Z. Sowjetunion 1, 733 (1933).

48. W. Shockley; Phys. Rev. 56, 317 (1939).

49. S.G. Davison and J.D. Levine; "Solid State Physics", Vol. 25, Editors H. Ehrenreich, F Seitz and D. Turnbull, Acadamic Press, New York (1970).

50. J.M. Kowalski, K.H. Johnson and H.L.Tuller; J. Electrochem. Soc. 127, 1969 (1980).

51. H.S. Tayler; J. Am. Chem. Soc. 53, 578 (1931).

52. M. Tomkiewicz; Surf. Sci. 101, 286 (1980).

53. K. Bohnenkamp and H. Engel; Z. Electrochem. 61, 1184 (1957).

54. M. Hoffman-Perez and H. Gerischer; Z. Electrochem. 65, 771 (1961).

55. P.J. Boddy and W.H. Brattain; J. Electrochem. Soc. 109, 812 (1962).

56. P.J. Boddy and W.H. Brattain; Proc. Intl. Conf. on Physics of Semiconductors, Edited by A.C. Strickland, Exter, England (Acadamic Press,1962).

57. R. Memming, Phys. Lett. 7, 89 (1963).

58. R. Memming, Surf. Sci. 2, 509 (1963).

59. P.J. Boddy and W.H. Brattain; J. Electrochem. Soc. 110, 570 (1963).

60. A. Many; J. Phys. Chem. Solids 26, 575, 587 (1965).

61. H. Morisaki, M. Haria and K. Yazawa; Appl. Phys. Lett. 30, 7 (1977).

62. R.H. Wilson; J. Electrochem. Soc. 127, 228 (1980).

63. A. Heller, K.C. Chang and B. Miller; J. Electrochem. Soc. 124, 697 (1977).

64. M.Tomkiewicz; J. Electrochem. Soc. 127, 1518 (1980).

65. D. Laser and S. Gottesfeld, J. Electrochem. Soc. 126, 475 (1979).

66. M.P. Dare-Edwards, A. Hamnett and J.B. Goodenough; J. Electroanal. Chem. Interfacial Electrochem. 119, 109 (1981).

67. R.P. Silberstein, F.H. Pollak, J.K. Lyden and M. Tomkiewicz;
Phys. Rev. B 24, 7397 (1981).

68. R.P. Silberstein, J.K. Lyden, M. Tomkiewicz and F.H. Pollak; J. Vac. Sci. Technol. 19, 406 (1981).

69. C.Gutierrez and P. Salvador; J. Electroanal. Chem. 138, 457 (1982).

70. M. Tomkiewicz; J. Electrochem. Soc. 126, 2220 (1979).

71. M. Tomkiewicz in " Semiconductor Liquid-Junction Solar Cells", Proceedings of the Electrochemical Society, 77-3 92 (1977).

72. M. Tomkiewicz, J.K. Lyden, R.P. Silberstien and F.H. Pollak in "Photoeffects at Semiconductor-Electrolyte Interface", edited by A.J. Nozik, ACS Symposium Series No. 146, Washington D.C. (1981), p.267.

73. J.K. Lyden, M.H. Cohen and M. Tomkiewicz; Phys. Rev. Lett. 47, 961 (1981).

74. P.J. Boddy; J. Electroanal. Chem. 10, 199 (1965).

75. R. DeGryse, W.P. Gomes, F. Cardon and J. Vennik; J. Electrochem. Soc. 122, 711 (1975).

76. M. Cardona in "Modulation Spectroscopy", Editiors, F.Seitz. D. Turnbull, and H. Ehrenreich, Acadamic Press, New York (1969).

77. M. Cardona, K.L. Shaklee, and F.H. Pollak; Phys. Rev. 154, 696 (1967).

78. D.E. Aspnes; Sur. Sci. 37, 418 (1973).

79. D.E. Aspnes in "Handbook in Semiconductors", Vol.2, North Holland (1980).

80. D.E. Aspnes; Phys. Rev. Lett. 28, 913 (1972).

81. F.H. Pollak in ref 12

82. S.F. Pond; Sur. Sci. 37, 596 (1973).

83. J.D.E. Mc Intyre; "Adavances in Electrochemistry and Electrochemical Engineering", Vol.9, ed. R.H. Muller, Wiley Interscience,New York (1973).

84. S.S. Lu, F.H. Pollak, and P.M. Raccach: Proc. Workshop held at NBS, Guithersurbg, 1975, NBS Special Publication 455, page 125.

85. D.M. Kobb, W. Boeck, K.M. Ho, and S.H. Liu; Phys. Rev. Lett. 47, 1921 (1981).

86. R. Tenne, Y. Mirovsky, Y. Hreenstein, and D. Cahen; J. Electrochem. Soc. 129, 1506 (1982).

87. L.A. Harris and R.H. Wilson; J. Electrochem. Soc. 123, 7 (1976).

88. K. Vos and H.J. Krusemyer; J. Phys. C, Solid State Phys. 10, 3893 (1977).

89. A.K. Gosh, F.G. Wankin, and R.R. Addis; Phys. Rev. 184, 979 (1969).

90. J.D. Zook; Phys. Rev. Lett. 20, 848 (1968).

91. J.O'M Bockris and A.K.N. Reddy; "Modern Electrochemistry", Vol. 2, Plenum Press, N.Y. (1970).

92. D.E. Yates and T.W. Healy; J. Chem. Soc. Faraday Trans. 1,76, 9 (1980).

93. V.E. Henrich and R.L. Kurtz, Phy. Rev. B. 23, 6280 (1981).

94. R.V. Kasowaski and R.H. Tait; Phys. Rev. B 20, 5168 (1979).

95. T. Wolfram and S. Elliatioglue; Appl. Phys. 13, 21 (1977).

96. for example seee: W.A. Harrison, "Electronic Structure and the Propreties of Solids" Chap. 10, W.H. Freeman and Comp., San Fransisco (1980).

97. R.H. Tait and R.V. Kasowski; Phys. Rev. B, 20, 5178 (1979).

98. Y.W. Chang, W.J. Lo and G.A. Somorjai; Surf. Sci. 64, 588 (1977).

99. V.E. Henrich; Prog. Surf. Sci. 9, 143 (1979).

100. R.L. Kurtz and V.E. Henrich; Phys. Rev. B 26, 6682 (1982).

101. M.L. Knotek, Surf. Sci. 91, 117 (1980).

102. M.L. Knotek, Surf. Sci. 101, 334 (1980).

103. M. Lavagna, J.P. Pique, and Y. Marfaig; Solid State Electronic 20, 235 (1977).

104. B.O. Seraphin and N. Bottka; Phys. Rev. 139, 560 (1965).

105. R. Trykozko in "Proceedings of the Third International Conference of Ternary Compounds" Edinburgh, April 1977,page 249.